Experimental Investigation of the Role of Turbulence Fluctuations on Incipient Motion of Sediment

Ahmet Ozan Celik

Dissertation submitted to the faculty of the Virginia Polytechnic Institute and State University in partial fulfillment of the requirements for the degree of

Doctor of Philosophy
In
Civil Engineering

Panayiotis Diplas, Chair
Clint L. Dancey, Co-Chair
Joseph A. Schetz
Pavlos P. Vlachos
Linbing Wang

May 4, 2011
Blacksburg, VA

Keywords: Incipient Motion, Hydrodynamic Forces, Impulse, Turbulence, Open channel flow, Rough bed, Particle Tracking System, Pressure Measurements

Copyright © 2011, Ahmet Ozan Celik

Experimental Investigation of the Role of Turbulence Fluctuations on Incipient Motion of Sediment

Ahmet Ozan Celik

ABSTRACT

The movement of granular material along a streambed has been a challenging subject for researchers for more than a century. Predicting the limiting case of nearly zero bedload transport, usually referred to as threshold of motion or critical condition, is even more challenging due to the highly fluctuating nature of turbulent flow. Numerous works have advocated that the peak turbulent forces, randomly occurring in time and space with magnitudes higher than the average, initiate the bed material motion. More recent findings have shown that not only the magnitude of the peak turbulent forces acting on individual grains but their duration as well have to be considered for determining the incipient conditions. Their product, or impulse, is better suited for specifying such conditions.

The goal of this study was to investigate the mechanism responsible for initiation of sediment motion under turbulent flow conditions. The impulse concept was investigated by utilizing appropriate measurement methods in the laboratory for determining the condition of incipient motion. The experimental program included measurements of particle entrainment rates of a mobile grain and turbulence induced forces acting upon a fixed grain for a range of flow conditions. In addition, near bed flow velocities were measured synchronously with both the entrainment and pressure measurements at turbulent resolving frequencies.

Results of this work covered the limitations and uncertainties associated with the experimental methods employed, and the description of the inadequacies of existing incipient motion models via the impulse framework. The extreme sensitivity of bed material activity to minute adjustments in flow conditions was explained by the associated change in the frequency of impulse events. The probability density function proposed for impulse was used together with the critical impulse to estimate the particle entrainment rate for a range of flow conditions. It was shown that the impulse events with potential to dislodge the grain were occurring mostly during sweep type of flow structures. The impulse events were also typically accompanied by positive lift forces. The force patterns showed that the positive peaks in the lift consistently occurred before and after the impulse events in the drag force. The magnitude of these lift forces were significantly higher in the wake of a cylinder compared to that of uniform flow conditions. The time average lift force in the wake of a cylinder was also observed to be positive with magnitudes reaching more than 30% of the submerged weight of the particle. The cylinder caused the downstream turbulence intensity to increase slightly but the particle entrainment rate to increase significantly. This finding provided a physically based explanation for the modification of turbulent force fluctuations and resulting changes in the particle movement rates by such unsteady flow conditions.

Dedicated to my parents Faize, Ali, Phyllis and Cliff

Acknowledgements

I would like to sincerely thank my advisors Dr. Diplas and Dr. Dancey for everything they have done for me during my PhD study at VT. Working for Drs. Diplas and Dancey has been an incredible experience for me. I am proud to be one of their graduate students and a member of the impulse team.

I also would like to thank my committee members; Dr. Schetz, Dr. Vlachos and Dr. Wang for valuable discussions that have helped shape this work.

My colleagues, Nikolaos Apsilidis, Polydefkis Bouratsis, Brandon Dillon, Miles Ellenberg, Krista Greer, Soonkie Nam, John Petrie, Matthew Rice, Collin Steward and Manousos Valyrakis deserve special thanks. It has been a pleasure working with you all at BEHL-VT.

I owe the Departments of Civil and Environmental Engineering and Mechanical Engineering at Virginia Tech a lot for financially supporting me in my last two years at VT. I would also like to thank Anadolu University in Eskisehir, Turkey for the financial support they provided during the early years in my PhD study.

Attribution

This dissertation consists of four self-contained chapters (chapters 2-5). Chapters 2 and 3 have been published in peer-reviewed journals. This attribution page is for introducing the co-authors and clarifying their contribution to these chapters.

Chapter 2: Professor Panayiotis Diplas of the civil and environmental engineering department at Virginia Tech, Associate Professor Clinton L. Dancey of the mechanical engineering department at Virginia Tech and Mr. Manousos Valyrakis, a former graduate student at the Baker Environmental Hydraulics Laboratory at Virginia Tech are co-authors of this research article. This article was prepared by Professor Panayiotis Diplas and Ahmet Ozan Celik. Associate Professor Clinton L. Dancey and Manousos Valyrakis reviewed and revised the article. Professor Panayiotis Diplas, Associate Professor Clinton L. Dancey also guided the particle tracking experiment performed by Ahmet Ozan Celik which is presented in the paper.

Chapter 3: Professor Panayiotis Diplas of the civil and environmental engineering department at Virginia Tech, Associate Professor Clinton L. Dancey of the mechanical engineering department at Virginia Tech and Mr. Manousos Valyrakis, a former graduate student at the Baker Environmental Hydraulics Laboratory at Virginia Tech are co-authors of this research article. This article was prepared by Ahmet Ozan Celik. Professor Panayiotis Diplas, Associate Professor Clinton L. Dancey and Manousos Valyrakis reviewed and revised the article. Professor Panayiotis Diplas, Associate Professor Clinton L. Dancey guided the experimental work which was performed by Ahmet Ozan Celik.

Table of contents

Chapter 1. Introduction……..… 1
1. Overview……..…….... 1
2. Organization…….…….…….... 2

Chapter 2. Non-intrusive Method for Detecting Particle Movement Characteristics near Threshold Flow Conditions…… 5
Abstract……..…..... 5
1. Introduction……..…… 6
2. Threshold of Movement Determination…….……... 9
3. Discussion and Conclusions…….…….....19
Acknowledgements…….…….…… 20
References…...…….. 21

Chapter 3. Impulse and Particle Dislodgement under Turbulent Flow Conditions…….23
Abstract……...….. 23
1. Introduction……..…. 24
2. Impulse Concept……...27
A. Impulse Detection……...……...…….. 28
3. Experiments……...……..32
A. Incipient Particle Motion Detection……...…….. 33
B. Experimental Procedure……...…….....35
4. Results and Analysis…….....36
A. Distribution of Impulse……...…….....39
B. Critical u^2 and Number of Impulses……..44
C. Critical Impulse and Number of Grain Entrainments…...…….. 49
D. Probability of Particle Entrainment……...……..53
5. Implications of the Impulse Concept for Low Mobility Conditions…..…..….. 56
6. Conclusions…….....…….. 59
Acknowledgements…….……...…….....…….... 61
Appendix: Derivation of the Pdf for Impulse…….... 61
References……..…….... 64

Chapter 4. Instantaneous Pressure Measurements on a Spherical Grain under Threshold Conditions ……..…….....…….... 67
Abstract…….....67
1. Introduction……..…… 68
2. Experiments……...72
2.1 Devices and Methods for Experiments……...……...……..76
2.2 Static Calibration Test……...……...……..…..78
2.3 Dynamic Performance Test……...……...…….....81
2.4 Measurement Uncertainty in the Flume Tests…….…….....84
*2.5 Summary of Experiment*s……...…….……...…….....84
Experiments under Uniform Flow conditions……...…..... 85

Experiments in the Wake of a Cylinder……..... 86
3. Characteristics of the Surface Pressures Acting on the Grain……... 88
3.1 Uniform Flow Conditions..... 88
3.2 Cylinder Tests.....90
4. Correlations between the Individual Pressures..... 91
4.1 Uniform Flow Conditions.....91
4.2 Cylinder Tests.....94
5. Pressures and Near-bed Flow Velocity……... 97
5.1 Uniform Flow Conditions.....98
5.2 Cylinder Tests…… 101
6. Conditionally Sampled Pressure Fluctuations…… 103
6.1 Uniform Flow Conditions…… 107
6.2 Cylinder Tests…… 110
7. Conditionally Sampled Force Fluctuations…… 112
7.1 Uniform Flow Conditions…….. 112
7.2 Cylinder Tests.....115
8. Instantaneous Forces…… 118
8.1 Force Magnitudes..... 118
8.2 Force Event Durations……..122
9. Discussion on the Time Delay between Flow velocity and Pressures…..130
10. Summary and Discussions..... 133
Acknowledgements……136
References……137

Chapter 5. Instantaneous Turbulent Forces and Impulse on a Rough Bed: Implications for Initiation of Bed Material Movement ……141
Abstract…… 141
1. Introduction…… 141
2. Experiments…… 144
3. Impulse Detection…… 147
4. Results…… 151
4.1 Distribution of Directly Detected Impulse……..151
4.2 Forces during Impulse Events…….. 155
Ensemble Average of the Forces of Impulse Events…….. 155
Drag Coefficients of Impulse Events…….. 157
1D and 2D Histograms of the Forces of Impulse Events…….....162
Influence of Near-bed Bursting Phenomenon on the Forces of Impulse Events…….. 164
4.3 Implications for Particle Entrainment……..... 167
The Number of Detected Impulse Events…….....167
The Effect of Lift Force during Impulse Events on the Critical Impulse…….....169
The Effect of Turbulence Intensity on the Number of Impulse Events and Particle Entrainment…….....171
5. Conclusions…… 174
Acknowledgements.....175

References…….....…..…176

Chapter 6. Conclusions…….....…..… 178

List of Figures

Chapter 2. Non-intrusive Method for Detecting Particle Movement Characteristics near Threshold Flow Conditions……....5

Figure 1. Plot of dimensionless shear stresses (τ_{0*}) against normalized bedload transport rates (q_{s*})……...……. 8

Figure 2. Solitary test particle and pocket geometry. Sketch on the upper left side shows top view and sketch on the right shows side view……. 10

Figure 3. The sketch of the flume, showing the working section and associated instrumentation for the entrainment experiments ……...…. 11

Figure 4. Teflon® test particle, retaining pin, 2D LDV beams, and identical size well packed glass spheres forming the flume bed ……...…. 12

Figure 5. A typical photo-detector output displaying rocking and pivoting sample events of the mobile test particle. Upper right side: Enlarged voltage signal corresponding to 1 mm displacement of the ball in the streamwise direction (dashed ellipse in the main figure)……...……. 13

Figure 6. Representative time series of stream-wise velocity (measured at one diameter upstream of the particle, at a sampling rate ~300 Hz). The time instant of the initiation of the test particle motion (matching the pivoting event shown in Fig. 5) is displayed with a dashed vertical line……. 14

Figure 7. Ensemble average of u vs. relative time and time delay results (t = 0 is the uncorrected instant of entrainment). Time delay is due to the distance between the LDV measurement volume and the grain (See Fig.2). A span of ±500 data points for each entrainment instant were used to obtain the ensemble average of u. The horizontal solid line indicates the time-average value of u over 30 minutes……...……...……. 16

Figure 8. a) Treatment of raw calibration data (Volt vs. displacement). b) Entrainment signal calibration procedure (normalized voltage intensity vs. displacement); c1 and c2 data points from still water and c3 from running water tests……...……. 18

Figure 9. Results from the calibration of the entrainment signal. Displacement of the center of the particle in the streamwise direction ….……. 19

Chapter 3. Impulse and Particle Dislodgement under Turbulent Flow conditions.. 21

Figure 1. Definition sketch of the forces acting on a spherical particle resting on identical size densely packed spheres, side view (left) and top view (right) of the bed geometry ……..……. 29

Figure 2. Representation of the impulse events in the u^2 time series. i^{th} event is characterized by $<u^2>_i$ and T_i values, representing force magnitude and duration, the product of which is impulse = $<u^2>_i T_i$ (corresponds to the shaded rectangular area below the u^2 line). t_0 and t_n were determined by interpolating the adjacent data points in the u^2 time series. The vertical line between the t_0 and t_n indicates that the particle movement was observed during the i^{th} event……. 31

Figure 3. Side view (right) and top view (upper left corner) sketches of the mobile test particle and pocket geometry (diameter of the grains, d = 12.7 mm) ...……..…….33

Figure 4. From top to bottom: Representative time series of, u^2, impulse ($<u^2>_i T_i$), and photo-detector output, from run E1. Dashed vertical lines in the top two plots indicate detected particle movements. Secondary vertical axes in the top two plots: binary 0/1 signal. Explanation of the solid vertical lines in the bottom plot: A: beginning of a rocking event, B: beginning of a pivoting event, C: instant when the test particle reached the retaining pin, D: instant when the test particle started rolling back to its original pocket, E: instant when the particle reached its original pocket……..……34

Figure 5. Histograms of u^2, $<u^2>_i$, T_i and I_i from left to right for the run E1. Nearly 280,000 data points (counts) for u^2 and total of 1978 data points for $<u^2>_i$, T_i and I_i are represented in each histogram ……. 39

Figure 6. Relationship between impulse intensity, δ, and particle Reynolds number, Re^*.. ……..……. 41

Figure 7. Plots of the function given by Eq. 5 for a range of δ values ...……41

Figure 8. Comparison of Eq. 5 with measured pdfs for E1-E8. Solid lines are used to show pdfs obtained from Eq. 5……..……... 43

Figure 9. Semilogarithmic plot of measured pdfs from all eight runs. Eq. 5 is also presented with δ=0.7 and 1.1 for comparison……..……44

Figure 10. $<u^2>_i$ vs. T_i plots. 1978 data points from run E1 (left), 1101 data points from run E4 (right). Black circles indicate $<u^2>_i$, T_i combinations that are associated with full particle dislodgement (pivoting)..……. 46

Figure 11. a) Illustration of the approach used for varying the critical u^2. b) Number of detected impulses vs. the ratio of critical u^2 level used to the original u^2_{cr} ……..…….. 47

Figure 12. $I_i \sim <u^2>_i T_i$ vs. $<u^2>_i$ plot. The region where movement and no movement areas overlap is shown with a gray band between the impulse values of 0.0034 m^2/s and 0.0095 m^2/s. Horizontal arrow indicates the critical impulse level ……..…….50

Figure 13. The plot of number of impulse events above critical impulse per min vs. total number of impulse events above critical u^2 per min. Data points with black circles are from all eight runs where a constant I_{cr} was used. White and gray circles indicate results from run E1 and E5 respectively, where various I_{cr} values were used. Data with the plus sign indicates the actual particle movements (n_E) vs. n_T observed in each run……..……..……. 53

Figure 14. Illustration of the probability analysis. The probability that a flow event will generate a level of impulse that exceeds a specified critical level, I_{cr}, is indicated by the shaded area and is assumed to be equal to the probability of particle entrainment, $p_{E...}$……..……54

Figure 15. Probability of particle entrainment vs. probability of exceedance of critical impulse...……..……. 55

Figure 16. Dimensionless bed load parameter vs. Shields Stress (left *y*-axis) from Refs 10 and 12. Note that data only in the τ^* range between 0.005 and 0.016 were used. The number of impulse events above critical impulse per min ((right *y*-axis) vs. Shields Stress is also plotted……..……. 58

Chapter 4. Instantaneous Pressure Measurements on a Spherical Grain under Threshold Conditions …….....…….…….. 67

Figure 1. A sketch of the different flume sections (top view)……. 73

Figure 2. Instrumented fixture. (*a*) Drawings of the fixture during design process. (*b*) Photo of the fixture during assemblage. Dashed circle indicates the pressure tap on the top of the grain before it was trimmed. (*c*) Photo of the fixture installed in the flume bed looking upstream. (*d*) Definition sketch for the pressure measurement points and bed geometry. Dashed lines indicate the brass tubing lines. The Cartesian coordinate system used in this study is shown in (*a*) and (*d*)..……..……. 75

Figure 3. Photo of the test rig used for the static calibration and dynamic performance tests……..…….79

Figure 4. Voltage output of the transducer with respect to the static load in terms of water column (h) above the transducers' sensing element, data shown with cross symbols for transducer #2. Insets: Equation on top represents the best fit line; figure on the lower right corner is a magnification of the data point with maximum residual error (empty circle in this figure represents the predicted value by the best fit line equation); vertical line on lower left corner shows the DC offset voltage level for this transducer..... 80

Figure 5. Magnitude and phase plots of transfer function between the pressure signals p_3 (top) and p_4 (bottom).. 83

Figure 6. Side view of the test section with the test particle in the wake of a cylinder..... 87

Figure 7. Pressure histograms from run A2; 225,000 data points are represented in each histogram... 89

Figure 8. p'_{rms}/τ_0 vs. Re^* plots from uniform flow conditions (A1-A9)..... 91

Figure 9. Cross correlation functions between: (*a*) p_1 and p_2, (*b*) p_1 and p_3, (*c*) p_2 and p_3 (*d*) p_1 and p_4 (*e*), p_2 and p_4, and (*f*) p_3 and p_4, all from run A2..... 92

Figure 10. A (3D) surface plot of the instantaneous p_1, p_2 and p_3 from run A2. Color bar represents the magnitude of p_3. 225000x3 data points (p_1, p_2 and p_3) were used to create this plot... 93

Figure 11. Cross correlation functions between: a) p_1 and p_2, b) p_1 and p_3, c) p_2 and p_3 d) p_1 and p_4 e) p_2 and p_4, f) p_3 and p_4, all from run with the cylinder D = 33.4 mm..... 96

Figure 12. Power spectral density vs frequency of p_1 signal from cylinder tests (D = 33.4 mm)..... 96

Figure 13. Representative time series of, u, w (top) and simultaneously measured surface pressures (bottom) from run A2..... 97

Figure 14. Representative time series of, u, w (top) and simultaneously measured surface pressures (bottom) from a cylinder test (D = 33.4 mm)..... 98

Figure 15. CCFs between u and the pressures from run A2..... 100

Figure 16. CCFs between w and the pressures from run A2..... 101

Figure 17. CCFs between u and the pressures from the cylinder test with D = 33.4 mm..... 102

Figure 18. CCFs between w and the pressures from the cylinder test with D = 33.4 mm...……..……..……103

Figure 19. Representative time series of (filtered) p_1 from run A2. The detected local peaks with $p' > p'_{rms}$ and $p' > 2p'_{rms}$ are shown with empty and solid circles respectively. The threshold levels (for H = 1 and 2) are shown with horizontal, dashed lines. Time average p_1 is specified with horizontal, solid line...…….104

Figure 20. Pdf of the detected peak magnitudes in p_1 (H = 2). (a) data from UC. (b) data from cylinder test with D = 33.4 mm. Both normalized histograms and theoretical pdfs are presented. pdf: Johnson SB distribution, p-value: 0.52 for (a) and 0.65 for (b)...……..……...106

Figure 21. Ensemble averaged waveforms of conditionally sampled pressures (p_{1-4}) and velocities (u and w) from top to bottom (a)-(f), based on the detected positive peaks in p_1 signal. t = 0 is the instant when the peaks in p_1 were detected. Data from run UC was used and the ensemble average values are based on the 1296 detected peaks. Time average w is shown with dashed, horizontal line in (f). Threshold level, H = 2...……..……108

Figure 22. Ensemble average waveforms of conditionally sampled pressures (p_{1-4}) and velocities (u and w) from top to bottom (a)-(f), based on the detected positive peaks in p_1 signal. t = 0 is the instant when the peaks in p_1 were detected. Data from cylinder test D1 was used and the ensemble average values are based on detected 923 positive peaks. Threshold level, H = 2...……...…111

Figure 23. The waveforms for the horizontal and vertical differences of ensemble average of the conditionally sampled pressures (top (a) and bottom (b) figures respectively). t = 0 is the instant when the peaks in p_1 were detected. Data from runs A1, A9 and UC were used. Threshold level, H = 2...……..…113

Figure 24. The waveforms ensemble average of the conditionally sampled horizontal and vertical pressure gradients (top (a) and bottom (b) figures respectively). t = 0 is the instant when the peaks in p_1 were detected. Data from cylinder tests with D = 33.4 mm were used. Threshold level, H = 2...……116

Figure 25. Ensemble average waveforms of conditionally sampled lift force and velocities (u and w) from top to bottom, based on the detected positive peaks in p_1 signal. t = 0 is the instant when the peaks in p_1 were detected. Data from cylinder test D1 was used and the ensemble average values are based on the 923 detected positive peaks. Threshold level, H = 2...……..……117

Figure 26. CCF between drag and lift forces from run A2...……..……119

Figure 27. CCFs between u and drag force (bold line and) w and drag force (dashed line) from run A2...……...……..……120

Figure 28. CCFs between u and lift force (bold line and) w and lift force (dashed line) from run A2...……..……...……...…120

Figure 29. The histograms of the instantaneous lift force normalized with the critical pressure from runs UC and D1...……...……...121

Figure 30. Representative time series of (filtered) p_1 from run A2. The detected local peaks with $p' > 2p'_{rms}$ are shown with solid circles. Time average p_1 is specified with horizontal, solid line. The widths of the shaded rectangular areas indicate the detected event durations, T, while the heights indicate the average p_1 over duration T ($<p_1>$). The vertical dashed lines show the time of occurrence of events for the duration analysis...……..……..…….123

Figure 31. Histogram of the 478 events peak durations detected in p_1 ($H = 2$). Data from UC was used...……..……..……124

Figure 32. The surface plots of the peak event durations (*a*), magnitudes of p_1 signal (*b*), magnitudes of p_2 signal (*c*), magnitudes of p_3 signal (*d*) on $<u>$-$<w>$ plane. Data from run UC was used and 478 events with finite durations are represented. Color bars represent the duration (*a*) and magnitude (*b*), (*c*), (*d*) of pressure peaks. Note that the same colormap was used for different scales in the subplots. Horizontal and vertical dashed lines indicate the time average u and w values over the entire test duration respectively. Data from run UC...……125

Figure 33. The surface plots of the magnitudes of p_4 signal on $<u>$-$<w>$ plane (*a*), two dimensional histogram of the $<u>$ and $<w>$ (*b*). The color bar in (*b*) represents the number of counts for the 2D histogram. Horizontal and vertical dashed lines indicate the time average u and w values over the entire test duration respectively. Data from run UC...……..……..……127

Figure 34. The surface plots of the durations of drag force signal on drag-lift plane (*a*), two dimensional histogram of the drag and lift (*b*). The color bars in (*a*) shows the event durations and in (*b*) represents the number of counts for the 2D histogram. Data from run UC...……..……..……...……129

Figure 35. The surface plots of the durations of drag force signal on drag-lift plane (*a*), two dimensional histogram of the drag and lift (*b*). The color bars in (*a*) shows the event durations and in (*b*) represents the number of counts for the 2D histogram. Data from run D1. ...……..……..……130

Figure 36. Time traces of the synchronized streamwise flow velocity, u (*a*) the pressures acting on the front the particle, p_1 (*b*) and the pressures acting on the back of the particle, p_2 (*c*). Data from run A2 is presented. Vertical lines show flow structures which have reverse effects on p_1 and p_2...……...……131

Chapter 5. Instantaneous Turbulent Forces and Impulse on a Rough Bed: Implications for Initiation of Bed Material Movement ……..……...141

Figure 1. Bed configuration of mobile and instrumented particle experiments. a) Definition sketch for the pressure measurement points and bed geometry. b) Side view of the test section with the test particle in the wake of a cylinder...……...145

Figure 2. Definition sketch of the forces acting on a spherical particle resting on identical size densely packed spheres, side view (left) and top view (right) of the bed geometry. This is the arrangement that was used for both the pressure and the particle entrainment measurements...……...……148

Figure 3. Synchronized plot of measured forces acting on the test grain and flow velocities measured one diameter upstream of the grain. From top to bottom: Representative time series of F_D, F_L, u, and w from run U3. Shaded vertical regions indicate events within F_D, F_L, u, and w time series during which $F_D \geq F_{D_{cr}}$. The i^{th} event was selected to show the magnitude of $< F_D >_i$, $< F_L >_i$, $<u>_i$, and $<w>_i$...……..……...……150

Figure 4. Histograms of the event duration (*a*) and impulse (*b*). Data from Run U2 presented...…….151

Figure 5. Comparison of Eq. 3 with measured pdfs for run U2. Solid lines are used to show pdfs obtained from Eq. 3 and circles from data. $\delta = 1.01$ from the direct measurements (open circles) and $\delta = 0.96$ from force estimations using C_D=0.9 in Eq. 3 with the effect of time-averaged lift included in Eq. 1 (solid diamonds). *p*-value = 0.53....……..……...……153

Figure 6. Comparison of Eq. 3 with measured pdfs for run U3. Solid line is used to show pdf obtained from Eq. 3and open circles from data. $\delta = 0.95$. *p*-value = 0.65...……..……...……154

Figure 7. Comparison of Eq. 3 with measured pdfs for run CD1 (cylinder). Solid line is used to show pdf obtained from Eq. 3 and open circles from data. $\delta = 1.02$. *p*-value = 0.56...……..……..……155

Figure 8. Variations in the non-dimensionalized $<F_D>_{mean}$ and $<F_L>_{mean}$ (right axis) with Re^*. Linear and polynomial curves were included for visual guidance only...……..……...……157

Figure 9. Plot of the average drag coefficients vs. Re^*....……...159

Figure 10. Histogram of the $<C_D>$, 2522 data points from Run U2 were used...……..……...……159

Figure 11. Scatted plot of $\langle C_D \rangle_i$. vs non-dimensionalized $\langle u \rangle_i$. Shaded gray region represents ±50 error around the best fit curve...……...160

Figure 12. 3D surface plot of $\langle u \rangle_i$, $\langle C_D \rangle_i$ and I_i (data: run U3). Color bar indicates the impulse magnitude....…….……161

Figure 13. 3D scatter plot of $\langle u \rangle_i$, $\langle C_D \rangle_i$ and $\langle F_L \rangle_i$ (data: run U3). Blue ($\langle F_L \rangle_{mean}$) red and green lines ($\langle F_L \rangle_{mean} \pm 2\langle F_L \rangle_{std}$) are obtained using the equation given in Fig.11 inset…….....…….162

Figure 14. Histograms of the event average drag force (left) and lift force (right). Data from Run U2 presented....…….……..163

Figure 15. 3D mesh plot of the joint histogram of (a) drag force versus lift force and (b) impulse versus lift force (data from run U2-2522 data points were used, number of bins: 30x30 on $\langle D \rangle$ -$\langle L \rangle$ plane and 50x50 on I - $\langle L \rangle$ plane).. ….164

Figure 16. 3D surface plots of (*a*) impulse on $\langle u \rangle'$ - $\langle w \rangle'$ plane. Color bar on top indicates the impulse magnitude. (*b*) lift force associated with impulse events on $\langle u \rangle'$ - $\langle w \rangle'$ plane. Color bar indicates the lift force magnitude/direction. Run U3....…….……165

Figure 17. Bar plots of % total number of impulse events for each quadrant for all nine runs....……...……166

Figure 18. Plot of the total number of impulse events per min obtained using different methods, vs. Re^*. Line describes the overall variation of n calculated from directly measured F_D data with Re^* ($R^2 = 0.94$)....…….……168

Figure 19. Surface plot of the 2D histogram of impulse versus lift force (from run U2-2522 impulse events were used, number of bins: 50x50 on I-$\langle F_L \rangle$ plane). Color bar indicates the counts. This figure is the same as Fig 15b....……..171

Figure 20. Ratios of particle entrainment frequency data obtained in cylinder tests to that of undisturbed flow conditions vs. turbulence intensity. Marker labels indicate the runs...…….……...173

Figure 21. Ratios of bed material movement (bed load, q, data from Sumer et al. 2003, particle entrainment frequency, n_e, data from present tests, also shown in Fig. 20) obtained in cylinder test to that of undisturbed flow conditions vs. turbulence intensity....……..……173

List of Tables

Chapter 1. Introduction…….. 1

Table 1. Data types, flow types and concepts presented in each chapter..…..…... 4

Chapter 3. Impulse and Particle Dislodgement under Turbulent Flow Conditions. 21

Table 1. Summary of the test conditions for entrainment experiments..…...….. 37

Table 2. Summary of the impulse parameters obtained from 15 minute runs..….....…….. 38

Table 3. Number of impulse events and particle movements observed for 15 min. Note that $n_E = n_P + n_R$..…….…...…..45

Table 4. Summary of the results from conditions where various u^2 critical values were used for Run E1..….....…….. 47

Chapter 4. Instantaneous Pressure Measurements on a Spherical Grain under Threshold Conditions ……..…….. 67

Table 1. Summary of the flow conditions. Note that the last row presents the undisturbed flow condition parameters for cylinder tests (UC) without the cylinder.……..….. 86

Table 2. Summary of the results from peak detection analysis (for p_1). The last four rows present the tests with the cylinders.……...….105

Chapter 5. Instantaneous Turbulent Forces and Impulse on a Rough Bed: Implications for Initiation of Bed Material Movement …….141

Table 1. Summary of the flow conditions..……...….147

Chapter 1. Introduction

1. Overview

The incipient motion condition for granular material defines the stability of erodible beds and constitutes the central problem for sediment transport in rivers, coastal areas and atmospheric flows. Energetic flow events near the bed mobilize the sediment grains at incipient conditions. These events occur randomly in space and time due to the turbulent flow near the bed. Magnitude of forces acting on individual grains has been used extensively to characterize these flow events and to identify the threshold conditions. Despite these efforts and partially due to the experimental difficulties in observing the threshold of sediment movement with synchronized flow measurements, the precise determination of the incipient condition remains elusive. On the other hand, more recent findings have provided evidence that not only the magnitude of the peak turbulent forces acting on individual grains but their durations as well have to be considered for determining the incipient conditions for a given bed material size and configuration.

The purpose of this work was to investigate the mechanism of particle entrainment due to turbulent flow. This was pursued by analyzing the surface pressures and entrainment of a spherical grain, and the near bed flow velocity under a range of uniform and cylinder wake flows. The analysis presented here is based on the treatment of turbulence fluctuations in the drag force as impulses, which are products of magnitude and duration of applied force. The impulse concept effectively links the characteristics of turbulent flow to particle entrainment and has far reaching consequences in describing the inadequacies of existing incipient motion models as well as improving our ability to model a wide range of river mechanics and other geomorphology related phenomena.

2. Organization

This dissertation consists of four self-contained chapters (chapters 2-5). Each one of these chapters is an original article that has been or will be submitted to journals in the fields of fluid mechanics or sediment research.

This work utilized three major types of data collected from flume experiments to investigate the mechanism of particle entrainment. These data types are: flow velocity measured near the bed, particle entrainment rate and surface pressures acting on the particle. Because it was not possible to simultaneously measure all three, flow velocity-particle entrainment and flow velocity-pressure measurements were performed separately under identical flow conditions. The analysis included the investigation of magnitude and duration of pressures/forces acting on the grain and also the impulse concept applied to a fully exposed particle. The aforementioned experiments and analysis were performed for a range of uniform flows and cylinder wake flows. Table 1 summarizes the types of data, flow and analyses presented in each chapter.

In chapter 2, the nature of near threshold flow conditions and the difficulty in defining the incipient conditions due to the highly fluctuating nature of turbulent flow are discussed. The non-intrusive method for the particle entrainment experiments is presented in detail. This includes the uncertainty and limitations associated with the instrumentation. Final remarks demonstrate the complexities associated with implementing such controlled experiments in field conditions.

Chapter 3 introduces analysis of impulse events obtained indirectly from the near bed velocity. The statistics of these events is presented in detail. The sensitivity of impulse analysis to the critical force and impulse levels is demonstrated. A link is provided between the impulse distribution and the probability of particle entrainment.

That is, the significant increase observed in the particle entrainment rate with minute changes in the flow parameters at low shear stress conditions is explained well by the accompanying change in the occurrence of extreme impulse events above a critical level. This finding also helps elucidate the underlying mechanism for the well known but poorly understood phenomenon observed by others.

In chapter 4, the pressure measurements are presented in detail. The instrumentation, methods and the uncertainty in the measurements is explained. The relationships between individual pressures, forces approximated from the pressures and their relation to local flow velocity patterns are examined and important phase delays are revealed. The characteristics of the magnitude and duration of peaks in pressures, drag forces and lift forces are presented. Certain flow, pressure and force patterns which are important for particle entrainment are identified using conditional sampling method. The observed patterns show similarities with the commonly observed flow structures by others. It is shown that the dominance of sweep events in particle dislodgement is due to the frequent occurrence of long duration high magnitude events in this type of flow. It is also shown that in wake flows the average lift force is modified by the presence of the cylinder in a way that reduces the effective weight of the particle considerably. Instantaneous lift force is also shown to be reaching very high levels that can be consequential to particle mobility. A final remark in this chapter offers a rationale for inconsistencies in estimating the drag force using the near bed velocity.

Chapter 5 makes use of pressure, entrainment and velocity data to further investigate the impulse concept. Also, both the uniform flow and cylinder wake flow data is used. A comparison is presented on the effect of force approximations on the particle

movement analysis. It is shown that using a constant drag coefficient influences the detection of impulse events to a considerable extent. Lift forces occurring during impulse events are shown to change the critical impulse level required to dislodge the grain instantaneously. Finally, the actual role of increased turbulence intensity on the particle movement is advocated to be the increased average lift force under such conditions (chapter 4). This adjustment results in increased particle movement rates (chapter 3). This finding is substantiated by showing the qualitative similarities between the actual particle entrainment rates obtained in this study and well known observations of others available in the literature.

Chapter 6 summarizes the major findings of this work and discusses the future and potential direction of impulse concept.

Table 1. Data types, flow types and concepts presented in each chapter.

	Chapter #			
	2	3	4	5
Flow velocity near the bed	✓	✓	✓	✓
Particle entrainment data	✓	✓		✓
Surface pressure data			✓	✓
Pressure/force magnitudes			✓	✓
Pressure/force event durations			✓	✓
Impulse concept for particle entrainment		✓		✓
Uniform flow	✓	✓	✓	✓
Flow in the wake of cylinder			✓	✓

Chapter 2. Non-intrusive Method for Detecting Particle Movement Characteristics near Threshold Flow Conditions*

*This chapter is a modified version of the published article: Diplas, P., Celik, A. O., Dancey, C.L. and M. Valyrakis. (2010). "Non-intrusive method for detecting particle movement characteristics near threshold flow conditions" *Journal of Irrigation and Drainage Engineering*, ASCE, Volume 136, Issue 11, pp. 774–780.

Reproduced with permission from ASCE.

Abstract

Bedload measurements comprise an important component in the development of reliable formulae, in an effort to obtain the necessary constitutive relations between amount of transported material and flow parameters. The uncertainty of such measurements is rather well known, being much more pronounced at lower transport rates. This uncertainty stems from the multitude of factors affecting bedload transport and the lack of available trustworthy measuring technologies. Predictions of the limiting case of nearly zero bedload transport, typically reported in the literature as threshold of motion or critical condition, are even more challenging. The purpose of this contribution is to develop a methodology, together with the appropriate instrumentation, for determining the condition of incipient motion. The non-intrusive approach described here proved to be reliable in detecting even the slightest movements of a particle. At the same time, it demonstrates the complexity of the problem due to the highly fluctuating nature of turbulent flow.

1. Introduction

Bed load transport rate fluctuates considerably even in laboratory flumes under uniform, steady flow conditions. These fluctuations are manifested in terms of changes in both amount and composition of the transported material. This is not surprising given that turbulent flow, which is responsible for the instantaneous values of the driving force, is highly variable in space and time (e.g. Diplas et al. 2008). From results reported in the literature (e.g. Kuhnle and Southard 1988), it is evident that the amplitude and period of the fluctuations vary inversely with the magnitude of the average boundary shear stress or, equivalently, with the average bedload transport rate. Since the fluctuations are much more pronounced at low or marginal transport rates, it is expected that the lower bedload transport activity would be more difficult to capture because even the smallest interference with the flow may locally alter the nature of the flow in a crucial way. As a result, developing instrumentation to accurately measure bedload at low transport rates or even to identify threshold of motion conditions remain difficult tasks.

Information about low bedload transport rates and threshold of motion conditions is important for at least the following two reasons: 1) in gravel streams, most flows capable of transporting bedload experience boundary shear stresses that are typically slightly higher than those encountered under threshold conditions, and 2) characterizing a channel boundary as stable, as well as for calculating bedload transport rates using formulas based on the excess boundary shear stress notion, depend on accurately determining the threshold of motion shear stress value.

Knowledge of the near threshold flow conditions is important for a variety of applications ranging from civil and environmental engineering to stream ecology. The

protection of hydraulic structures from scouring processes and the selection of minimum grain sizes for stabilizing the channel bed require that the critical flow conditions be correctly identified. In the case of contaminated bed material, accurate assessment of the maximum flow conditions allowed in the stream without sediment removal and downstream transport to sites of ecological or other significance (e.g. water supply intakes, stream habitat) is vital. Such information is also useful for establishing the maximum flushing flow conditions downstream of reservoirs necessary for the removal of fine sediment without generating higher transport rates that may be damaging to stream's ecology and biology.

Considering the high dependence of bedload transport rate, q_s, on mean boundary shear stresses, τ_0, (Taylor and Vanoni 1972, Diplas 1987), the exact identification of the flow conditions which correspond to threshold or very low bedload transport rates remains a difficult task. As an illustration, the dimensionless Shields' shear stress $\tau_{0*} = \frac{\tau_0}{(\gamma_s - \gamma)d}$ is plotted against the dimensionless bedload transport rate $q_{s*} = \frac{q_s \rho^{1/2}}{d\gamma_s \sqrt{d(\gamma_s - \gamma)}}$ in Fig. 1; where γ and γ_s are the specific weights of water and sediment, respectively, ρ is the density of water, and d is the median size of the bed material. If the functional relation $q_{s*}=f(\tau_{0*})$ is approximated in terms of a power formula ($q_{s*}=a\tau_0{}^b{}_*$, where both a and b are based on regression equations) at different parts of the curve shown in Fig. 1, an exponent of $b\approx17$ will be required for near threshold conditions while a significantly lower value of $b\approx1.5$ will be appropriate for much higher bedload transport rates. It is therefore evident that minimal changes in the near threshold boundary shear stress values could result in substantial changes in bedload transport rates. Therefore, intrusive

instrumentation, such as bedload traps, might not be appropriate for identifying threshold of particle movement conditions and instead nonintrusive techniques should be employed.

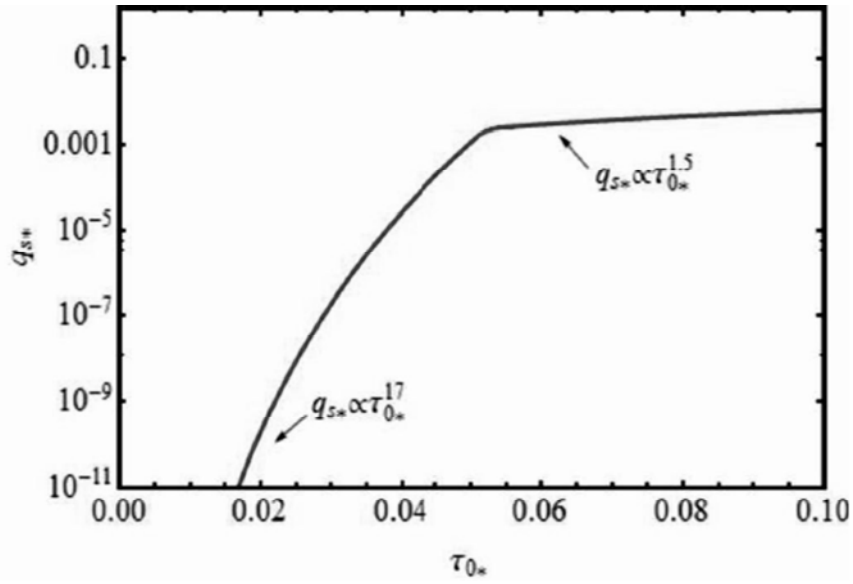

Figure 1. Plot of dimensionless shear stresses (τ_{0*}) against normalized bedload transport rates (q_{s*}).

The focus of this contribution will be on laboratory flumes. A new non-intrusive technique for detecting threshold of motion conditions will be discussed. Results from a controlled laboratory setting help identify the expectations we may have when using the same technique to collect field data in a natural environment that is typically more complex. It can also be used as a basis of comparison for alternative technologies employed for bedload transport measurements.

2. Threshold of Movement Determination

Over the years, several techniques, some of them quite ingenious, have been used for the precise determination of threshold of motion conditions (e.g. Shields 1936, Vanoni 1964, Fenton and Abbott 1977). An extensive overview of prior incipient motion studies has been provided by Buffington and Montgomery (1997). Given the violently fluctuating nature of velocity, pressure and other turbulent flow parameters, as well as the experimental difficulties in detecting the sediment entrainment and/or movement, such a determination remains elusive. Because of the fluctuating forces, some have argued whether such a criterion exists in turbulent flow (e.g. Einstein and El-Samni 1946). Nevertheless, most researchers and practitioners recognize the usefulness of a threshold criterion as a tool in engineering studies.

The authors have observed in well controlled laboratory flume experiments the extreme susceptibility of the localized turbulent flow behavior to even a minute interference. This fact dictates that the precise determination of threshold of particle movement requires the use of non-intrusive techniques. Recent advances in digital photography and image analysis algorithms have made it possible to investigate the initiation of bed material motion, and bed-load transport in such a fashion (see for example: Nelson et al. 1995, Sechet and Guennec 1999, Shvidchenko and Pender 2000, Dancey et al. 2002, Papanicolaou et al. 2002, Böhm et al. 2006, Roarty and Bruno 2006). The development of a non-intrusive method for particle tracking was part of a study at the Baker Environmental Hydraulics Laboratory, Virginia Tech, dealing with the relation between instantaneous turbulent flow velocities and inception of bed material movement. While it is not the objective of this study to expound on the appropriateness of a threshold

criterion concept, it is advocated here that the flow phenomena occurring in the immediate vicinity and upstream of a mobile particle under consideration will dictate its behavior, movement or no movement (Diplas et al. 2008). The study was carried out in a tilting flume, 0.60 cm wide and 20 m long. To reduce the number of parameters affecting the particle movement and facilitate the understanding of cause and effect mechanisms, the entrainment of a single, fully exposed Teflon® ball, having a diameter (d) of 8 mm, resting on four layers of well packed identical diameter glass spheres was examined in fully developed uniform turbulent open channel flow (see Fig. 2).

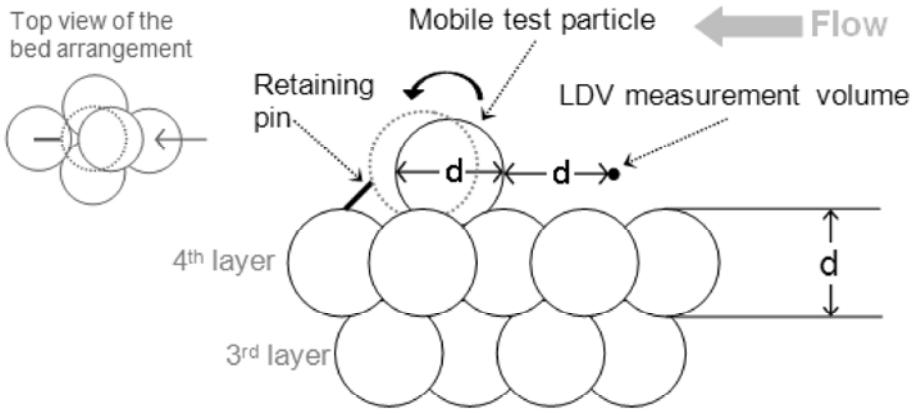

Figure 2. Solitary test particle and pocket geometry. Sketch on the upper left side shows top view and sketch on the right shows side view.

In an effort to identify which turbulent events were potentially responsible for particle entrainment, a two-component laser Doppler velocimeter (2D-LDV) was used to record the streamwise and vertical components of the instantaneous velocity vector one diameter upstream of the center of the test particle, at an average sampling rate between

200 and 520 Hz. A laser based system was developed for detecting small particle displacements as well as entrainment. This system utilizes a He-Ne laser source (output power: 25-30 mW, wavelength: 632.8 nm) and a photo-detector in the manner of a simple "electric-eye" arrangement. The additional laser based system used a principle of operation similar to the forward scatter operation mode of an LDV. The He-Ne laser beam is aligned to be partially incident upon the particle under investigation (see Fig. 3 for the definition sketch). That is, some of the laser beam is allowed to pass entirely through the flume and some of the beam is scattered by the particle. The amount of light that is allowed to pass strikes an opaque boundary on the opposite side of the flume. The light incident on this boundary is viewed by the photo-detector with lens assembly (see Figs. 3 and 4). Very small changes in the position of the particle cause detectible changes in intensity of the transmitted light.

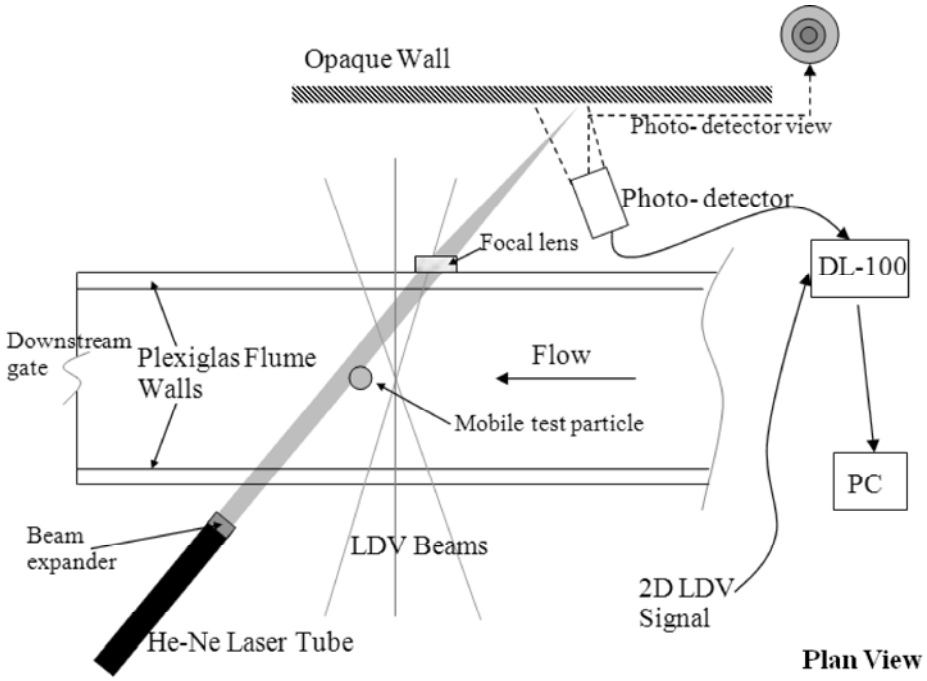

Figure 3. The sketch of the flume, showing the working section and associated instrumentation for the entrainment experiments.

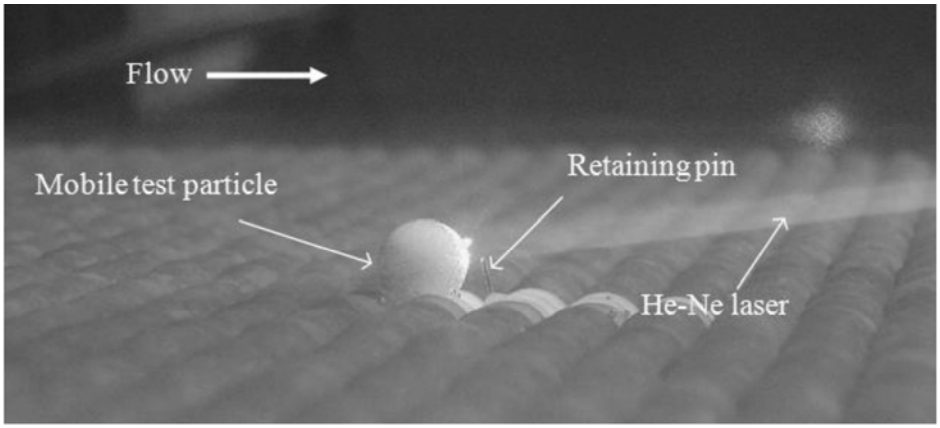

Figure 4. Teflon® test particle, retaining pin, 2D LDV beams, and identical size well packed glass spheres forming the flume bed.

The intensity of the photo-detector signal was recorded simultaneously with instantaneous velocity measurements obtained with the LDV system, using a multi-channel interface signal processor (TSI, Model DL-100). Therefore, the laser-based system requires no triggering in order to collect the photo-detector output. A retaining pin was used to prevent the mobile particle from being completely entrained by the flow (see Fig. 4). This small but important component allowed for continuous records of entrainment episodes without manual intervention. In this manner, statistically significant sets of particle displacement and local flow velocity pairs were obtained for various flow conditions.

The photo-detector output for the particular run presented here varied between -2.65 (V_{max}) and -1.6 (V_{min}) volts, due to the movement of the test particle. A relatively low background noise level ($\pm$ 15 mV) was achieved by minimizing the ambient light during the calibration and test runs. The photo-detector output time series obtained for

typical entrainment events (e.g. rocking and pivoting events) is shown in Figure 5. When the test particle is fully entrained by the turbulent flow forces (e.g. see pivoting signal in Fig.5), it rolls over the valley formed by the pocket arrangement until it reaches the retaining pin, which is located 1 mm away downstream of the rear face of the particle. The photo-detector signal corresponding to the pivoting of the particle is shown in the upper right corner of Figure 5.

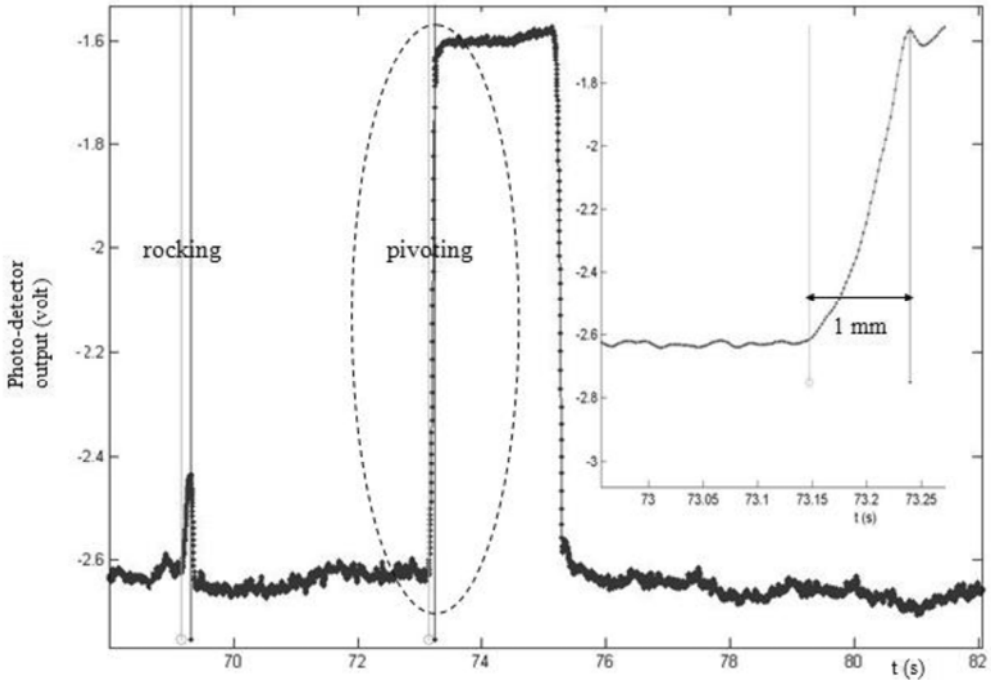

Figure 5. A typical photo-detector output displaying rocking and pivoting sample events of the mobile test particle. Upper right side: Enlarged voltage signal corresponding to 1 mm displacement of the ball in the streamwise direction (dashed ellipse in the main figure).

When the flow conditions are sufficiently strong, the particle is temporarily pushed against the rigid pin. When these conditions subside, the particle falls back to its original pocket. The photo-detector (Volts) output was used to identify within the LDV velocity/time record the instants when a specific level of particle movement had occurred (e.g. see pivoting signal in Fig.5). Once the instants of entrainments were determined, a binary 0/1 signal, with "1" indicating any detectable particle movement was constructed. A representative streamwise velocity time series coupled with the binary entrainment signal is shown in Figure 6. This figure presents a small portion of the local velocity time series, including a turbulent event corresponding to particle dislodgement (instant of particle entrainment obtained from the binary signal is shown with a vertical dashed line).

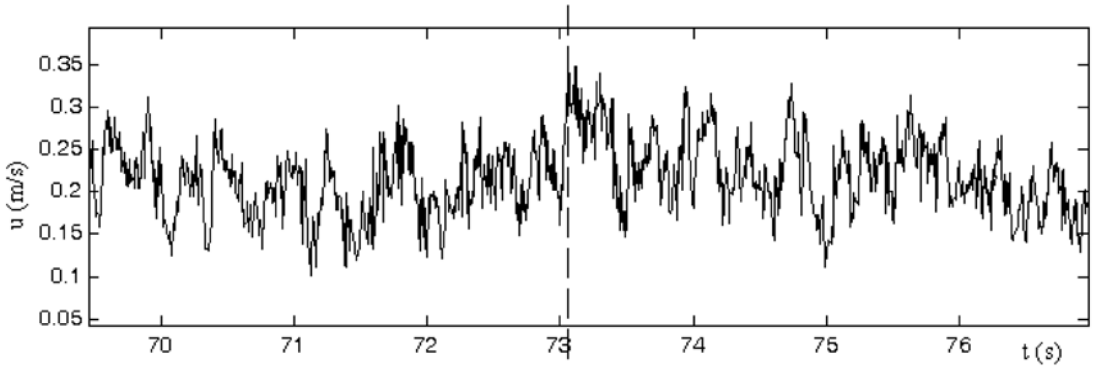

Figure 6. Representative time series of stream-wise velocity (measured at one diameter upstream of the particle, at a sampling rate ~300 Hz). The time instant of the initiation of the test particle motion (matching the pivoting event shown in Fig. 5) is displayed with a dashed vertical line.

A total of 43 particle entrainment events were recorded simultaneously with LDV signal over the 30 minute test period. The ensemble average flow velocity history of flow

events, associated with theses 43 particle entrainment episodes is shown in Fig. 7. The horizontal axis is the relative time with respect to the originally detected instants of entrainment ($t = 0$, the vertical dashed line on the right). The other vertical dashed line on the left shows where the actual instant of entrainment should be, accounting for the time delay based on Taylor hypothesis. The corrected instant of entrainment identifies an ensemble average velocity at which the particle begins to move (~0.26 m/s in these experiments). This magnitude matches the critical velocity deduced from a moment balance on the submerged grain (assuming zero lift and a constant drag coefficient of 0.9). Figure 7 reveals that the grain entrainment events are associated with strong streamwise velocity peaks with relatively short durations.

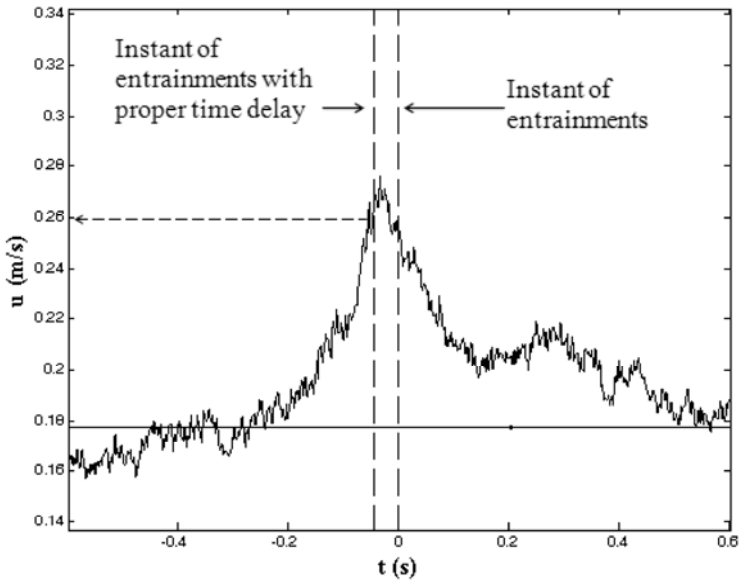

Figure 7. Ensemble average of u vs. relative time and time delay results ($t = 0$ is the uncorrected instant of entrainment). Time delay is due to the distance between the LDV measurement volume and the grain (See Fig.2). A span of ±500 data points for each entrainment instant were used to obtain the ensemble average of u. The horizontal solid line indicates the time-average value of u over 30 minutes.

The calibration of the He-Ne based system was performed *in situ* and resulted in a resolution of 10 μm over the full 1 mm range of motion of the particle. The relationship between the photo-detector output and the position of the mobile particle was determined throughout the entire range of mobile particle displacement. The calibration procedure and the corresponding curve are given in Figs. 8a and 8b. The voltage values for each "test particle displacement step" are time averaged values of 3,000 data points. All of the three calibration experiments were performed under well-controlled ambient light conditions. c1 and c2 were carried out in the flume filled with clean stagnant water, while c3 was performed under the actual experimental conditions (LDV was on, flow was on,

flow was seeded for LDV measurements). Based on the aforementioned calibration calculations, the three raw calibration data were normalized by their usable range. (Usable voltage range = R_v: the acquired signal between the conditions of initial test particle position (resting), V_{max}, and the step right before the full dislodgement, V_{min}, see Fig. 8a). Resulting data indicate the normalized voltage intensity vs. particle displacement steps (Fig. 8b). Data from c1, c2 and c3 follow the same trend, indicating a linear variation of voltage output with particle displacement (Fig. 8b).

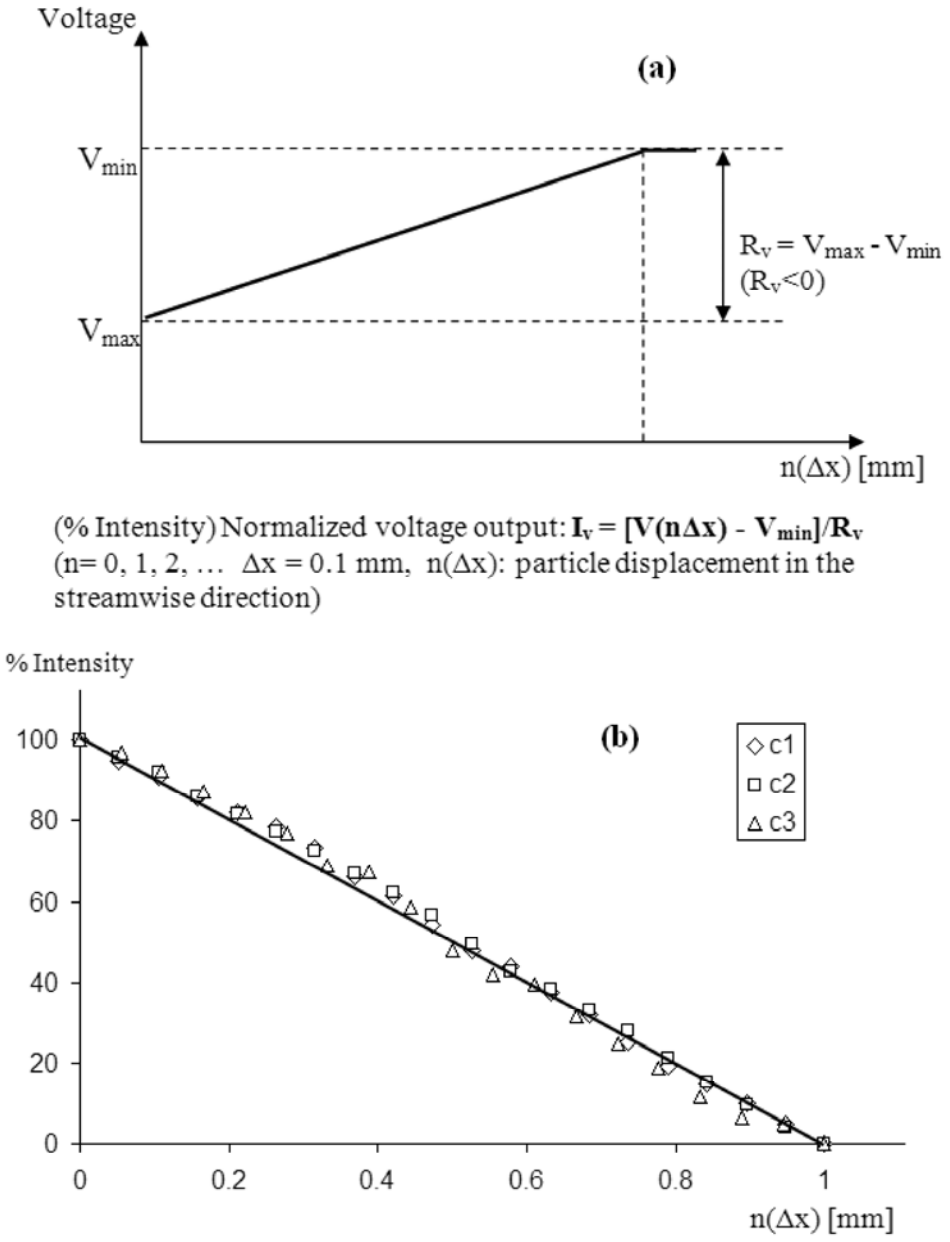

Figure 8. a) Treatment of raw calibration data (Volt vs. displacement). b) Entrainment signal calibration procedure (normalized voltage intensity vs. displacement); c1 and c2 data points from still water and c3 from running water tests.

Owing to the precisely defined 3D pocket geometry and well-defined motion of the mobile particle within the (streamwise-vertical) x-z plane, both the streamwise, $x(t)$, and vertical, $z(t)$, displacements can be obtained from the calibration results and the He-Ne signal, while the instantaneous local velocity record is provided simultaneously by the LDV system. Figure 9 shows the displacement of the center of the particle in streamwise direction as a function of time obtained during one of the experiments. In principle, from $x(t)$ and $z(t)$ the velocity and acceleration of the center of mass of the particle can be determined as functions of t, for each entrainment event. In the present case, pure rolling motion was observed so that the acceleration of the center of mass can be used to directly determine the angular acceleration of the grain as well. With such data, calculation of the net hydraulic force and torque are possible, with appropriate assumptions.

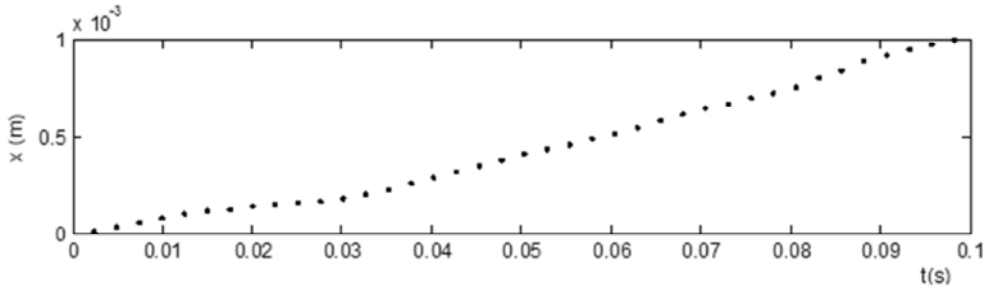

Figure 9. Results from the calibration of the entrainment signal. Displacement of the center of the particle in the streamwise direction.

3. Discussion and Conclusions

For the detection of threshold of motion conditions, it is necessary to employ non-intrusive techniques and objective methodologies for identifying accurately the instant of particle dislodgement. The He-Ne system discussed here appears to satisfy these requirements in well-controlled laboratory conditions. However, this technique is not

suitable for use in the field and for higher bedload transport rates. Furthermore, specifying uniquely the threshold condition remains a difficult task as it depends on the frequency of particle dislodgement in both space and time.

Field conditions are much more complex. Typically, the range of particle sizes present in a gravel stream spans several orders of magnitude, modes of transportation vary widely among streams, up to 10 orders of magnitude (Diplas and Shaheen 2008), and tend to be highly unsteady, suspended and dissolved load concentrations change substantially, and flow depths exhibit a wide range. All of these factors, together with intricate channel topography and life threatening conditions prevailing during floods, make bedload or threshold of movement measurements in a natural setting challenging. It is, therefore, important for new technologies to be tested and calibrated over a wide range of flow and bed material conditions. Range of conditions suitable for the use of this method, as well as the error involved in the measurements, need to be determined to the extent possible. The potential of non-intrusive particle tracking methods can be evaluated in large laboratory flumes and channels with relatively simple geometry.

Acknowledgements

The support of the National Science Foundation (EAR-0439663) for the study presented here is gratefully acknowledged.

References

Buffington, J. M., Montgomery, D. R. (1997). "A Systematic analysis of eight decades of incipient motion studies, with special reference to gravel-bedded rivers" *Water Resour. Res.*, 33(8), 1993-2029

Böhm, T., Frey, P., Ducottet, C., Ancey, C., Jodeau, M. and Rebound, J-L. (2006)."Two-dimensional motion of a set of particles in a free surface flow with image processing" *Experiments in Fluids*, 41(1), 1-11

Dancey, C. L., Diplas, P., Papanicolaou, A. and Balakrishnan, M. (2002). "Probability of Sediment Movement and the Incipient Condition." *J. Hyd. Engr.,* ASCE, 128(12), 1069-1075.

Diplas, P. (1987). "Bedload Transport in Gravel-Bed Streams." *J. Hydr. Engr.,* ASCE, 113(3), 277-292.

Diplas, P. and Shaheen, H. (2008). "Bedload transport and streambed structure in gravel streams." Gravel Bed Rivers VI - From Process Understanding to River Restoration, H. Habersack, H. Piegay, and M. Rinaldi (eds). Elsevier, pp. 291-312.

Diplas, P., Dancey, C.L., Celik, A.O., Valyrakis, M., Greer, K., Akar, T., (2008) "The role of impulse on the initiation of particle movement under turbulent flow conditions". *Science* DOI:10.1126/science.1158954, 322: 717-720.

Einstein, H. A. and El-Samni, E. A. (1949). "Hydrodynamic forces on a rough wall." *Rev. Mod. Phys.*, 21(3), 520–524.

Fenton, J. D. and Abbott, J. E. (1977). "Initial Movement of Grains on a Stream Bed: The Effect of Relative Protrusion." *Proceedings of the Royal Society of London*, Series A, 352, 523-537.

Kuhnle, R. A., and Southard, J. B. (1988)."Bed load transport fluctuations in a gravel bed laboratory channel" *Water Resour. Res.,* 24(2), 247-260

Nelson, J., Shreve, R. L., McLean, S. R. and Drake, T. G. (1995). ''Role of near-bed turbulence structure in bed-load transport and bed-form mechanics.'' *Water Resour. Res.,* 31(8), 2071–2086

Papanicolaou, A. N., Diplas, P., Evaggelopoulos and N., Fotopoulos, S. (2002). "Stochastic incipient motion criterion for spheres under various bed packing conditions" *J. Hyd. Engr.,* ASCE, 128(4), 369-380

Paintal, A. S. (1971). "Concept of Critical Shear Stress in Loose Boundary Open Channels." J. *Hydr. Res.*, 9(1), 91-113.

Roarty H. J. and Bruno, M. S. (2006).”Laboratory measurements of bed load sediment transport dynamics” *J. Waterway, Port, Coastal and Ocean Engineering*, ASCE, 132(3), 199-211

Sechet, P.and Guennec, L., B., (1999). “Bursting phenomenon and incipient motion of solid particles in bed load transport” *J. Hydr. Res.*, 37(5), 683-696

Shields, A. (1936). ‘‘Anwendung der Aehnlichkeitsmechanik und der Turbulenzforschung auf die Geschiebebewegung,’’ Mitteilungen der Preussischen Versuchsanstalt fuer Wasserbau und Schiffbau, Heft 26, Berlin, (in German), [English translation by W. P. Ott and J. C. van Uchelen, Publication No. 167, Hydrodynamics Lab., California Inst. of Technology, Pasadena, Calif.].

Shvidchenko, A. B. and Pender, G. (2000).”Flume study of the effect of relative depth on the incipient motion of coarse uniform sediments” *Water Resour. Res.*, 36(2), 619-628.

Taylor, B. D., and Vanoni, V. A. (1972). ‘‘Temperature effects in flat-bed flows.’’ *J. Hydr. Div.*, ASCE, 98(8), 1427–1445.

Vanoni, V. A. (1964). “Measurements of Critical Shear Stress for Entraining Fine Sediments in a Boundary Layer.” Report KH-R-7, W. M. Keck Laboratory of Hydraulic and Water Resources, California Institute of Technology.

Chapter 3. Impulse and Particle Dislodgement under Turbulent Flow Conditions*

*This chapter is an edited version of the published article: Celik, A. O., Diplas, P., Dancey, C. L. and Valyrakis, M. (2010). "Impulse and Particle Dislodgement under Turbulent Flow Conditions." *Physics of Fluids*, Volume 22, pp. 1–13.

Reprinted with permission from Celik, A. O., Diplas, P., Dancey, C. L. and Valyrakis, M., Physics of fluids, Vol. 22, Page 1-13. Copyright 2010, American Institute of Physics.

.

Abstract

In this study, we investigated the role of turbulence fluctuations on the entrainment of a fully exposed grain near threshold flow conditions. Experiments were carried out to measure synchronously the near bed flow velocity and the particle movement for a range of flow conditions and resulting particle entrainment frequencies. We used a simplified bed geometry consisted of spherical particles to reduce the complexities associated with the variations in the bed and flow details in an effort to identify the underlying dominant physical mechanism. An analysis was performed based on common force approximations using near bed flow velocity. Turbulence fluctuations were treated as impulses, which are products of magnitude and duration of applied force. It is demonstrated that besides the magnitude of the instantaneous forces applied on a sediment grain, their duration is important as well in determining whether a particle will be entrained by a turbulent flow event. Frequency of particle entrainment varied remarkably with minute changes in gross flow parameters. Impulse imparted on the sediment grain by turbulent flow was found to be well represented by a log-normal distribution. We obtained a (log-normal) probability density function (pdf) dependent on only the coefficient of variation of the impulse (impulse intensity). Relation of the impulse intensity to the particle Reynolds number,

*Re**, was established. The sensitivity of the computed impulse to the critical force level, as well as the influence of the critical impulse level on the dislodgement events were explored. Particle entrainment probabilities were found using the derived pdf as well as experimental observations and a good agreement between the two is reported. Implications of the presented impulse concept and our experimental findings for sediment mobility at low bed shear stress conditions are also discussed.

1. Introduction

The incipient motion condition for granular material defines the stability of erodible beds and constitutes the central problem for sediment transport in rivers, coastal areas and atmospheric flows. Shields' deterministic framework[1], employing time-space average bed shear stress to describe the driving hydrodynamic forces near the bed is the most widely used practical tool, and has been for over 70 years.[2] On the other hand, as a result of decades of work, the literature acknowledges the significance of momentary high turbulent forces on mobilizing the sediment grains at incipient conditions.[3-8] These forces occur randomly in space and time due to the turbulent flow near the bed.[9] It is advocated that the movement of a grain begins when the local instantaneous turbulent forces overcome the resisting forces, which are also statistical in nature.[8] Occasional sediment movement is still possible under turbulent flow conditions where the mean hydrodynamic force is not large enough to entrain the particles.[10,11] In addition, Paintal[10], using long observation periods, showed under flow conditions well below conventional critical conditions, such as those proposed by Shields[1,2], that not only the random movements of bed material are observed, but a small increase in the bed mean shear stress causes a

significant increase in the movement of bed material. Paintal[10] reported that at these low stresses the bedload transport rate increases with the 16^{th} power of the boundary shear stress. Helland-Hansen et al.[12] and Hofland[13] also made observations under low shear stress and low mobility conditions; those are in qualitative agreement with Paintal's[10] findings.

Incipient motion criteria utilizing gross flow characteristics, such as those proposed by Shields, do not account for the force fluctuations and therefore are not sufficient to describe the phenomenon at incipient conditions. This view has led many researchers to argue that a unique threshold level in terms of bed shear stress doesn't exist at which the grain movement suddenly begins.[11,14-16]

Many researchers, in an effort to overcome the limitations of the time-averaged wall shear stress approach, have explored the role of turbulent velocity and the resulting fluctuating hydrodynamic forces near the bed on the particle dislodgement, particularly for incipient conditions. Several deterministic and stochastic approaches have been proposed as a result.[17-22] Common in these approaches is the importance of the *magnitude* of peaks in the local flow velocity, the streamwise component in particular, and resulting instantaneous forces acting on individual grains in mobilizing these particles. Despite these efforts and partially due to the experimental difficulties in observing the threshold of sediment movement with synchronized flow measurements, which also lead to subjectivity in defining the bed mobility[2,17,18], the precise determination of the incipient condition remains elusive. Moreover, the nature of the processes that are causing the phenomenon observed by Paintal[10] hasn't been explained by the recent methods so far.

The sensitivity of the interactions between local turbulent flow and mobile sediment to even a minute interference, observed during incipient motion experiments, suggests that the investigation of threshold of particle movement requires the use of non-intrusive particle tracking techniques.[18, 23] Balakrishnan[24], using a video camera together with local flow velocity measurements, provided evidence contrary to the general consensus, and demonstrated that not all local flow velocity fluctuations well above the mean value result in particle dislodgement under incipient flow conditions. A recent study examined this phenomenon further under well controlled laboratory conditions and demonstrated that it is not the magnitude of the applied force alone that serves as the necessary and sufficient condition for particle entrainment but rather the combination of force and duration, or impulse.[25] The implication here is that the turbulence induced momentary peak forces acting on the bed material must last long enough to cause entrainment. Although results reported by Diplas et al.[25] represent the behavior of a test particle in a well controlled environment, this conclusion implies that the impulse potential of a turbulent stream is relevant to the inception of bed material motion, rather than simply the magnitude of the instantaneous forces or time-space-averaged bed shear stress.

The goal of this study is to carry out laboratory flume experiments to further investigate the influence of impulse on entrainment of a single grain for a range of flow strengths and resulting entrainment frequencies. This is pursued by examining long duration data sets of synchronously measured local streamwise flow velocity (and associated impulse values) and the entrainment of a mobile test particle. The former was

measured via the use of a laser Doppler velocimeter (LDV), while the latter was monitored using a laser-based particle tracking technique.

Tests were performed in fully developed uniform open channel flow at near threshold conditions. In this study, in an effort to simplify the phenomenon to its most elemental form and facilitate the development of cause and effects relations (while retaining the physics which dominate), the entrainment of an isolated, fully exposed, spherical particle was examined. The preferred mode of particle movement under these conditions is rolling, consistent with observations made in the field for rounded or semi-rounded particles subjected to near threshold conditions.[4,11]

The impulse concept and the detection of impulses are explained in the following section. The experimental methods are described in detail in Sec. 3. Statistics and pdf of impulses detected in various runs are presented in Sec. 4-A. We discuss in Sec. 4-B and C, the sensitivity of the total number of impulses observed and the number of impulses with a potential to yield particle entrainment to the critical force and critical impulse levels respectively. Following these analyses, the probability of particle entrainment is explored in Sec. 4-D. Implications of our findings to sediment movement at low bed shear stresses are discussed in Sec.5. Conclusions are given in Sec. 6.

2. Impulse Concept

Despite the evidence available in the literature on the dynamical significance of the magnitude of fluctuating local turbulent forces in mobilizing the bed material, the durations over which these turbulent forces act have received no attention thus far with the exception of Diplas et al.[25] They provided evidence that the impulse imparted by near

bed turbulent events has to be larger than a critical impulse level to entrain a sediment grain from rest.[25] Understanding the statistical characteristics of impulse imparted by turbulent flow, rather than just those of the local forces or bed shear stress is essential for describing the incipient bed material motion. In order to detect impulses we used a simple approach in which the force time history is obtained from the local flow velocity, as described in the following section.

A. Impulse Detection

Here, the focus is on a simple setting where the grains are spherical and a mobile particle rests on densely packed identical size particles, as shown in Fig. 1. For the given configuration it is assumed that the forces acting on the mobile particle are submerged particle weight, W_S, and hydrodynamic force, F, assumed to act through the center of gravity of the sphere.[26, 27] Drag force, F_D, is the prevailing hydrodynamic force component, in line with the flow direction. The lift force, F_L, is neglected here since drag dominates grain dislodgement for highly exposed particles.[28, 29]

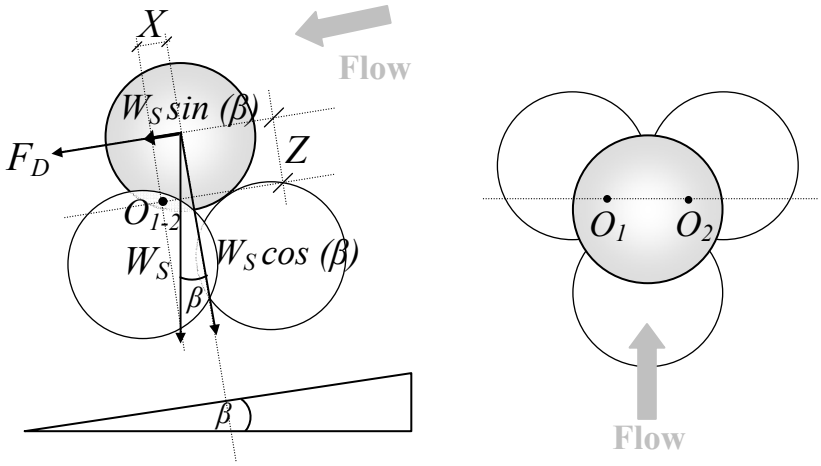

Figure 1. Definition sketch of the forces acting on a spherical particle resting on identical size densely packed spheres, side view (left) and top view (right) of the bed geometry.

Integrating the forcing function, *F(t)*, describing the time history of hydrodynamic force acting upon a particle, between times t_1 and t_2, the impulse, related to particle entrainment, is given as:

$$\text{Impulse} = \int_{t_1}^{t_2} F(t)dt = < F > T \text{ with } F(t) \geq F_{cr} \text{ between } t_1 \text{ and } t_2 \qquad (1)$$

where, $T = t_2 - t_1$ is the total duration of the applied force, $<F>$ is the time average force over duration T, and F_{cr} is the minimum (critical) force required to initiate bed material motion (obtained from the resting equilibrium conditions[18] as discussed later). Since F_D is the only hydrodynamic force component considered here, Eq. 1 is treated in the streamwise direction and corresponding F_{cr} , the critical drag force, F_{Dcr}, is determined as follows.

F_{Dcr} necessary to first move the spherical grain is obtained by a moment balance about the contact points of the test particle with the base particles.[18] This is illustrated in

Fig. 1 where O_1 and O_2 indicate the contact points between the mobile grain and the two downstream base particles. F_{Dcr} can be derived from:

$$F_{Dcr} = f_V W_S [cos(\beta) \frac{X}{Z} - sin(\beta)] \quad (2)$$

where the hydrodynamic mass coefficient[18], $f_V = (1+0.5(\rho/\rho_S - \rho))$, ρ_S is the density of the particle, ρ is the density of water, X and Z are the lever arms, aligned with and normal to the bed respectively, and β is the angle between the channel bed and the horizontal plane. For steady flows, the relationship between F_D and local flow velocity in the streamwise direction, u, upstream of the submerged body is given by

$$F_D = \frac{1}{2} \rho u^2 C_D A \quad (3)$$

where C_D is the drag coefficient and A is the projected grain area perpendicular to flow direction. It is reasonable to estimate the relative level of the instantaneous F_D and its temporal variation through the approximation $F_D(t) \sim u^2(t)$.[28,30] Consequently, the u^2 time history is utilized in the analysis to estimate the drag force time history. The critical condition for the minimum drag force to initiate motion in terms of flow velocity then can be derived using Eqs. 2 and 3 to yield

$$u_{cr}^2 = \frac{2}{\rho C_D A} f_V W_S [\cos(\beta) \frac{X}{Z} - \sin(\beta)] \quad (4)$$

Here f_v is 1.43 for the Teflon® ball that is used in this study and C_D is assumed to be 0.9.[28] The critical u^2 value obtained from Eq. 4 is used in our analysis to detect those events in the u^2 ($\sim F_D$) time series which exceed the minimum required threshold value (u^2_{cr}) as illustrated in Fig. 2.

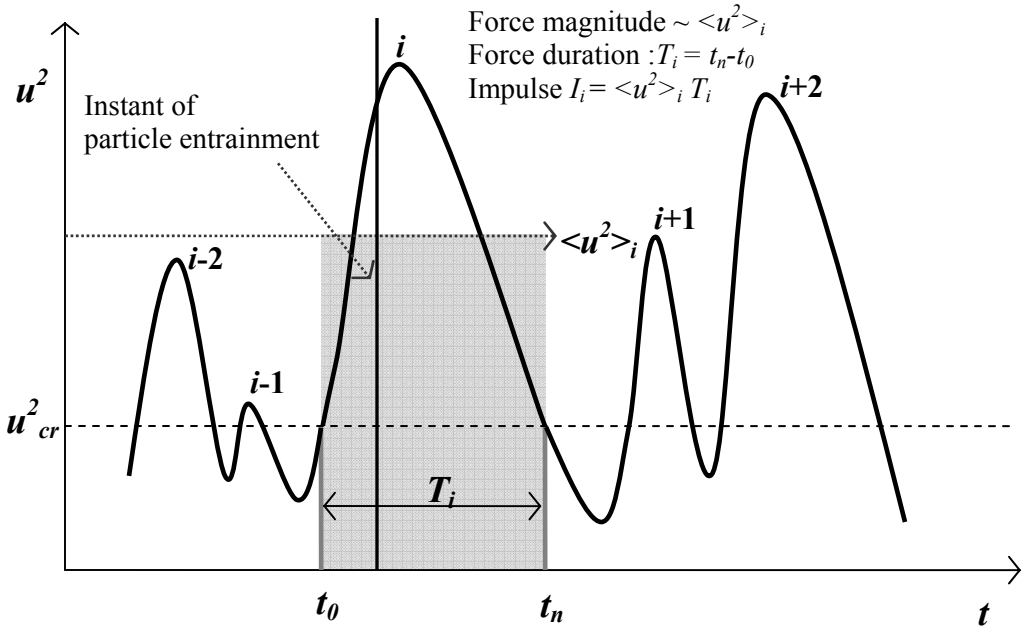

Figure 2. Representation of the impulse events in the u^2 time series. i^{th} event is characterized by $<u^2>_i$ and T_i values, representing force magnitude and duration, the product of which is impulse = $<u^2>_i T_i$ (corresponds to the shaded rectangular area below the u^2 line). t_0 and t_n were determined by interpolating the adjacent data points in the u^2 time series. The vertical line between the t_0 and t_n indicates that the particle movement was observed during the i^{th} event.

All events with $u^2 \geq u^2_{cr}$ are detectable within the u^2 time series together with their times of occurrence and durations, T_i, (duration over which $u^2 \geq u^2_{cr}$). In addition, time-average u^2 values, $<u^2>_i$, can be computed for each such event with $u^2 \geq u^2_{cr}$, representative of the average drag force, $<F_D>_i$ of an impulsive event (angle brackets denote averaging over impulse duration). Consequently, relative impulse event magnitudes $I_i = <u^2>_i T_i$, here-after referred to as "impulse", can be obtained. Those events (I_i) associated with particle entrainments can also be identified experimentally by

simultaneously measuring the particle movement together with *u(t)*. Accordingly, experiments described in the following section were performed to obtain data sets of local flow velocity and particle entrainment pairs.

3. Experiments

Incipient motion experiments were conducted in a 20.5 m long and 0.6 m wide flume located in the Baker Environmental Hydraulics Laboratory at Virginia Tech. Sporadic entrainment events of a fully exposed, mobile Teflon® spherical particle of diameter, d = 12.7 mm, with a specific gravity of 2.3, resting on two layers of well packed identical diameter glass spheres was monitored together with the local flow velocity. The test section was 14 m downstream from the channel entrance to ensure fully developed turbulent flow conditions. Streamwise component of the local flow velocity, u, was measured at one diameter upstream of the test particle along its centerline with a LDV system. Figure 3 illustrates this arrangement. Entrainment of the mobile test particle was recorded utilizing a separate laser-based system that detects its displacement.

Another component of this set-up was a retaining pin located 1.5 mm downstream from the mobile particle (see Fig. 3) to prevent it from being transported downstream from the measurement location. This retaining pin permitted the grain to return to its original position under the action of gravity. This simple but important feature allowed for continuous records of entrainment episodes to be obtained without manual intervention. In this fashion, sets of particle entrainment and local flow velocity data pairs were obtained for various flow conditions.

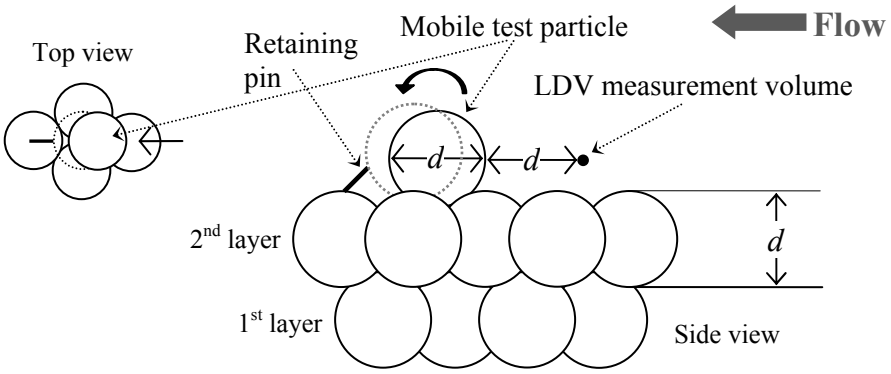

Figure 3. Side view (right) and top view (upper left corner) sketches of the mobile test particle and pocket geometry (diameter of the grains, d = 12.7 mm).

A. Incipient Particle Motion Detection

The particle tracking system used in this study employs a single, low power (25-30 mW) He-Ne laser source and a photo-detector, positioned similar to an "electric-eye" arrangement with the voltage output of the photo-detector directly related to the position of the mobile grain. The calibration of the He-Ne system was performed in-situ using a micrometer and resulted in a resolution of less than 10 μm over the 1.5 mm full streamwise range of particle motion. The LDV and entrainment signals were recorded synchronously via a multi-channel signal processor under various flow conditions during the experiments reported here. The sampling frequency in these experiments varied between 250-700 Hz. A fraction of the photo-detector voltage output from run E1 (see Table 1 for summary) is shown in Fig. 4 together with simultaneous records of u^2 and I_i ($<u^2>_i T_i$). In this example record, both rocking and pivoting of the particle about the contact points are shown. We use the term "pivoting" to indicate those grain movement events which correspond to full grain dislodgement.

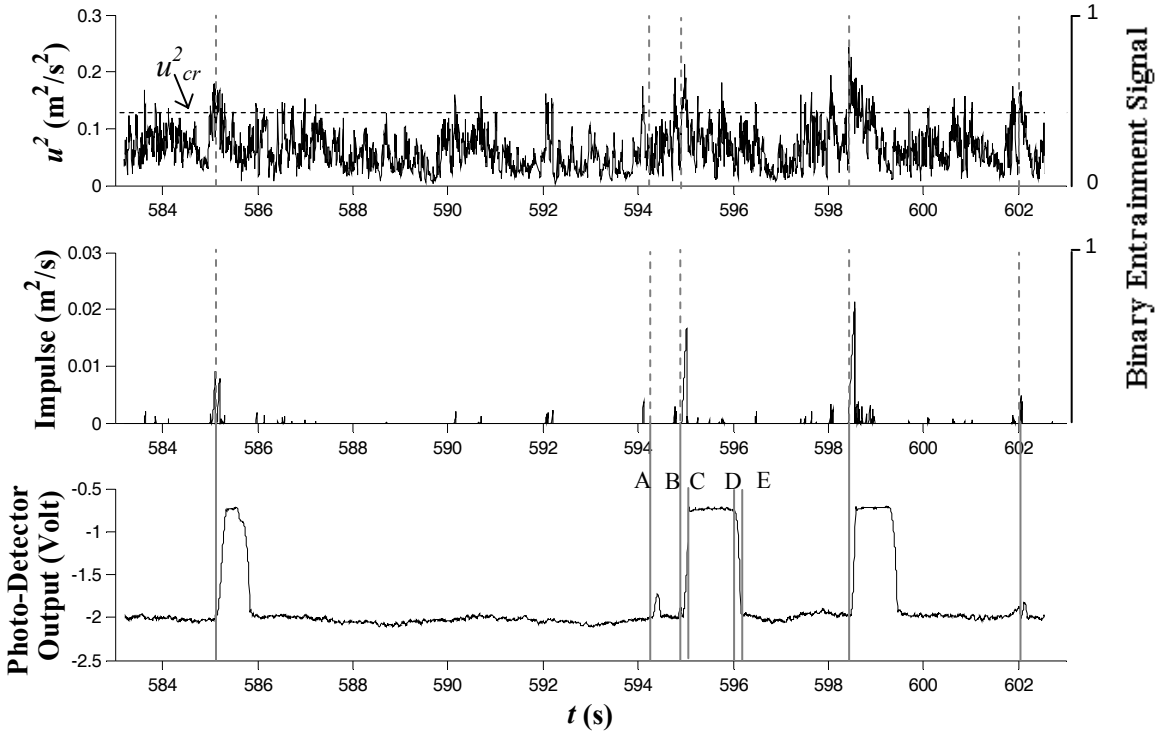

Figure 4. From top to bottom: Representative time series of, u^2, impulse ($<u^2>_i T_i$), and photo-detector output, from run E1. Dashed vertical lines in the top two plots indicate detected particle movements. Secondary vertical axes in the top two plots: binary 0/1 signal. Explanation of the solid vertical lines in the bottom plot: A: beginning of a rocking event, B: beginning of a pivoting event, C: instant when the test particle reached the retaining pin, D: instant when the test particle started rolling back to its original pocket, E: instant when the particle reached its original pocket.

The photo-detector voltage output was used to identify within the u^2 and I_i, time records, the instants when a specific level of particle movement occurred. This is illustrated in Fig. 4. After detecting the instants when the grain moved, a binary 0/1 signal, with "1" indicating any detectable particle movement was constructed (Fig. 4).

Note that the impulse plot (in the middle) of Fig. 4 includes data for events with $u^2 \geq u^2_{cr}$ only.

The typical behavior of the test particle during the experiments was observed to be as follows. When the test particle dislodges, it rolls downstream over the valley formed by the pocket arrangement until it reaches the retaining pin (see Fig. 4, instants B and C respectively). The particle temporarily remains positioned against the pin until the flow induced forces are not strong enough to maintain the position of the particle (Fig. 4, instants C and D respectively). Then the particle falls back to its original pocket as shown in Fig. 4 between instants D and E. We also observed occasional "rocking" events of the test particle in several runs an example of which is shown in Fig. 4, instant A. At these instants, the particle moves within the pocket but does not reach the retaining pin.

B. Experimental Procedure

We conducted flume experiments under eight different uniform flow conditions that resulted in various (time-average) particle entrainment frequencies, f_E. The following experimental procedure was repeated for each flow condition. First, the experiment was run for sufficiently long time to obtain a stable f_E value (~120 min). Subsequently, under the same flow condition, the local flow velocity and entrainment signals were recorded simultaneously for 15 minutes. At the completion of the run, velocity profile measurements were obtained one diameter upstream of the test particle but with the test particle removed from its pocket. The bed slope was kept constant at 0.25% throughout the experiments.

4. Results and Analysis

The analysis reveals that, more than 90% of the particle entrainments in runs E1-E4 and all of the entrainments in the other four runs were associated with events having $u^2 \geq u^2_{cr}$. This high percentage indicates that our assumption about the dominance of F_D on the entrainment of a fully exposed particle is reasonable. It also gives validity to the approach employed here for calculating the u^2_{cr} value, although some uncertainty remains because of the fact that the drag coefficient, C_D, is not precisely known[28].

Table 1 summarizes the flow conditions. It provides the depth average flow velocity, U; flow depth, H; particle Reynolds number, $Re^* = u^* d/\nu$, where u^* is the friction velocity and ν is the kinematic viscosity (u^* was obtained using the Clauser method[31]); Shields stress, $\tau^* = \tau_0/(\rho_s-\rho)gd$, where τ_0 is time-average bed shear stress, g is gravitational acceleration; f_E; u_{mean} which is the time average value of u at a point one diameter upstream of the test particle along its center; and turbulence intensity (TI) given by u'_{rms}/u_{mean}, where u'_{rms} is the root-mean-square of the turbulent velocity fluctuations, u'.

Significant variation in the frequency of grain entrainment occurs with only minute changes in the gross flow parameters. Table 1 shows that a 14% increase in Re^* (~ 35% increase in bed shear stress, $\tau_0 \sim u^{*2}$) is accompanied by a nearly 50-fold increase in f_E. This result is in qualitative agreement with the findings of Paintal[10] and Helland-Hansen et al.[12], and consistent with more limited flume observations of Hofland[13]. It is also noted that the variation in the turbulence intensity measured in the immediate vicinity of the particle for all eight experiments is almost negligible. These findings exemplify the inadequacies of incipient motion models that employ time-space average

flow parameters and suggest that deterministic and stochastic models that depend on local turbulence intensity to define the threshold of particle movement must be used cautiously.

Table 1. Summary of the test conditions for entrainment experiments.

Run	U (m/s)	H (cm)	Re^*	τ^*	f_E (Ent./min)	u_{mean} (m/s)	TI
E1	0.45	7.5	424	0.011	6.93	0.25	0.27
E2	0.43	8.2	413	0.010	5.73	0.24	0.27
E3	0.43	9.0	399	0.010	4.2	0.24	0.26
E4	0.41	7.9	398	0.010	2.06	0.23	0.27
E5	0.42	8.3	385	0.009	1.33	0.23	0.27
E6	0.40	8.6	377	0.009	0.52	0.23	0.26
E7	0.41	9.1	372	0.008	0.24	0.23	0.26
E8	0.39	8.7	364	0.008	0.14	0.22	0.27

Events, for which $u^2 \geq u^2_{cr}$, were obtained for all runs (E1-E8) by performing the analysis described in Sec 2.A via an impulse detection code. The statistics of detected impulse events are presented in Table 2 for E1-E8. The histograms of u^2; $<u^2>_i$ representing drag force averaged over the impulse duration for which $u^2 \geq u^2_{cr}$; T_i which is the impulse duration and I_i, impulse from run E1 are given in Fig. 5. A number of probability distribution functions have been proposed for u^2 in studies concerning the sediment entrainment.[18,19,21] Based on the assumption that the drag force is proportional to u^2, in combination with a Gaussian distribution for u, Papanicolaou[18] proposed a chi-squared distribution to describe instantaneous drag force, which was later modified by Hofland and Battjes[30] to account for the relative turbulence intensity. But the distribution of the impulse, impulse duration or force magnitude associated with impulse events, to the writers' knowledge, has never been examined in sediment transport research. The histogram of impulse is positively skewed with a long tail as shown in Fig. 5. These

distribution characteristics are due to very high magnitude but rare impulse events. The rare impulse events, described by relatively long durations and a range of $<u^2>_i$ values are in fact those responsible for particle movement (see Sec. 4-B). It is important to note that the duration of impulse events (T_i) shows more than an order-of-magnitude variation but a relatively narrow range of $<u^2>_i$ (0.13-0.2 m^2/s^2), in all runs (Fig.5). The variability of event durations is much more pronounced compared to force magnitudes and thus the durations, to a greater extent, influence the impulse values.

Table 2. Summary of the impulse parameters obtained from 15 minute runs.

Run	Impulse $I = <u^2> T$				
	I_{mean} (m^2/s) x10^{-3}	I_{std} (m^2/s) x10^{-3}	δ	Skewness	Flatness
E1	2.39	2.42	1.01	3.3	14.7
E2	2.31	2.29	0.99	3.8	11.1
E3	2	1.9	0.95	3.5	11.4
E4	2.1	2.07	0.97	3.6	12.6
E5	2.11	1.96	0.93	3.8	11
E6	2.16	1.8	0.84	2.9	12.5
E7	1.9	1.66	0.87	2.8	10.9
E8	1.85	1.57	0.85	2.7	9

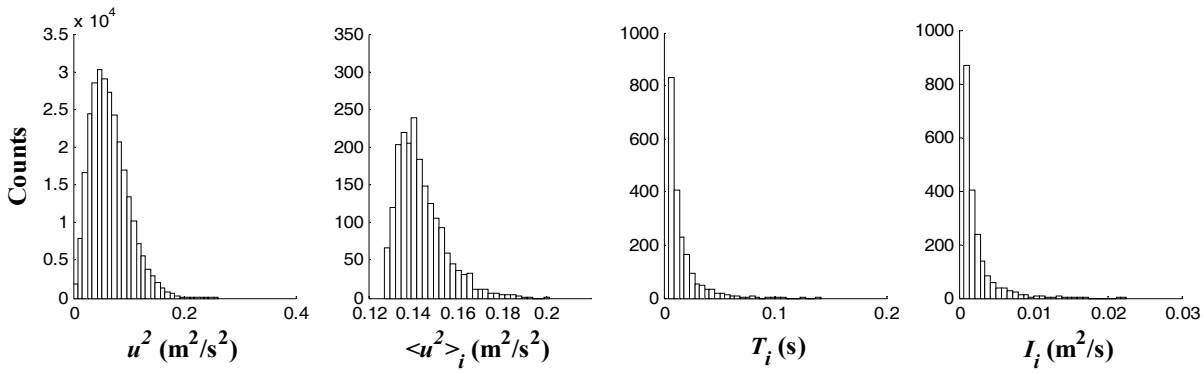

Figure 5. Histograms of u^2, $<u^2>_i$, T_i and I_i from left to right for the run E1. Nearly 280,000 data points (counts) for u^2 and total of 1978 data points for $<u^2>_i$, T_i and I_i are represented in each histogram.

A. Distribution of Impulse

The impulse statistics and histograms indicate that the impulse distribution is heavily skewed. A suitable function that describes data with such properties is the log-normal distribution function. Cheng and Law[32] proposed a log-normal distribution to describe the bed shear stress fluctuations. Another example of the use of log-normal distribution function in sediment research is provided by Wu et al.[33] Recently, Mouri et al.[34] reported log-normality in energy fluctuations obtained from velocity measurements for a wide range of turbulence scales at various flow conditions. It is generally argued that the origin of log-normality lies in the multiplicative stochastic processes, i.e. as a result of independent stochastic variables inherent to turbulent flow phenomena.[34, 35] Impulse, the product of turbulent forces and their durations near the bed may be described by a log-normal distribution. If the impulse is non-dimensionalized with its ensemble average

value, $\hat{I} = I / I_{mean}$, then the log-normal probability density function for the dimensionless impulse, $\hat{I}$ as a function of the impulse intensity, $\delta = I_{std} / I_{mean}$ is given by

$$f(\hat{I}) = \frac{1}{\sqrt{2\pi ln(1+\delta^2)}\hat{I}} exp\left[-\frac{\left(ln\hat{I} + ln\sqrt{1+\delta^2} \right)^2}{2ln(1+\delta^2)} \right] \tag{5}$$

The derivation of Eq. 5 is given in the Appendix. Note that $\delta = \delta_{\hat{I}}$, the latter being the intensity of the dimensionless impulse, $\hat{I}$. Table 2 gives the calculated δ values for all eight runs. A linear relationship exists between δ and Re^* for the limited range of uniform flow conditions tested here (Fig. 6). A linear regression approach provides the following expression

$$\delta = \frac{Re^*}{417} \tag{6}$$

with a coefficient of determination of 0.85.

Figure 7 shows the influence of δ on the distribution of $\hat{I}$ (Eq. 5). Equation 5 approaches a normal distribution for $\delta < 0.2$. For higher δ values on the other hand, the distribution becomes positively skewed. For all δ values that are of interest here (Table 2) and shown in Fig.7, the difference in the right tails of pdfs is clear and significant. These deviations in the shape of the tail with small variations in δ essentially dictate the probability of occurrence of extreme impulse events above a high (critical) level. As it will be discussed in the next section, critical impulse level[25] itself, which has different values in dimensionless form for each run, is also crucial in determining the probability of occurrence of impulse events with a potential to entrain the particle.

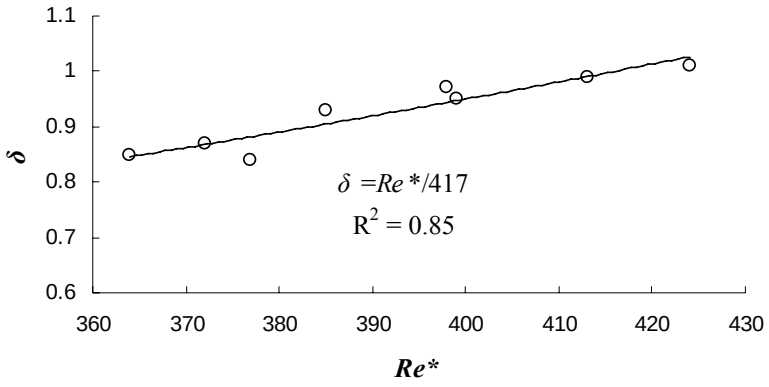

Figure 6. Relationship between impulse intensity, δ, and particle Reynolds number, Re^*.

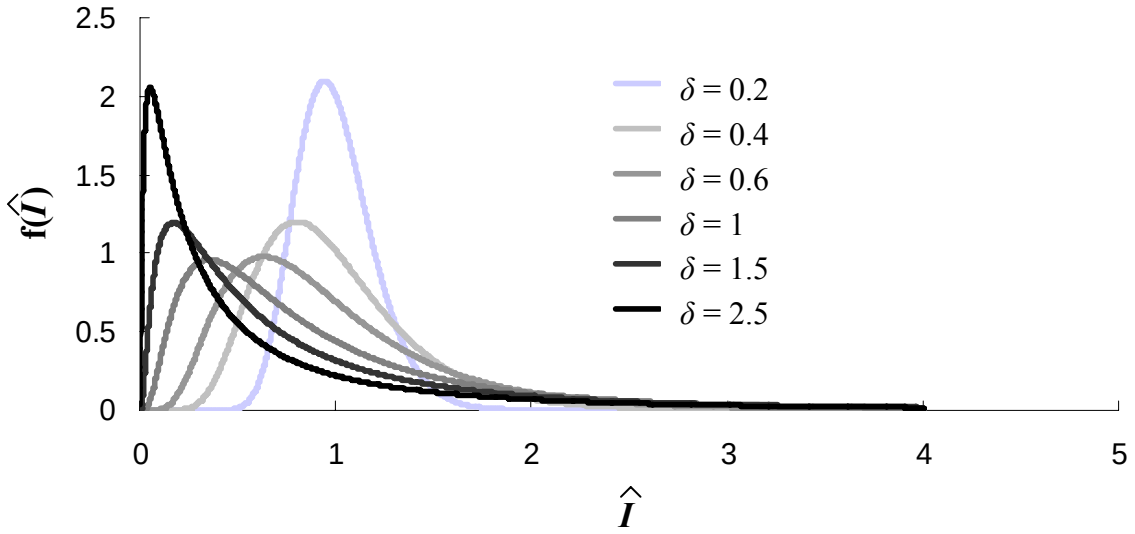

Figure 7. Plots of the function given by Eq. 5 for a range of δ values.

Measured pdfs of impulses, obtained from normalized histograms, are compared with Eq. 5 in Fig. 8 for all eight runs. δ values were determined from the data for each particular run and were used in Eq. 5. It can be seen that the derived pdf describes the data well. In the construction of the pdf's shown in Fig. 8, the tail of the distribution for high impulse is emphasized. This tail characterizes the extreme impulse events and hence it is most relevant to particle entrainment for near threshold conditions, as discussed later

in Sec. 4-D. The selection of the optimum number of bins (~ 25) used to resolve the tail necessarily results in poor resolution at the other extreme of the distribution (the rising leg and peak). In order to show the tail sections better, a semi-logarithmic plot of Eq. 5, together with all the experimental data is presented in Fig. 9 covering the range of test conditions ($\delta = 0.7$ and 1.1). Despite the scatter of data, especially at higher $\hat{I}$ values ($\hat{I} > 3$), Eq. 5 predicts the overall trend well. Since the rising leg and the peak in the pdfs are now involved in rest of the analysis, no uncertainty due to the differences/lack of data points in this section of the pdf was introduced. Therefore no attempts, such as employing arbitrary δ values for different sections of the pdf, have been made.

Furthermore, low amplitude impulse events (where $\hat{I} < 1$) in the rising legs of the pdfs are characterized by combinations of very short T_i and very high $<u^2>_i$ values, or vice versa. Close inspection of the data reveals that the former may not be detected accurately even at turbulent resolving sampling frequencies (i.e. peaks occurring within less than 5 ms). The latter are, on the other hand, extremely rare.

Given that the analysis is sensitive to the features of detected impulses, the following Sections 4-B and C are presented to examine the role of critical u^2 level (u^2_{cr}) on the number and statistics of the detected impulses.

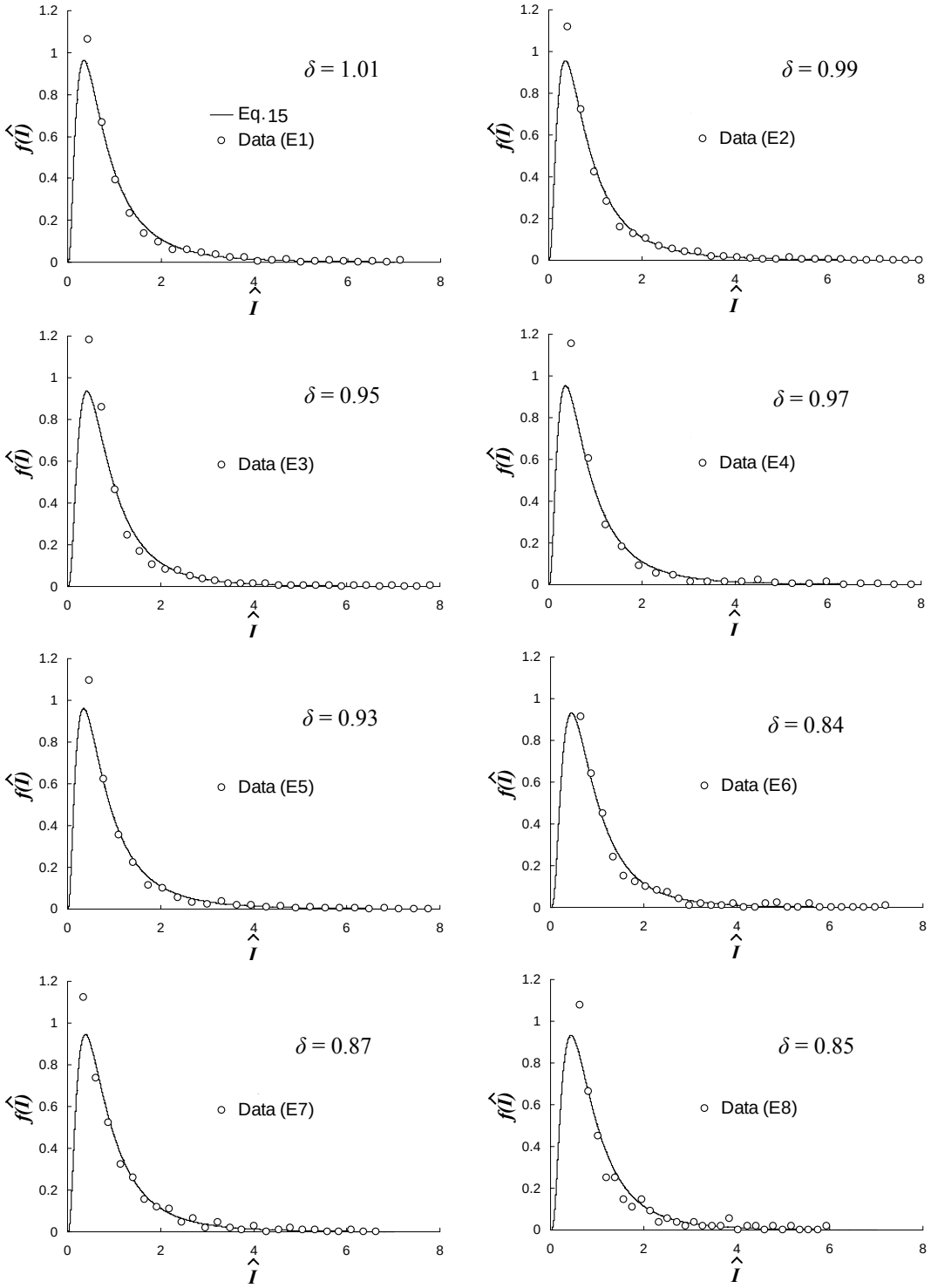

Figure 8. Comparison of Eq. 5 with measured pdfs for E1-E8. Solid lines are used to show pdfs obtained from Eq. 5.

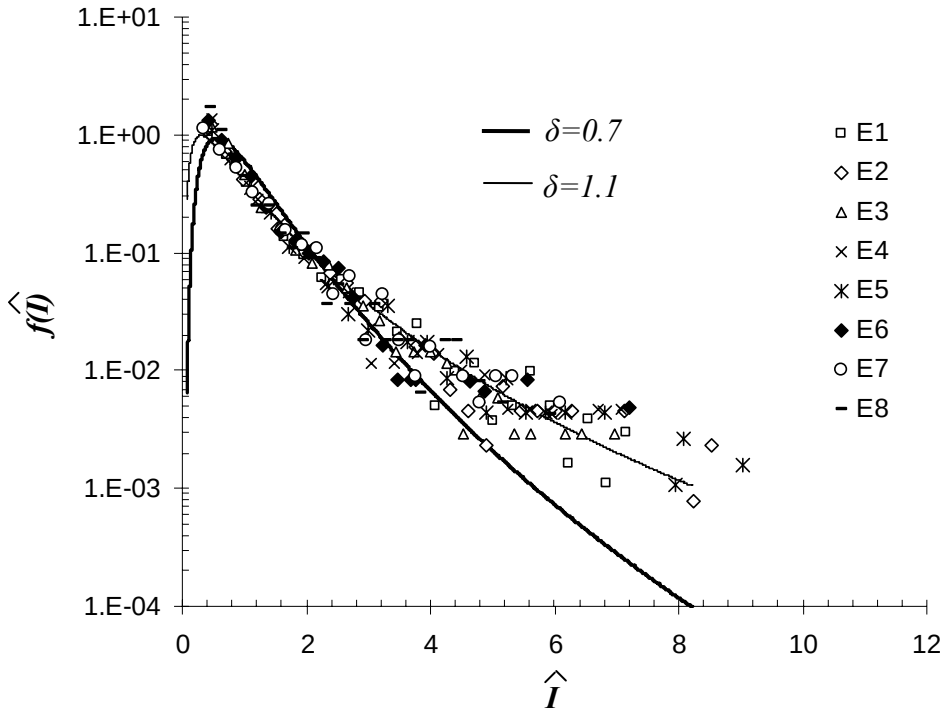

Figure 9. Semilogarithmic plot of measured pdfs from all eight runs. Eq. 5 is also presented with δ=0.7 and 1.1 for comparison.

B. Critical u^2 and Number of Impulses

Values of $\langle u^2 \rangle_i$ are plotted with respect to corresponding T_i in Fig. 10 for all impulse events and including the events associated with full particle dislodgement (the latter are shown in the figure with solid circles) for runs E1 and E4. Plots given in Fig. 10 clearly demonstrate that, in agreement with the findings of Diplas et al.[25] although $F_D \geq F_{Dcr}$ is necessary for the initiation of motion, this condition alone is not sufficient to predict full grain dislodgement. Contrary to common force-balance models and other stochastic approaches, only particular combinations of $\langle u^2 \rangle_i$ and T_i ($u^2 \geq u^2_{cr}$) with moderate to large durations, yielded grain dislodgement. In fact, the most recent incipient motion

models[16,19,20] would significantly over estimate the particle entrainment rate under similar flow and bed conditions. This is true since all of the detected events with $u^2 \geq u^2_{cr}$, for instance all 1978 events in run E1 are routinely expected to entrain the particle in such mechanistic models because these events would cause very high instantaneous drag forces on the particle. On the contrary, our experiment shows that less than 7% of these events caused particle entrainment in run E1. This finding is consistent with Balakrishnan's[24] observations. The total number of impulse events, n_T, for which $u^2 \geq u^2_{cr}$, and the number of impulse events ($u^2 \geq u^2_{cr}$) that yield particle dislodgement, n_E, both observed over a 15-minute sampling period, are given for all runs in Table 3. Note that $n_E = n_P + n_R$ where n_P and n_R are the number of pivoting and rocking events respectively. As shown in Table 3, the difference between the n_T and n_E values is dramatic for all runs. Overall, less than an-order-of magnitude increase in n_T corresponds to two-orders-of-magnitude increase in the n_E. This observation supports the idea that the force magnitude alone is not sufficient to describe the particle entrainment.

Table 3. Number of impulse events and particle movements observed for 15 min. Note that $n_E = n_P + n_R$.

Run	# of impulse events n_T	# of particle movements n_E	
		Pivoting n_P	Rocking n_R
E1	1978	104	29
E2	1554	86	17
E3	1262	63	16
E4	1101	31	15
E5	722	20	8
E6	416	8	3
E7	362	4	4
E8	249	1	1

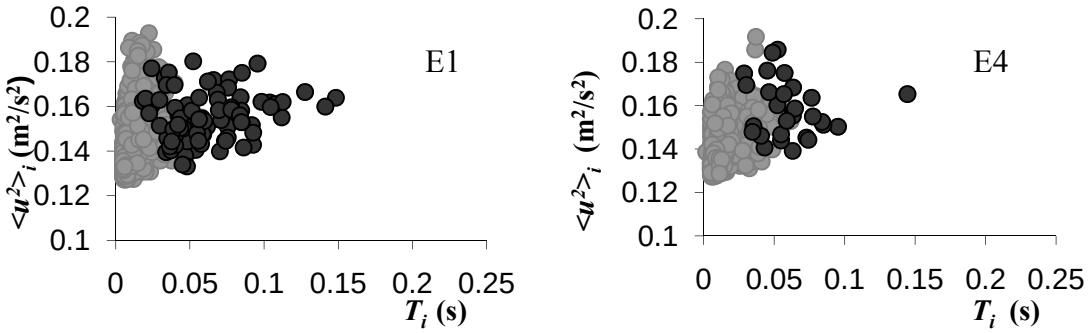

Figure 10. $<u^2>_i$ vs. T_i plots. 1978 data points from run E1 (left), 1101 data points from run E4 (right). Black circles indicate $<u^2>_i$, T_i combinations that are associated with full particle dislodgement (pivoting).

In order to investigate the origins of this remarkable variability in the number of impulses with minute changes in the flow conditions, the role of critical u^2 (u^2_{cr}) level on the number and statistics of the detected impulses was examined. This was done artificially, not by running additional experiments with different grain density or size, but rather by adjusting the level of u^2_{cr} in the analysis of the current series of experiments. This approach is comparable to that by varying the gross flow parameters slightly as was the procedure in the actual experiments. In this analysis, data from run E1 was used. Eight arbitrarily chosen critical u^2 values slightly above and below the original critical level ($u^2_{cr} \pm \Delta u^2$) as illustrated in Fig. 11-a, were selected to identify impulse events, now associated with drag force above the new critical level. Table 4 gives the critical u^2 value that is used; the resulting number of detected impulses, mean and standard deviations of $<u^2>_i$, T_i and impulse respectively; and the impulse intensity. The row with bold font in

Table 4 indicates the results from the conditions where the original critical u^2 obtained from Eq. 4 was used to detect the impulses.

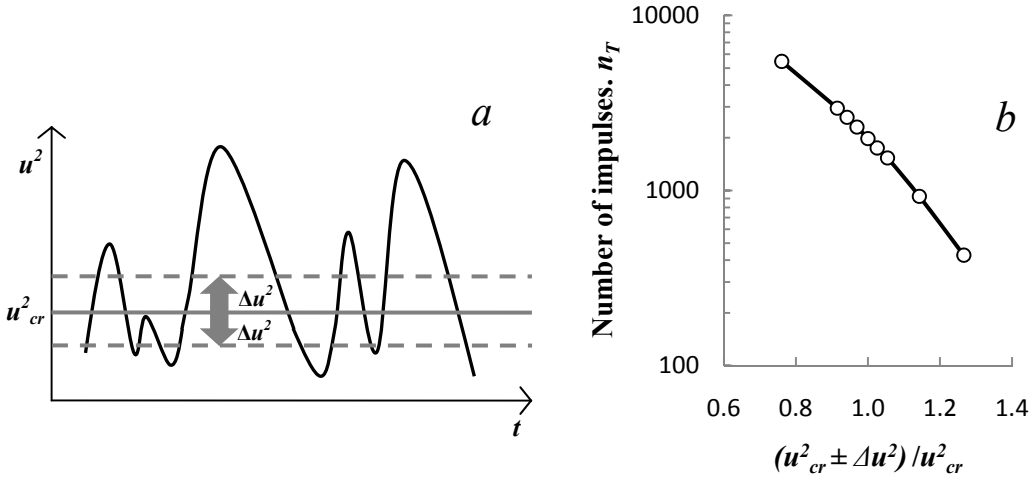

Figure 11. a) Illustration of the approach used for varying the critical u^2. b) Number of detected impulses vs. the ratio of critical u^2 level used to the original u^2_{cr}.

Table 4. Summary of the results from conditions where various u^2 critical values were used for Run E1.

Critical u^2 (m^2/s^2)	Number of detected impulses (n_T)	$<u^2>_{i\ mean}$ (m^2/s^2)	$<u^2>_{i\ std}$ (m^2/s^2)	$T_{i\ mean}$ (s)	$T_{i\ std}$ (s)	$I_{i\ mean}$ (m^2/s)	$I_{i\ std}$ (m^2/s)	δ
0.160	427	0.176	0.010	0.013	0.008	0.0022	0.0016	0.72
0.144	925	0.161	0.010	0.014	0.011	0.0023	0.0019	0.83
0.133	1532	0.150	0.010	0.015	0.013	0.0023	0.0022	0.96
0.130	1748	0.147	0.010	0.016	0.014	0.0024	0.0023	0.96
0.126	**1978**	**0.143**	**0.011**	**0.016**	**0.015**	**0.0024**	**0.0024**	**1.01**
0.123	2302	0.140	0.011	0.017	0.016	0.0024	0.0025	1.04
0.119	2615	0.136	0.011	0.017	0.016	0.0024	0.0026	1.08
0.116	2948	0.133	0.011	0.017	0.017	0.0024	0.0026	1.08
0.096	5456	0.114	0.012	0.021	0.023	0.0025	0.0032	1.28

It is observed that the number of detected impulses is very sensitive to the chosen critical level of u^2. Slightly shifting the critical u^2 level up or down results in a significant

change in the number of detected impulses. The number of impulses increases by an order of magnitude when the critical u^2 level is shifted downward by only about 40% as shown in Fig. 11-b. The latter also corresponds to a hypothetical 25% decrease in the particles density (Eq. 4). This is due to the fact that as the critical u^2 is reduced, those events that were initially below u^2_{cr} now become important (i.e. detectable). The significant increase in the number of impulses in this analysis, similar to what was observed in the original experiments, suggests that the temporal features, resulting from the underlying structure of turbulence, together with the critical u^2 level, plays a crucial role in the significant variation of number of impulse events observed here.

The $<u^2>_{i\ mean}$ as well as $T_{i\ std}$ increase linearly with increasing critical u^2 level while the $<u^2>_{i\ std}$ and $T_{i\ mean}$ decrease. The change in $T_{i\ mean}$ with the critical u^2 level is however much more pronounced compared to the change in $<u^2>_{i\ mean}$. The impulse parameters also do not vary as much as the number of impulses. Impulse intensity ($\delta = I_{i\,mean} / I_{i\,mean}$) increases in a linear fashion as the critical level moves down, mostly due to the decrease in the standard deviation of impulse. As the critical u^2 level approaches the average of u^2, the impulse intensity increases. Together with our earlier findings (shown in Fig. 7), this observation suggests that the distribution of impulse becomes more skewed for relatively lower critical u^2 levels. In the case of higher critical u^2 levels however, the smaller peaks are not detected and the distribution of impulse, including only those extreme events with high impulse magnitudes, will approach a normal distribution.

It is apparent that the number of impulse events (those where $u^2 \geq u^2_{cr}$) is sensitive to u^2_{cr}, but it is also clear that not all impulse events yield grain dislodgement. In the next

section we investigate the relationship between those events that are above critical impulse[25] and u^2_{cr}.

C. Critical Impulse and Number of Grain Entrainments

Figures 9 and 10 imply that the turbulent channel flow contains flow structures with a potential to apply a range of impulse values varying over an-order-of magnitude. A threshold impulse value under the given bed and particle conditions can be defined by identifying an impulse level above which particle entrainment takes place[25]. This constant impulse is approximated by a value of $<u^2>_i T_i$ in the overlap region where both grain movement and no movement are observed on the plot of impulse, $<u^2>_i T_i$, with respect to $<u^2>_i$ (Fig. 12). This region lies between the "impulse" values of 0.0034 m^2/s and 0.0095 m^2/s.

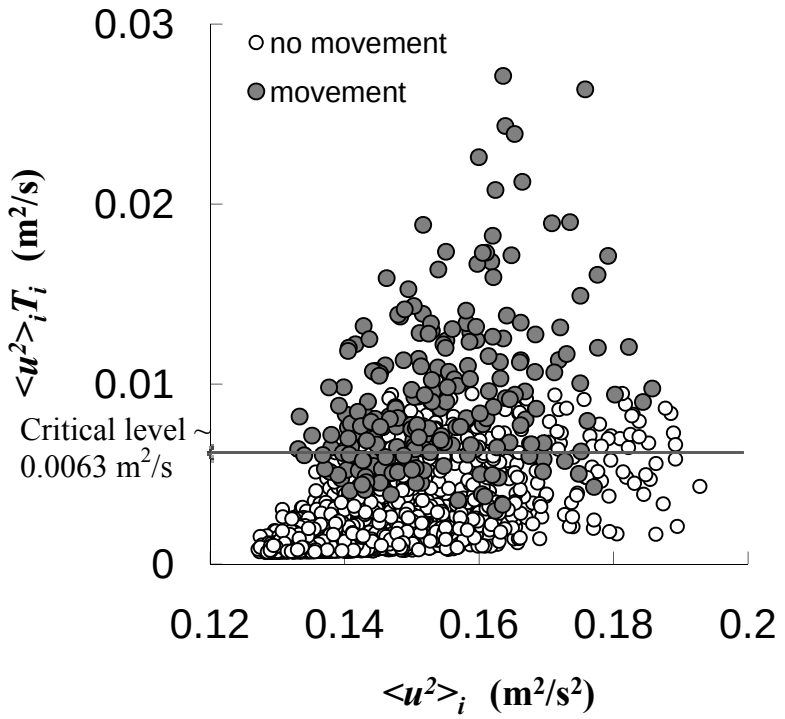

Figure 12. $I_i \sim \langle u^2 \rangle_i T_i$ vs. $\langle u^2 \rangle_i$ plot. The region where movement and no movement areas overlap is shown with a gray band between the impulse values of 0.0034 m^2/s and 0.0095 m^2/s. Horizontal arrow indicates the critical impulse level.

The computed critical impulse level is obtained from the average over this region as shown in Fig. 12 (data from E1-E8 are included). The obtained $\langle u^2 \rangle_i T_i$ value approximates the threshold of impulse (I_{cr}), considering that all of the runs were performed under a single bed configuration and thus under the same threshold of movement condition. The uncertainty in detecting the critical impulse level in our analysis is attributed to the variations in the instantaneous drag coefficient.[28]

In order to investigate the role of the critical impulse level, the previous analysis using artificial critical u^2 levels (Sec. 4-B) was extended. That is, a corresponding critical

impulse level for each critical u^2 level (Table 4) was estimated as follows. The density of the particle corresponding to each of the critical u^2 levels given in Table 4 was determined using Eq. 4. Note that, here the size of the particle remains the same. A theoretical initial velocity, V_{init}, of the particle with the calculated density, as a result of impulse, in the streamwise direction was estimated from the potential energy that the particle gains when it is elevated by an amount of Δz (0.4 mm) normal to the flow direction as it reaches the retaining pin, that is $V_{init} = \sqrt{2g\Delta z}$. For simplicity the energy losses due to friction were ignored for this estimate. Using the change in the linear momentum of the particle, the impulse required (the critical level) was determined for each calculated particle density using V_{init}; and Eqs. 1, 3 and 4. The assumption here is that the impulse determined for each particle density represents a minimum (critical) impulse level that causes a detectible particle movement. The critical impulse level (I_{cr}) calculated in this fashion for the original particle density was 0.0033 m^2/s. We note that this value is near the lower impulse threshold detected using the actual observations of particle movement (Fig. 12).

Using the estimated artificial critical impulse levels, the data for each case in Table 4 were reanalyzed to identify for each critical u^2 value the corresponding number of impulse events above the approximate critical impulse level. The analysis was performed using data from runs E1 and E5. Additionally, the number of impulse events above the critical impulse level of 0.0033 m^2/s was also determined for all eight runs. The results are presented in Fig. 13 where the number of impulse events above critical ($I_i \geq I_{cr}$) per minute are plotted with respect to the total number of impulse events with $u^2 \geq u^2_{cr}$ per minute, for all critical u^2 values tested using the data from runs E1 and E5. In

addition, the number of actual particle movements (n_E) observed in each of the eight runs was also plotted in the figure against the original n_T (Table 4). There is clearly a strong relationship between the number of events above critical impulse and the total number of impulse events, n_T, regardless of the approach used to detect them, provided that the theoretical I_{cr} is used. The functional relationship between the two variables and the coefficient of determination are given in Fig. 13 as an inset. This conformity indicates that the significant increase in both number of impulse events and the number of events above critical impulse with minute changes in either flow parameters or grain density is not a coincidence but a phenomenon inherent to turbulent flow-particle interactions. However, the actual number of ball movements is found to be lower than the number of events above a critical impulse with a potential to move the ball (black circles and plus signs in Fig. 13 are compared). One obvious reason for this difference is the fact that the calculated critical impulse used here is near the lower observed threshold for particle movement as mentioned earlier (Fig. 12).

Next section examines the probability of particle movement taking into consideration the critical impulse values obtained here.

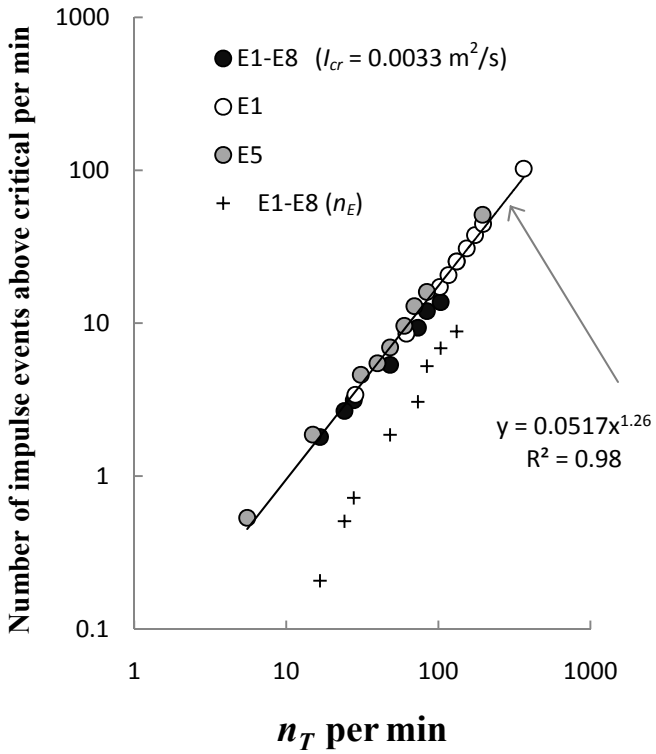

Figure 13. The plot of number of impulse events above critical impulse per min vs. total number of impulse events above critical u^2 per min. Data points with black circles are from all eight runs where a constant I_{cr} was used. White and gray circles indicate results from run E1 and E5 respectively, where various I_{cr} values were used. Data with the plus sign indicates the actual particle movements (n_E) vs. n_T observed in each run.

D. Probability of Particle Entrainment

Probability of particle entrainment has received much attention in the literature.[9,17,18,36] It is commonly argued that the probability of exceeding of a given threshold level is equal to the probability of particle entrainment.[18] Here we hypothesize that the probability, p, of occurrence of flow events that exceed the impulse threshold (Fig. 12) is equal to the probability of particle entrainment, p_E (this concept is illustrated in Fig. 14). The former

can be evaluated directly using Eq. 5 with the critical impulse value (in the form of $\hat{I}_{cr} = I_{cr} / I_{i\,mean}$). To examine the validity of this hypothesis the data for each of the series, E1-E8, were analyzed using three different critical impulse levels obtained from Fig. 12: the upper, lower and average values associated with the overlap region in the figure.

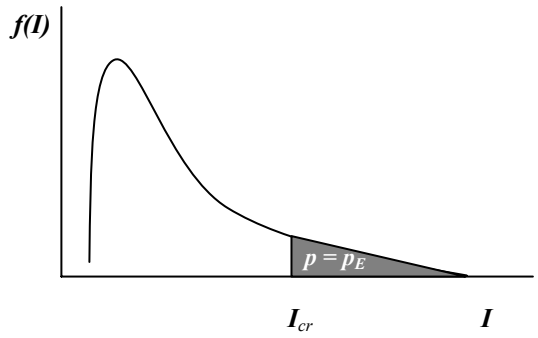

Figure 14. Illustration of the probability analysis. The probability that a flow event will generate a level of impulse that exceeds a specified critical level, I_{cr}, is indicated by the shaded area and is assumed to be equal to the probability of particle entrainment, p_E.

We approximate the probability, p_E by the relative frequency of impulse events that yield particle dislodgement, i.e.

$$p_E \approx \frac{n_E}{n_T} \tag{7}$$

p and p_E values obtained in this fashion are compared in Fig. 15. A good agreement is achieved between the two probability values, especially for higher entrainment rates when the critical impulse is taken as 0.0063 m^2/s (Fig. 12). For comparison, p values obtained using the upper and lower limits of the impulse threshold (Fig. 12) are also

presented with respect to p_E for all runs to reflect the effect on p of the uncertainty in the critical impulse. As shown in Fig. 15, the variation of p with I_{cr} is significant. Nevertheless, the good agreement between p and p_E, using $I_{cr} = 0.0063$ m^2/s confirms that the pdf given by Eq. 5 describes the data well and suggests that, despite the significant variability in particle entrainment frequency, consistent probability values for particle entrainment are obtained near threshold conditions when the frequency of impulse (i.e n_T) is taken into account.

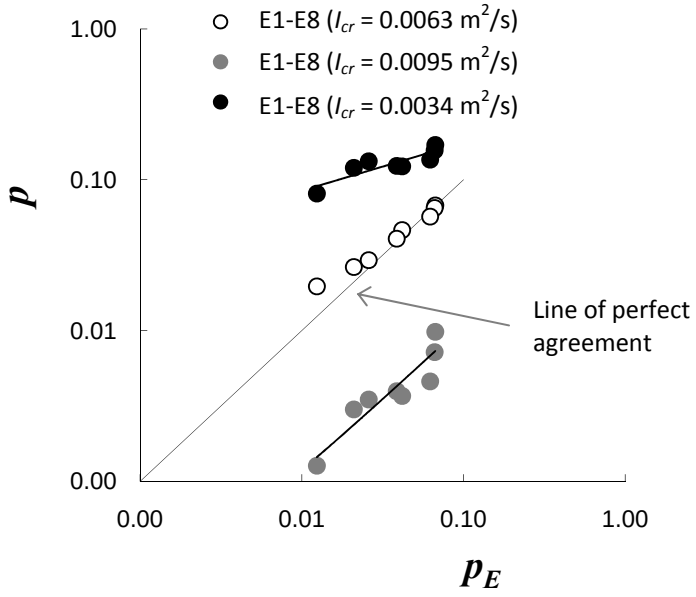

Figure 15. Probability of particle entrainment vs. probability of exceedance of critical impulse.

5. Implications of the Impulse Concept for Low Mobility Conditions

Bedload measurements constitute an important component in the development of reliable formulae relating the amount of transported bed material to the flow parameters. Predictions of the limiting case of nearly zero bedload transport, the threshold of motion or critical condition, are even more challenging. The complexities at very low mobility conditions are associated with flow turbulence and bed microtopography parameters, the former being most prominent. In addition, the paucity of dependable data obtained under low shear stress and low bed material movement conditions hinders understanding of sediment transport processes at incipient conditions. Given these facts, Paintal's[10] well known observation still remains to be explained.

We have shown in this study that for near threshold conditions, the particle entrainment rate increases significantly due to impulse events with only minute increases in the flow strength, interpreted in terms of boundary shear stress or similar parameters. The Shields stress values for instance in our tests varied between 0.008 and 0.011, a change accompanied by nearly two orders of magnitude increase in the number of full particle dislodgements. This behavior exhibits strong qualitative similarities with the observations of Paintal[10] and Helland-Hansen et al.[12]. Figure 16 shows particle movement at low Shields stresses using, as a surrogate measure, the number of impulses per minute above a critical impulse obtained from our experiments (see Sec. 4-C). Dimensionless bed load parameter, q^*, reported by Paintal[10] and Helland-Hansen et al.[12] are included in the same figure for comparison purposes. Despite the variability in flow and bed material parameters employed by Paintal[10] and Helland-Hansen et al.[12] , Fig. 16 shows a nearly two-orders-of-magnitude increase in the number of impulses (with a potential to move

the grains) per minute and in the dimensionless bed load values over a low Shields stress range. The observed similarity in the trends (see the exponents shown in the inset of Fig. 16) helps explain the well known, yet poorly understood, phenomenon observed first by Paintal[10]. It also contributes to the validation of the impulse concept presented here for sediment entrainment at low shear conditions.

It is well understood now that the mean bed shear stress other than being a good descriptor of the mean forces cannot explain the local processes and resulting sediment movement at low shear stress conditions. The magnitude of the local hydrodynamic forces and their distributions form the basis of many stochastic incipient motion models to overcome the complexities of fluid-mobile boundary interactions (i.e. $u^2 \geq u^2_{cr}$). Our results on the other hand clearly show that impulse has far greater dynamical significance in terms of initial sediment movement.

This is clearly seen that the impulse events above critical ($Ii \geq I_{cr}$), rather than the peak forces (with $u^2 \geq u^2_{cr}$), are responsible for particle dislodgement (Fig. 12). Within the given shear stress range, a variability that is in close qualitative agreement with the findings of Paintal[10] and Helland-Hansen et al.[12] is observed in the number of impulse events above critical ($I_i \geq I_{cr}$) and not the number of peak forces for which $u^2 \geq u^2_{cr}$ (see Figs. 13 and 16). We believe therefore that the impulse concept presented here represents a significant step toward establishing incipient motion models with better predictive abilities.

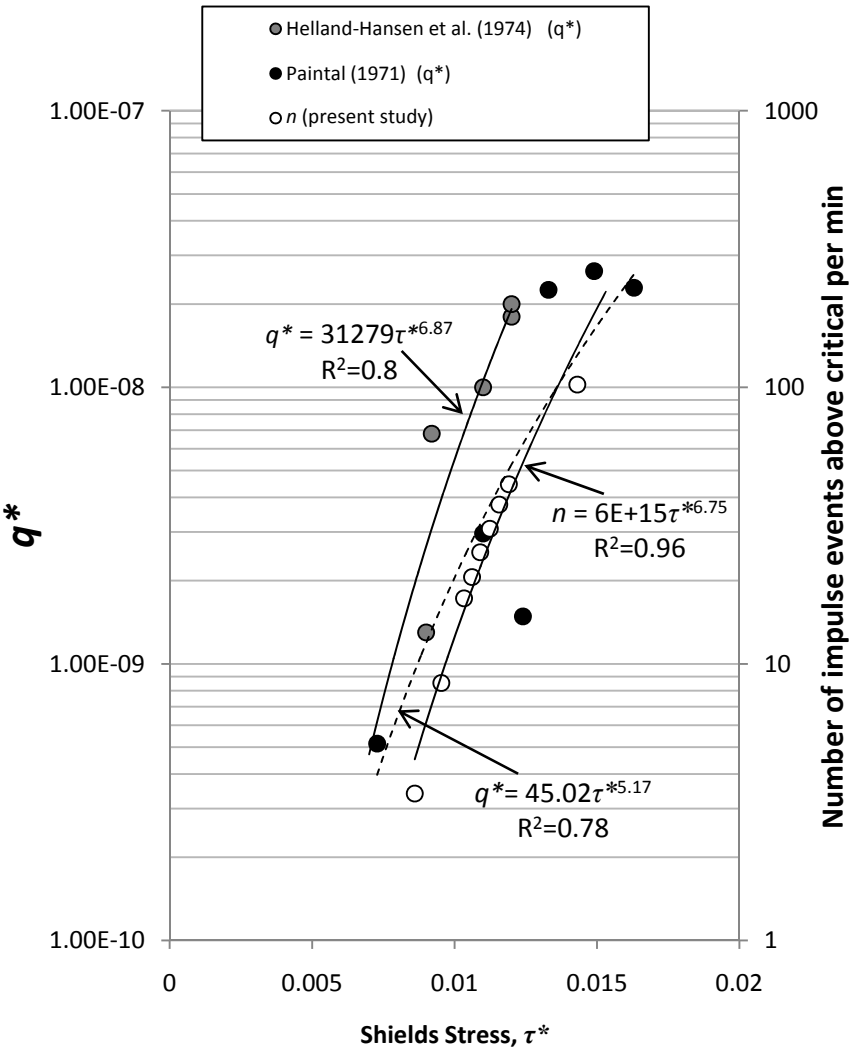

Figure 16. Dimensionless bed load parameter vs. Shields Stress (left *y*-axis) from Refs 10 and 12. Note that data only in the τ^* range between 0.005 and 0.016 were used. The number of impulse events above critical impulse per min ((right *y*-axis) vs. Shields Stress is also plotted.

Because the impulse is the germane criterion for describing the dislodgement of fully exposed as well as fully hidden particle configurations[25], it is expected to remain valid for the more general cases of variable local bed topography. Furthermore, determination of a critical impulse level depends on local bed conditions. In natural

settings, grain size, shape, exposure and packing density vary greatly in a probabilistic manner[8] making also the resistance (critical impulse) of grains to vary spatially. Therefore the threshold of real sediment movement in both space and time requires consideration of both the impulse potential of the turbulent flow and the distribution of critical impulse. Nevertheless, future work will be necessary to demonstrate this result conclusively.

6. Conclusions

We showed for a range of flow conditions and particle entrainment rates that the impulse is a better suited parameter to describe the role of turbulence fluctuations on the particle movement for the given bed configuration and under incipient conditions. Using a particle tracking technique that offers high temporal and spatial resolution in detecting the motion of a single test particle we found that the particle entrainment rate is extraordinarily sensitive to minute changes in the gross flow parameters. This finding is in agreement with well known observations of others available in the literature.

A log-normal distribution was found to describe the impulse data well (Figs. 8-9). Equation 5, for the log-normal distribution, is a function of impulse intensity, δ, alone, which can be determined experimentally or using Eq. 6 for the given Re^* range. Equation 6 is therefore useful for further studies under similar bed and low shear stress configurations.

We demonstrated that the impulse imparted by the turbulent stream on the mobile grain has to be sufficiently large in order to cause dislodgement. Combinations of force duration and magnitude that entrained the particle were observed to be in general above a

critical impulse value (Fig. 12). The durations of applied force varied an order of magnitude for corresponding relatively small range of the force (u^2 values). The resulting strong dependency of impulse values on the duration of applied forcing suggests that the magnitude of drag force is necessary but not sufficient to characterize the threshold of motion.

We also investigated the role of u^2_{cr} (representing the minimum drag force necessary to entrain the particle) on the number of detected impulses. Additionally, the role of critical impulse level on the number of impulse events with a potential to move the grain was examined. The results showed that minute changes in the u^2_{cr} and the critical impulse leads to significant variations in the number of total impulse events and events with a potential to dislodge the grain respectively. This analysis substantiates and helps to explain the observed nearly two-orders-of-magnitude increase in the particle movement rate with 35% increase in the bed shear stress.

The derived pdf (Eq. 5) of dimensionless impulse was used together with an approximated critical impulse level to find the probability of particle entrainment. Probabilities obtained in this fashion were checked against experimentally determined particle entrainment probabilities and a good agreement was achieved when an approximated critical impulse level was used.

Finally, the significant increase in the number of impulse events above critical impulse with small increases in the bed shear stress was found to be qualitatively similar to the significant increase in the bed load transport observed by others under comparable low mobility conditions.

Our results using the impulse concept link the characteristics of turbulent flow to particle entrainment and, despite the simplified bed geometry employed, have far reaching consequences in describing the inadequacies of existing incipient motion models as well as improving our ability to model a wide range of river mechanics and other geomorphology related phenomena.

Acknowledgements

The support of the National Science Foundation (EAR-0439663 and EAR-0738759) and Army Research Office for this study is gratefully acknowledged.

Appendix: Derivation of the Pdf for Impulse

The log-normal distribution for a random variable x is defined by:

$$f(x) = \frac{1}{\sigma\sqrt{2\pi}x}\exp\left[-\frac{1}{2}\left(\frac{\ln(x)-\mu}{\sigma}\right)^2\right] \tag{A1}$$

where μ and σ are the mean and standard deviation of the variable's natural logarithm, $\ln(x)$. x_{mean} and x_{std} representing the mean and standard deviation of the variable x, and

$$c_v = \frac{x_{std}}{x_{mean}} \tag{A2}$$

where c_v is the coefficient of variation of x, μ and σ can be defined as

$$\mu = \ln\left(\frac{x_{mean}}{\sqrt{1+\left(\frac{x_{std}}{x_{mean}}\right)^2}}\right) = \ln\left(\frac{x_{mean}}{\sqrt{1+c_v{}^2}}\right) \tag{A3}$$

and

$$\sigma = \sqrt{\ln\left[1+\left(\frac{x_{std}}{x_{mean}}\right)^2\right]} = \sqrt{\ln(1+c_v{}^2)} \tag{A4}$$

respectively.[37] Equation A1, using Eqs. A2, A3, and A4 can be rewritten as:

$$f(x) = \frac{1}{\sqrt{2\pi \ln(1+c_v{}^2))}x} \exp\left[-\frac{\left(\ln(\frac{x}{x_{mean}}) + \ln\sqrt{1+c_v{}^2}\right)^2}{2\ln(1+c_v{}^2)}\right] \tag{A5}$$

Pdf given by Eq. A5 can be transformed[37] for a new dimensionless random variable $\hat{x}$, which is defined as

$$\hat{x} = \frac{x}{x_{mean}} \tag{A6}$$

The pdf transformation yields

$$f(\hat{x}) = \frac{1}{\sqrt{2\pi \ln(1+c_v{}^2))}\hat{x}} \exp\left[-\frac{\left(\ln\hat{x} + \ln\sqrt{1+c_v{}^2}\right)^2}{2\ln(1+c_v{}^2)}\right] \tag{A7}$$

Equation A7 is dependent only on c_v. Here x is the impulse, $I = \langle u^2 \rangle T$, and c_v is the impulse intensity, δ, given by,

$$c_v = \delta = \frac{I_{std}}{I_{mean}}. \tag{A8}$$

If the impulse is non-dimensionalized as follows

$$\hat{x} = \hat{I} = \frac{I}{I_{mean}} \tag{A9}$$

Eqs. A7, A8 and A9 then yield

$$f(\hat{I}) = \frac{1}{\sqrt{2\pi ln(1+\delta^2)}\hat{I}} exp\left[-\frac{\left(ln\hat{I} + ln\sqrt{1+\delta^2}\right)^2}{2ln(1+\delta^2)} \right] \tag{A10}$$

Note that $\delta = \delta_{\hat{I}}$, the latter being the intensity of the dimensionless impulse $\hat{I}$. Equation A10 shown above is the pdf of dimensionless impulse, $\hat{I}$ as a function of δ.

References

[1]Shields, A. (1936). "Anwendung der aehnlichkeitsmechanik und der turbulenzforschung auf die eschiebebewegung" Mitteilungen der Preussiischen versuchsanstalt fur wasserbau und schiffhau, Heft 26, Berlin, (in German), [English translation by W. P. Ott and J. C. van Uchelen, Publication No. 167, Hydrodynamics Lab., California Inst. of Technology, Pasadena, CA, 1950].

[2]Buffington, J.M., Montgomery, D. R. (1997). "A Systematic analysis of eight decades of incipient motion studies, with special reference to gravel-bedded rivers" Water Resour. Res., 33(8), 1993-2029

[3]Kalinske, A.A. (1947). "Movement of sediment as bed load in rivers" Transactions, American Geophysical Union, Vol. 28, No. 4, pp. 615-620.

[4]Sutherland, A. J. (1967). "Proposed mechanism for sediment entrainment by turbulent flows" J. Geophys. Res., 72(24), 6183-6194.

[5]Heathershaw A.D., and Thorne P.D. (1985). "Sea-bed noises reveal role of turbulent bursting phenomenon in sediment transport by tidal currents" Nature, 316, 339-342

[6]Nelson, J., Shreve, R.L., McLean, S.R., and Drake, T.G. (1995). "Role of near-bed turbulence structure in bed-load transport and bed-form mechanics" Water Resour. Res., 31(8), 2071–2086

[7]Sumer, B.M., Chua, L.H.C., Cheng, N.S., and Fredsoe, J. (2003). "Influence of turbulence on bed load sediment transport" J. Hydr. Engrg., 129(8), 585-596

[8]Kirchner, J.W., Dietrich, W.E., Iseya, F. and Ikeda, H. (1990). "The variability of critical shear stress, friction angle, and grain protrusion in water-worked sediments" Sedimentology, 37, 647-672

[9]Grass, A. J. (1983). "The Influence of boundary layer turbulence on the mechanics of sediment transport" Edited by B. M. Sumer, and A. Muller, pp. 3-17, A. A. Balkema, Rotterdam, Netherlands.

[10]Paintal A. S. (1971). "Concept of critical shear stress in loose boundary open channels" Journal of the Hydraulics Division, 9, 91-114.

[11]Fenton, J.D., and Abbot, J.E. (1977) "Initial movement of grains on a stream bed : The effect of relative protrusion" Royal Society (London) Proceedings, v. 352A, p. 523-537.

[12]Helland-Hansen, E., Klingeman, P.C., and Milhous, R.T. (1974). "Sediment transport at low Shields-paramter values" Journal of the Hydraulics Division, 100(1), 261-265.

[13]Hofland, B. (2005) “Rock & Roll: Turbulence-induced damage to granular bed protections” PhD thesis. Department of Civil Engineering and Geosciences, Delft University of Technology, The Netherlands.

[14]Einstein, H.A., and El-Samni, E.A. (1949). “Hydrodynamic forces on a rough wall” Rev. Mod. Phys., 21(3), 520-524.

[15]Grass, A.J. (1970). “Initial instability of fine bed sand” Journal of the Hydraulics Division, 96(3), 619-632

[16]McEwan, I., and Heald, J. (2001). “Discrete particle modeling of entrainment from flat uniformly sized sediment beds” J. Hydr. Engrg., 127(7), 588-597.

[17]Shvidchenko, A.B., and Pender, G. (2000). “Flume study of the effect of relative depth on the incipient motion of coarse uniform sediments” Water Resour. Res. 36, 619-628

[18]Papanicolaou, A.N., Diplas, P., Evaggelopoulos, and N., Fotopoulos, S. (2002). “Stochastic incipient motion criterion for spheres under various bed packing conditions” J. Hydr. Engrg., 128(4), 369-380

[19]Cheng, N.S., Chiew, Y.M. (1998). “Pick-up probability for sediment entrainment” J. Hydr. Engrg., 124(2), 232-235.

[20]Schmeeckle, M.W., and Nelson, J.M. (2003). “Direct numerical simulation of bedload transport using a local dynamic boundary condition” Sedimentology, 50, 279-301

[21]Wu, F.C., and Chou, Y.J. (2003). “Rolling and lifting probabilities for sediment entrainment” J. Hydr. Engrg., 129(2), 110-119

[22]Vollmer, S., and Kleinhans, M.G. (2007). “Predicting incipient motion, including the effect of turbulent pressure fluctuations in the bed” Water Resour. Res., 43, W05410

[23]Yalin, M. S. (1992). River Mechanics. Pergamon Press, Oxford

[24]Balakrishnan, M. (1997). “The role of turbulence on the entrainment of a single sphere and the effects of roughness on fluid-solid interaction” PhD dissertation, Virginia Polytechnic Institute and State University, Blacksburg, Va.

[25]Diplas P., Dancey C.L., Celik A.O., Valyrakis M., Greer K., and Akar T. (2008). “The role of impulse on the initiation of particle movement under turbulent flow conditions” Science, 322, 717-720

[26]Gessler, J. (1971). “Beginning and ceasing of sediment motion” in River Mechanics, Shen, H.W., Ed., Water Resources Publications, Forth Collins, CO, Chap.7

[27]White, C. R. (1940). "The equilibrium of grains on the bed of a stream." Proc. R. Soc. London, Ser. A, 174, 322-338.

[28]Schmeeckle, M.W., Nelson, J. M., and Shreve, R. L. (2007). "Forces on stationary particles in near-bed turbulent flows" J. Geophys. Res., 112, F02003

[29]Bridge, J.S., and Bennett, S.J. (1992). "A model for the entrainment and transport of sediment grains of mixed sizes, shapes, and densities" Water Resour. Res., 28, 337-363.

[30]Hofland, B., Battjes, J. (2006). "Probability density function of instantaneous drag forces and shear stresses on a bed" J. Hydr. Engrg., 132(11), 1169-1175

[31]Song, T., Graf, W.H., and Lemmin, U. (1994). "Uniform flow in open channels with movable gravel bed" J. Hydraul. Res., 32(6), 861-876.

[32]Cheng, N.S., Law, A.W.K. (2003). "Fluctuations of turbulent bed shear stress" J. Eng. Mech., 129(1), 126-130.

[33]Wu**,** B**.**S**.**, Molinas**,** A**.**, Julien, P.Y.(2004). "Bed-material load computations for nonuniform sediments" J. Hydraul. Eng.,130(10), 1002-1012

[34]Mouri, H., Hori, A. and Takaoka, M. (2009)."Large-scale lognormal fluctuations in turbulence velocity fields" Physics of Fluids, 21, 065107

[35]Limpert, E., Stahel, W.A.,,and Abbt, M. (2001). "Log-normal distributions across the sciences: Keys and clues" BioScience, Vol. 51, No. 5. 341-352.

[36]Dancey, C.L., Diplas, P., Papanicolaou, A., and Bala, M. (2002). "Probability of individual grain movement and threshold condition" J. Hydraul. Eng.,128 (12), 1069-1075

[37]Gumbel, E.J. (1958), Statistics of Extremes. Columbia University Press, New York

Chapter 4. Instantaneous Pressure Measurements on a Spherical Grain under Threshold Conditions

Abstract

We present results from flume experiments where the instantaneous pressures acting on a fully exposed grain were measured simultaneously with local flow velocity in the vicinity of the particle under threshold flow conditions. A simplified bed geometry consisting of spherical particles was used in the experiments to reduce the complexities associated with the variations in the bed and flow details. A spherical particle was instrumented with low-range, high frequency response pressure transducers to measure the surface pressures simultaneously at its front, back, top and bottom. The local flow velocity was measured synchronously with a laser Doppler velocimeter. The emphasis was on determining the characteristics of the flow field with the potential to dislodge a spherical grain under uniform flow conditions as well as under flow in the wake of different size cylinders placed horizontally across the bed in otherwise fully developed flow. The channel and particle Reynolds numbers varied between 31,000-39,000 and 330-440 respectively in these experiments. The relationship between individual pressures, forces approximated from the pressures, and their correlation with local flow velocity patterns was examined. The characteristics of the temporal durations of flow events about the local maxima in the pressures, drag forces and lift forces are presented. Certain patterns in the velocity, pressure, and force time series, which are important for particle entrainment, were identified using a conditional sampling method. The local maxima in the drag force occurred mostly during sweep type near-bed flow events. Strong upward peaks in the lift force were consistently observed before and after the detected peaks in the drag force.

The former peak lift is presumably caused by localized hairpin vortices traveling downstream of sweep type flow structures while the latter is observed during the sweep events. A discussion is included to address the discrepancies between the drag obtained from the instantaneous pressure measurements and that estimated using the conventional quasi-steady drag law.

1. Introduction

Sediment transport by water flow is a complex, stochastic phenomenon that determines the morphological development of river-beds, estuaries, wetlands and coastal areas. The flow condition at which sporadic movement of bed sediment just begins to occur is referred to as the incipient or threshold condition. This condition defines the stability of movable beds. In channel flow, near threshold conditions, the time-averaged hydrodynamic forces are not large enough to cause entrainment of sediment grains. Under these conditions, however, the movement of individual particles is still observed (Paintal 1971, Hofland 2005). In an effort to resolve this apparent paradox, many researchers have advocated that the cause of particle entrainment is the peak fluctuating hydrodynamic forces acting on the sediment bed as a result of turbulence (Kalinske 1947, Sutherland 1967, Heathershaw & Thorne 1985, Kirchner *et al*. 1990, Nelson *et al*. 1995, Sumer *et al*. 2003). On the other hand, more recent findings have provided evidence that not only the magnitude of the peak turbulent forces acting on individual grains but their durations as well have to be considered for determining the incipient conditions for a given bed material size and configuration (Diplas et al. 2008, Celik et al. 2010, Valyrakis et al. 2010).

Incipient motion models, regardless of the framework utilized (e.g. impulse, force or moment balance) require knowledge of the actual instantaneous local forces acting on the grains, their relation with near bed turbulence patterns and their temporal variations for accurate predictions of the threshold of sediment movement from the bed. Einstein & El-Samni (1949) stated that two possible approaches could be used to obtain the hydrodynamic forces. One is to solve for the flow field over the bed surface and to employ statistical tools to calculate from this field the turbulence generated forces on the bed material. Although there are numerical models for solving the governing equations over a fully rough bed (e.g. Stoesser *et al*. 2007, Zeng *et al*. 2008, Derksen & Larsen 2011), full resolution of the forces at realistic Reynolds numbers is not yet achievable. The second approach is to measure directly the forces or pressures acting on individual bed particles. However, because of the experimental difficulties involved, such direct measurements are uncommon.

It is well known that the turbulent flow field at a particular location and the resulting forces acting on the particles are heavily influenced by the upstream and the local bed structure (Bushnell & McGinley 1989, Schmeeckle & Nelson 2003, Hofland *et al*. 2005). It is, therefore, also expected that the probability of entrainment of a mobile grain will change accordingly when the flow field is altered. Celik *et al*. (2010) showed that the frequency of bed particle entrainment at low mobility conditions is extremely sensitive to the minute changes in flow parameters, such as the mean bed shear stress and also to the particle configuration (which pertains to the resistance to motion) under uniform flow conditions. A significant change in sediment movement rate was observed not only as a result of such manipulations in uniform flow conditions but for unsteady

flow conditions as well. Nelson *et al*. (1995) and Sumer *et al*. (2003) reported a considerable increase in the bedload transport under unsteady flow conditions, where the flow field was altered using various methods. They attributed the enhanced bedload transport to the increased turbulence intensity near the bed.

Bed materials, natural and artificial, consisting of sediment of various sizes and shapes, have been used in many flume studies to identify the threshold of particle movement (e.g. Papanicolaou *et al*. 2002, Hofland 2005, Smart & Habersack 2007, Paiement-Paradis *et al*. 2010) and its relation to instantaneous force values obtained from the near bed velocity measurements. Separate pressure or force measurements on rough beds, even though rare, are also available in the literature (Hofland *et al*. 2005, Schmeeckle *et al*. 2007, Detert *et al*. 2010*a* among others) providing information on the link between the flow turbulence and hydrodynamic forces. In their bedload model, Schmeeckle & Nelson (2003) tried to incorporate the complex interaction of flow with individual spherical grains of various sizes by taking into account the instantaneous drag force acting on each grain. They concluded that the typical parameterizations of mean drag and lift forces were useful for bedload estimations but not sufficient, particularly of the lift, to accurately represent the actual instantaneous forces acting on the grains. They also suggested that the pressure fluctuations due to localized vortices which are convected by the near bed flow affect the instantaneous forces significantly.

At high Reynolds numbers, it is reasonable to consider that the instantaneous drag and lift forces result from the pressure distribution over the entire surface of the grain. Therefore, such information is directly relevant to the movement of bed material. Hofland *et al*. (2005), Smart & Habersack (2007) and more recently Dwivedi *et al*. (2010*a*) and

Detert *et al*. (2010*a*) explored the role of fluctuating pressures on particle mobility near threshold flow conditions. Hofland *et al*. (2005) argued that the drag force, estimated using horizontal pressure difference acting on a cubic particle was correlated with both streamwise and vertical components of the near bed flow velocity. They also reported the correlation between the exposure of the particle and the pressures and the occurrence of overall favourable conditions for particle movement during sweep events. Although they did not measure the actual vertical pressure difference, Hofland *et al*. (2005) argued that the streamwise velocity fluctuations of low frequency coincided with high frequency lift force fluctuations. Dwivedi *et al*. (2010*a*) measured both horizontal and vertical pressure differences on a spherical grain under threshold flow conditions and suggested the importance of sweep events in generating concurrently very high drag and lift forces; though the net vertical pressure in their experiments were obtained from the difference between the pressures measured at the top of a test grain and in the porous media under the grain. In another recent study, Dwivedi *et al*. (2010*b*) used the quasi-steady theory to predict the drag force spectra. This approach was used before by van Radecke & Schulz-DuBois (1988), Schmeeckle &Nelson (2003) and Hofland *et al*. (2005). Hofland (2005) suggested that the particle movement was initiated by a strong positive lift force followed by a sweep like event giving the final push (possibly by a peak in the form drag) to the particle. Cameron (2006) reported similar observations and also strong accelerations in streamwise velocity following hairpin vortices near the bed just before the initiation of particle movement. It should be noted that the findings of Hofland (2005) and Cameron (2006) were obtained near threshold flow conditions. Recently, Detert *et al*. (2010*b*) provided evidence that hairpin vortex packages 2-4*d* long in the streamwise direction (*d*

is the diameter of the roughness elements) were observed near the rough bed which had the potential to create low pressure zones on the uppermost layer of the bed. Smart & Habersack (2007) argued that localized vortices and the resulting peak lift forces acting on individual bed materials were the main causes for particle entrainment. These finding are, in general, consistent with the results obtained from a large number of studies concerning smooth and rough wall pressure fluctuations (an extensive review is provided by Robinson 1991) that the negative peak pressures acting on the wall are associated with strong localized vortices with low pressure cores.

The aim of this study was to examine the turbulence generated pressure fluctuations measured directly on the surface of a sediment grain near threshold flow conditions with uniform, fully developed flow and flow in the wake of various diameter pipes positioned spanwise across the bed. A spherical particle was instrumented with pressure transducers to measure the surface pressures simultaneously at its front, back, top and bottom. The behavior of the important peak pressures (as well as pressure gradients), their characteristic magnitudes, durations and their relation to near bed flow patterns and turbulence intensity were examined.

2. Experiments

The experimental investigation was undertaken at the Baker Environmental Hydraulics Laboratory at Virginia Tech. A tilting flume, 14.4 m long, 0.6 m wide and 0.3 m deep, with Plexiglas side walls was used for the experiments. A Cartesian coordinate system (x, y, z) where x is streamwise along the flume axis, y is spanwise across the flume, and z is perpendicular to the flume bottom was adopted in this study.

Three different reaches in the flume, characterized by different materials and/or sizes were used. A top view sketch of these reaches is given in Fig. 1. The first 10.4 m of the flume was covered with natural gravel (d_{50} = 25 mm, where d_{50} is the median sediment size). The next 1.5 m section was covered with three layers of glass beads with a diameter, d, of 8 mm and a specific gravity of 2.54. The last 2.5 m reach near the flume exit was covered with two layers of 12. 7 mm diameter glass beads (specific gravity 2.54). The thickness of material covering the flume bed was kept at an average level of 23 mm (±1 at the 8mm glass bead section and ±3 mm at the natural gravel section) throughout the 14.4 m flume length. The bed slope was kept constant at 0.25% throughout the experiments.

To avoid water surface drawdown near the flume exit and maintain uniform flow depth, steel rods (with a diameter of 8 mm) were placed at the downstream end of the flume (Balakrishnan 1997). The rods were mounted horizontally in rails installed near the tailgate structure. Flow discharge was controlled by a variable speed pump.

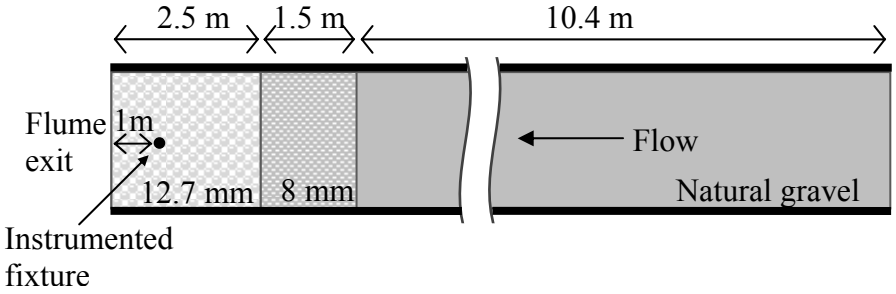

Figure 1. A sketch of the different flume sections (top view).

Pressure fluctuations on the surface of a spherical grain were measured using an in-house custom designed fixture attached to the flume bed along its centerline. The

fixture, located one meter upstream from the flume exit and 4 m downstream of the transition between the natural sediment and well-packed spherical bed, is an instrumented sphere, 12.7 mm in diameter, secured on top of three identical size base balls, arranged in a hexagonal densely packed structure, consistent with the surrounding bed grains (Fig. 2).

The fixture was designed, built and installed such that the tubing system for pressure measurements was completely hidden within the instrumented grain and supporting base structure as shown in Fig. 2(*a*). Solid brass spheres (deviation from spherical form: 0.005 mm, Small Parts Inc.) and brass tubes were fine-machined and used to construct the fixture. First, a small spherical cap (3 mm height) was removed from the solid brass ball along a cutting plane (Fig. 2(*b*)). The interior of the remaining brass ball was machined out through this plane face. Pressure tap holes, located in the front (facing upstream), p_1; back, p_2; top, p_3; and bottom, p_4, of the instrumented sphere were drilled. The pairs "p_1 and p_2" and "p_3 and p_4" are opposite points through the center of the sphere (i.e. antipodal points), so situated that a line drawn from one point to the other for each pair forms a straight line in the streamwise and vertical (stream-normal) directions respectfully when the grain is placed in the flume bed (Fig. 2(*c*)). The size of these holes matched the outer diameter of the brass tubing, which is 1.58 mm. The inner diameter of the brass tubing, and the pressure taps is 1 mm. In addition, outlets with the same diameter as the outer diameter of the brass tubes were drilled through the points where the supporting three base brass balls would be in contact with the instrumented grain in a closely packed arrangement. Then the tubing was installed interior to the instrumented grain (Fig. 2(*b*)). All 4 tubes for tap holes, $p_{1\text{-}4}$, exited the grain from the points where the supporting base grains were in contact with the instrumented particle.

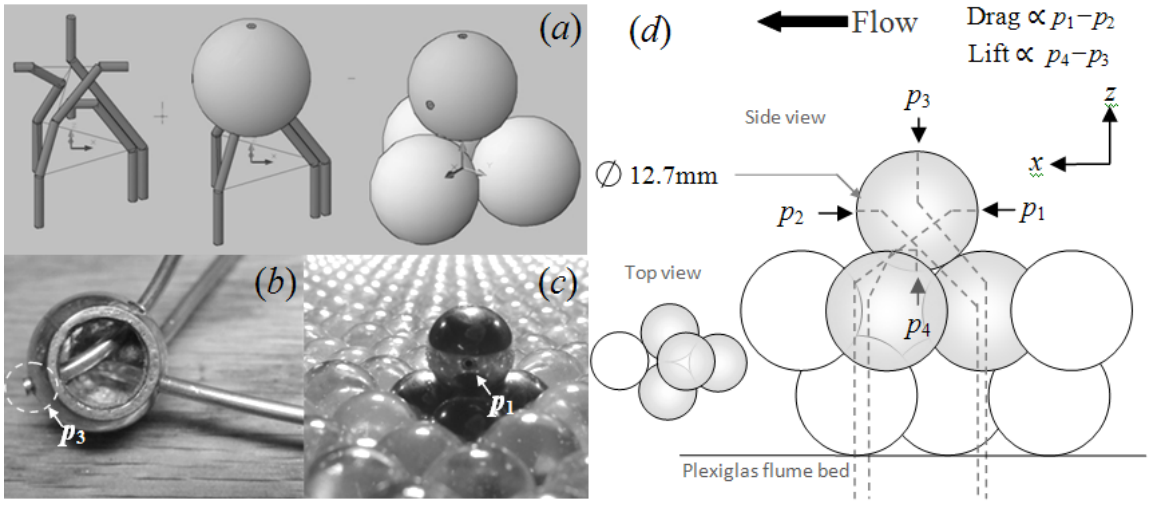

Figure 2. Instrumented fixture. (*a*) Drawings of the fixture during design process. (*b*) Photo of the fixture during assemblage. Dashed circle indicates the pressure tap on the top of the grain before it was trimmed. (*c*) Photo of the fixture installed in the flume bed looking upstream. (*d*) Definition sketch for the pressure measurement points and bed geometry. Dashed lines indicate the brass tubing lines. The Cartesian coordinate system used in this study is shown in (*a*) and (*d*).

With four tubes and only three supporting points, two of the tubes were passed through one contact point (see Figs. 2(*a*) and 2(*b*)). The interior of the instrumented grain (i.e. the gap between the tubes, see Fig. 2(*b*)) was filled with aluminum to support the tubes inside. A separate but precisely matching spherical cap was made and welded on to the plane face of the instrumented grain to complete the sphere. Tubes stemming from the pressure tap holes ($p_{1\text{-}4}$, Fig. (2*b*)) were trimmed and the entire grain was smoothed for the final product to have a completely spherical outer surface as shown in Fig. 2(*c*).

The protruding tubes from under the instrumented grain passing through the contact points were installed interior to the supporting brass balls (Fig. 2(*a*)) through pre-machined holes. All 4 brass balls were then welded together at their natural contact points without introducing any blockage to the flow through the porous bed. The final design had one end of the brass tubing, the pressure taps (p_{1-4}), flush with the surface of the instrumented sphere and the other end stemming from underneath the supporting base spheres to be connected to the pressure transducers.

The configuration of the flume test section used here was identical to that of earlier experiments described by Celik *et al*. (2010) that monitored the entrainment frequency of a mobile Teflon® ball with a diameter of 12.7 mm, and a specific gravity of 2.3. Such simplified bed geometries, where a fully exposed spherical grain is resting on densely packed identical size spheres have been used by other researchers in sediment transport research (Ling 1995, Papanicolaou *et al*. 2002, Cheng 2002, Ancey *et al*. 2006). Particularly unique in this study is the measurement of the surface pressure on the bottom of the sphere, simultaneously with the top, front and rear surface pressures.

2.1 Devices and Methods for Experiments

We used four Honeywell, Sensotec FP-2000 series gage pressure transducers with a full-scale (F.S.) pressure range of 25.4 cm of water column (corresponding to 2,450 N/m^2 and 5 V output), 0.1% F.S. accuracy from a best fit straight line for an operating temperature range between -40 °C and 240 °C to measure the pressure fluctuations.

Analog voltage outputs from the pressure transducers were digitally sampled and recorded using a 16-bit data acquisition board (National Instruments - DAQPad-6015

with a SC-2345 series signal conditioning unit) and LabVIEW software. A resolution of 0.076 mV (~0.038 N/m^2) is specified for the data acquisition board. The transfer time of digital pressure signal from the data acquisition system to the computer was on the order of nanoseconds ensuring that there was negligible or no phase delay between the simultaneously measured pressure signals (p_{1-4}).

Streamwise and vertical velocity components of the near-bed flow velocity, u and w respectively, were measured with a 2D laser Doppler velocimeter (LDV) system. The ellipsoidal LDV measurement volume, with estimated dimensions of 100 μm, 100 μm and 300 μm in the streamwise, vertical and spanwise directions respectively, was located one diameter upstream of the instrumented grain along its centerline. This location coincides with the x and z coordinates of the center of the pressure taps in the front and back of the instrumented ball. A traverse system was used to systematically position the LDV measurement volume within the flume with an accuracy of 0.002 mm.

LDV signal was digitally sampled and recorded using TSI IFA 755 (burst correlator) signal analysis system. The error in the velocity measurements due to uncertainty in fringe spacing estimations was calculated to be no more than ±1.5%. Average sampling frequencies for the flow velocity measurements varied between 250 Hz and 700 Hz.

Separately measured pressure and velocity signals were synchronized as follows. A TSI DL-100 external input module, with a 16 bit analog-to-digital converter and 50 kHz sampling frequency coupled and registered the analog voltage output from one of the pressure transducers (p_1) with valid LDV signals (u and w) during the signal acquisition process while the recording of pressure signals (p_{1-4}) using the NI- DAQPad-6015 data

acquisition board was performed in parallel. This arrangement enabled coupling the velocity and pressure signals (via p_1) with a delay (due to the separate measurement chains) of less than 20 microseconds.

Flow depth measurements in the flume were obtained using a metric ruler attached to the Plexiglas flume wall at a location near the fixture. The depth was measured at 2 min intervals over 15 min sampling duration for each test. The maximum error in an individual flow depth measurement was ±0.5 mm. Average depth values over the sampling durations were used for the analysis. The next two sections describe the static calibration and dynamic performance tests of the pressure measurements.

2.2. Static Calibration Test

Pressure transducers were first calibrated under static loading conditions. This was achieved by recording the voltage output from each transducer under known static pressures using the 16-bit data acquisition board. The transducers were attached to the bottom of a Plexiglas box (25.4 cm x 25.4 cm x 30 cm) and the static calibration was performed over the range of 0 to 23.6 cm of water column by measuring the output voltage of the transducers corresponding to various water levels in the box. This box is shown in Fig. 3. Sampling rate and duration for individual static load tests were 250 Hz and 2 min respectively.

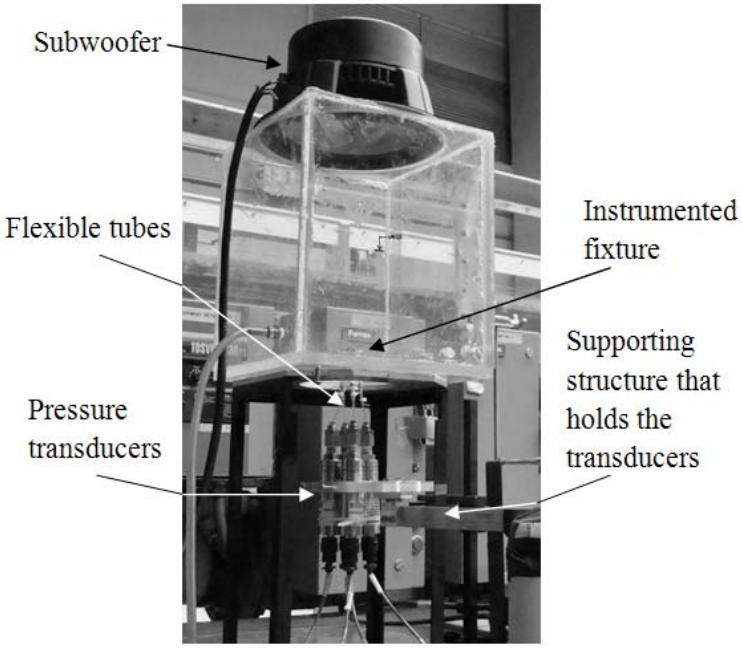

Figure 3. Photo of the test rig used for the static calibration and dynamic performance tests.

The pressure transducers we used exhibited an initial (zero gauge pressure) offset voltage. These inherent DC offset voltages were measured for each transducer before each static calibration and before each flume test. Representative DC offset level for a transducer (#2 used for p_2) is shown in Fig. 4. The static calibration revealed a linear response with static calibration factors (mV/cm of water column) for all transducers. Figure 4 gives the calibration data and the best fit line. Compared to the results obtained from all the pressure transducers, this data set exhibits the maximum deviation from the best fit straight line. The maximum residual error for transducer #2 was found to be 7.5 mV (~0.38 mm of water column or 3.72 N/m^2) which is 50% higher than the value of 5 mV reported in the transducer specification sheets (see inset in Fig. 4). Therefore this new value of 3.72 N/m^2 is considered to be the resolution for the pressure measurements.

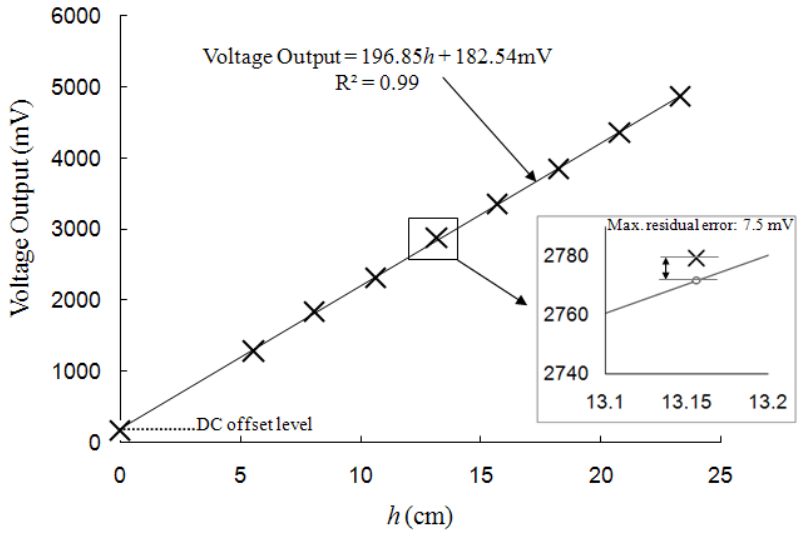

Figure 4. Voltage output of the transducer with respect to the static load in terms of water column (h) above the transducers' sensing element, data shown with cross symbols for transducer #2. Insets: Equation on top represents the best fit line; figure on the lower right corner is a magnification of the data point with maximum residual error (empty circle in this figure represents the predicted value by the best fit line equation); vertical line on lower left corner shows the DC offset voltage level for this transducer.

A change in the stagnation pressure of 3.72 N/m^2 corresponds to a 4% increase in the incident flow velocity. Experiments with various size spherical mobile particles indicated that the flow velocity, measured one particle upstream of the grain may increase more than 100% at the instants just prior to particle movement (Balakrishnan 1997). In addition, the vertical pressure difference that is necessary to overcome the submerged weight, W_s, of a 12.7 mm diameter Teflon® grain is 108 N/m^2 (the critical pressure, from here on denoted by p_{crit}). Given these facts, the smallest change in pressure that can be

measured with the transducers (3.72 N/m^2) is sufficient to capture pressure changes due to turbulence which have the potential to dislodge a 12.7 mm diameter Teflon® grain.

2.3 Dynamic Performance Test

We employed various brass tubing arrangements in our pressure measurement set-up to connect the pressure taps and transducers as shown in Figs. 2(*a*), 2(*b*) and 2(*d*). Therefore, a dynamic performance test was necessary to evaluate the distortion, if any, in the pressure signal due to length of the tubes and bends. According to Yoshida *et al*. (2001) the effect of bends in a tubing line on the pressure signal is negligible if the effective cross sectional area of the tube at the bend zone is more than 50% of original area of the straight tube. To avoid excessive crimping of the brass tubing we used a commercial tube bender. Although the length of tubing used between the pressure taps and the transducer sensing elements (one per sensor) varied slightly between taps, the overall length of the tubing did not exceed 10 cm.

A dynamic performance set-up similar to that reported by Yoshida *et al*. (2001) was used to test our transducers and the tubing system. The Plexiglas static calibration box was modified and utilized for the dynamic performance tests (Fig. 3). This time we used a 25.4 cm diameter subwoofer and an amplifier to generate a fluctuating pressure field in the sealed box. The input to the subwoofer was white noise, generated by the MATLAB software (The MathWorks Inc.). The fixture was placed in the calibration box with a water level of 3.8 cm. To isolate the transducers from the vibrating Plexiglas box and test bench, the transducers were mounted on a separate supporting structure (see Fig. 3) that was fixed to the lab floor without any connection to the calibration test platform.

Flexible Teflon® tubing was used to securely attach the transducers to the brass tubes as shown in Fig. 3 to further reduce any vibration effects. The same arrangement was also used in the flume tests.

The top pressure tap (p_3) and corresponding transducer was used as the control for comparing the performance of the others. The bottom pressure tap (p_4) and connecting tubing was judged to be most susceptible to frequency distortion due to the necessary tight bend radius of the tubing designed within the instrumented fixture (Fig. 2(*a*)) and the length of the tubing. Since it was not possible to introduce a calibrated input pressure signal to the testing box, the signal from p_3 was used as the input (undistorted signal) and p_4 was treated as the output. The goal here with the dynamic performance tests was not to determine the frequency response of the transducers but rather to quantify the influence of tubing built within the instrumented fixture on the measured pressure signals. That is, the calibration data provided by the manufacturer (indicating a flat frequency response up to 300 Hz) was used for all four transducers.

Nezu & Nakagawa (1993) suggest that the maximum response frequency, f_{max}, for turbulence measurements in channel flow should be higher than $(50/\pi)(U/h)$ in order to resolve flow structures down to viscous sub-range. Here, U is the depth average velocity and h is the flow depth (see Table 1 for U and h values for the flume tests). For the flow conditions used in our tests, the frequency up to which a flat response is required was obtained using Nezu's assumption and found to be varying between 62-95 Hz. Approximate length scales of the flow structures that can be detected at such sampling frequencies are larger than those between 4.7 - 5.7 mm ($\approx U/f_{max}$). Given that the test particle diameter is 12.7 mm and the forces induced by flow structures smaller than the

particle size are not significant (Schmeeckle *et al*. 2007), these length scales are enough to estimate the important force fluctuations.

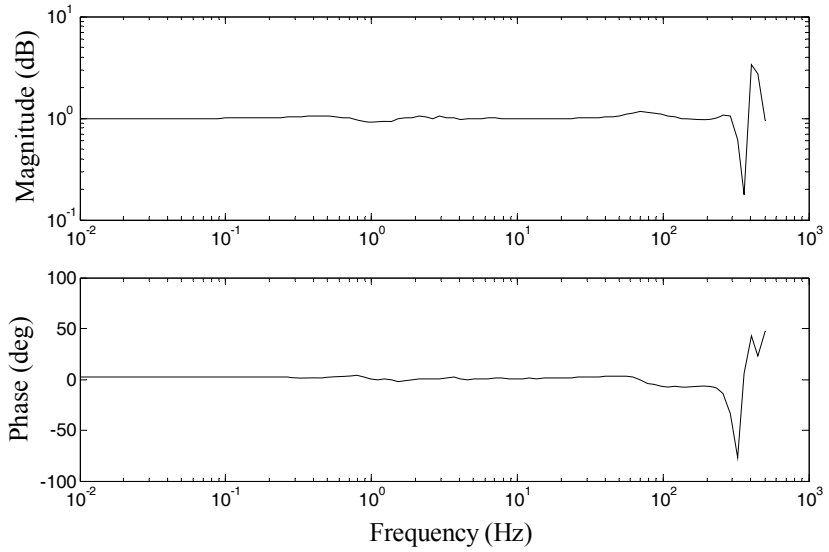

Figure 5. Magnitude and phase plots of transfer function between the pressure signals p_3 (top) and p_4 (bottom).

In order to determine the limitations in the pressure measurements due to tube bends, and the actual value of the maximum response frequency of the tubing system, the dynamic performance tests were performed using the test rig shown in Fig. 3. We used a sampling frequency of 1000 Hz and a sampling duration of 2 min in these tests. Subsequently, the transfer function between the two pressure signals measured at the top and bottom of the grain was estimated and the amplitude and phase plots (Bode plot) between the two signals are given in Fig. 5. It is indicated that the tubing effect is negligible up to at least 100 Hz, which satisfies Nezu & Nakagawa's (1993) criterion.

2.4 Measurement Uncertainty in the Flume Tests

Prior to the flume tests, a separate investigation was carried out to detect the natural frequency of the flume being used as well as the effect of flume pump operation on the pressure signals. Two Endevco, Isotron Model 50, single axis accelerometers (with 2-4000 Hz frequency range, and a sensitivity of 50 mV/*g*, where *g* is the acceleration due to gravity) were attached to the flume walls, one near the test section where the instrumented fixture was located, and the other, 2 m upstream of the test section. The vibration levels in both spanwise and vertical directions were recorded by changing the orientation of the accelerometers for a variety of flume operating conditions. The results from this investigation indicate that the flume has a natural frequency of around 100 Hz (when there is no pump and flow activity). A second research flume located at the same room was found to have a similar natural frequency which might be an indication of a structural natural frequency.

The effect of the flume vibration due to the pump and the flow on the pressure signals was also investigated and found to be negligible as long as the transducers were fixed firmly but separate from the flume structure. This was confirmed by comparing simultaneous DC voltage readings (while the flume was running) from a pressure transducer which was attached to a fixture separate from the flume to that of another transducer which was attached to the flume wall.

2.5 Summary of Experiments

Experiments were performed using the bed configuration shown in Fig. 2 under (*i*) uniform flow conditions and (*ii*) in the wake of a cylinder located upstream of the

particle. The sampling frequency and the duration for each run were 250 Hz and 15 min respectively.

The following experimental procedure was repeated for each flow condition, after allowing the flume to run for an extented length of time prior to any measurements to establish stable conditions. First, the local flow velocity near the bed and the pressure signals were recorded simultaneously for 15 minutes. At the completion of the run, velocity profile measurements were performed using LDV one diameter upstream of the test particle. These profiles were then used to obtain the friction velocity, u_* using the Clauser method (Song *et al*. 1994).

Individual pressure signals were checked for drift after each run. The drift was found to be negligible in all cases. Based on the results from the investigations of measurement uncertainties presented earlier, all the pressure data from flume tests were first digitally filtered with a 9^{th} order, Butterworth low-pass filter with a cut-off frequency of 90 Hz. This cut-off frequency is also below the structural natural frequency of around 100 Hz reported earlier.

The unevenly sampled LDV signal was linearly interpolated and re-sampled at 250 Hz to obtain pairs of synchronized pressure and velocity signals. Statistics of the (original) unevenly sampled and re-sampled velocity signals were compared and the influence of re-sampling on the velocity data statistics was found to be insignificant.

Experiments under Uniform Flow Conditions

We conducted flume experiments under nine different uniform flow conditions. Table 1 gives a summary of the flow conditions tested. Presented parameters are U, h, particle

Reynolds number, $Re^* = u^*d/v$, where v is the kinematic viscosity of water. These experiments matched the threshold conditions used in earlier tests by Celik et al. (2010) for a Teflon® ball at different levels of particle entrainment frequency. The turbulence intensity (TI) given by $u'_{rms}/\overline{u}$ was measured to be near 0.27 for all uniform flow experiments; where u'_{rms} is the root-mean-square of the turbulent velocity fluctuations, u', and $\overline{u}$ is the time average value of u measured near the instrumented grain via the LDV system (over bar denotes time average of a parameter over the entire sampling duration).

Table 1. Summary of the flow conditions. Note that the last row presents the undisturbed flow condition parameters for cylinder tests (UC) without the cylinder.

Run	Depth average velocity, U (m/s)	Flow depth, h (cm)	Re^*
A1	0.47	8.1	438
A2	0.45	7.5	424
A3	0.43	8.2	413
A4	0.41	7.9	398
A5	0.42	8.3	385
A6	0.40	8.6	377
A7	0.41	9.1	372
A8	0.39	8.7	364
A9	0.35	8.9	330
UC	0.42	9.1	399

Experiments in the Wake of a Cylinder

Bluff body wake flows are of interest to many branches of physics and engineering and have been studied extensively (see Williamson 1996 for a detailed review). The wake flow downstream of the bluff body is characterized by higher turbulence intensities and larger pressure fluctuations acting on the wall. In many practical river engineering applications, flow is altered due to presence of hydraulic structures. These conditions lead to a significant increase in sediment movement and result in scour near these hydraulic

structures in rivers and waterways (Sumer *et al*. 2003, Radspinner *et al*. 2010). Flow around and past pipelines, bridge piers and other in-stream structures are some of the examples. The purpose of the tests considered here was to examine if, and more precisely the way in which, the presence of a cylinder might influence the fluctuations of pressures acting on the instrumented grain in such unsteady wake flows.

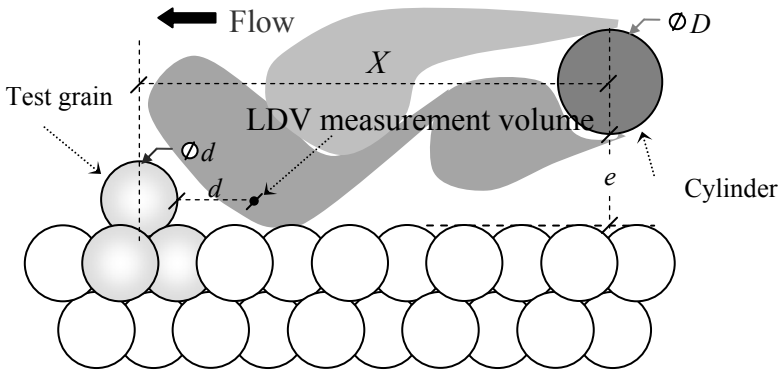

Figure 6. Side view of the test section with the test particle in the wake of a cylinder.

The cylinder was placed horizontally and in a direction perpendicular to the flow, extending across the entire flume width upstream of the test section. Four different size PVC pipes with diameters, D, of 33.4, 26.7, 21.9 and 12.7 mm were used. Figure 6 shows the bed conditions with the cylinder. X and e in Fig. 6 are the distance between the center of the instrumented test grain and centerline of the cylinder in the streamwise direction, and the distance between the bed (top of the spheres in the uppermost layer) and the cylinder respectively. e was set equal to D, for all four cylinder diameters to avoid suppression of the vortex shedding due to rough bed proximity (Sumer & Fredsøe 2006). X was chosen to be $2.5D+1.5d$ as this location was where the highest turbulence intensity (obtained from near-bed velocity measurements) was observed in preliminary flume tests. The presence of the cylinder in the flow increased the turbulence intensity at a location

one diameter upstream of the instrumented particle (LDV measurement point shown in Fig. 6) by 35%, 51%, 57% and 14% for D values of 33.4, 26.7, 21.9 and 12.7 mm respectively, compared to undisturbed flow condition tests (UC). The last row in Table 1 summarizes the undisturbed flow conditions under which the cylinder tests were performed.

3. Characteristics of the Surface Pressures Acting on the Grain

3.1 Uniform Flow Conditions

Detailed results on the statistics of the pressure fluctuations and the connection between the individual pressures are presented in this section. The histograms of individual pressures, $p_{1\text{-}4}$, from run A2 are given in Fig. 7. The statistical distributions of all four pressure signals were skewed. p_1 was positively skewed with skewness values varying between 0.74 and 0.83 for all runs performed under uniform flow conditions (A1-A9 and UC). This is in conformity with the findings of Hofland & Battjes (2006). The other three pressure signals were negatively skewed with skewness values consistently near -0.39, -0.36 and -0.33 for p_2, p_3 and p_4 respectively. Kurtosis values for the pressure signals p_2 and p_3 were near 3.1 which is close to the expected value for a normal distribution, while it was 3.7 and 3.8 for p_1 and p_4 showing a deviation from normal distribution due to moderate tails for these two pressure signals. Maximum pressure variations (i.e. p'_{max} and p'_{min}, where the prime denotes the fluctuating component obtained by Reynolds decomposition) were observed to be 4.5 and 6.8 times the root-mean-square (rms) of fluctuations, p'_{rms} for p_1 and p_4 respectively. These findings imply that both p_1 and p_4 include in their tail region extreme values which can play a role in particle dislodgement.

The variations in pressure values at the location of the 4th pressure tap have often been ignored in sediment transport studies (see for example Hofland *et al*. 2005 and Detert *et al*. 2010(*a*)). Nevertheless, very low p_4 values, also depending on the instantaneous value of p_3, can occasionally lead to high downward lift forces and aid in particle stability. Otherwise, higher p_4 values which are occurring more frequently could be contributing to particle dislodgement.

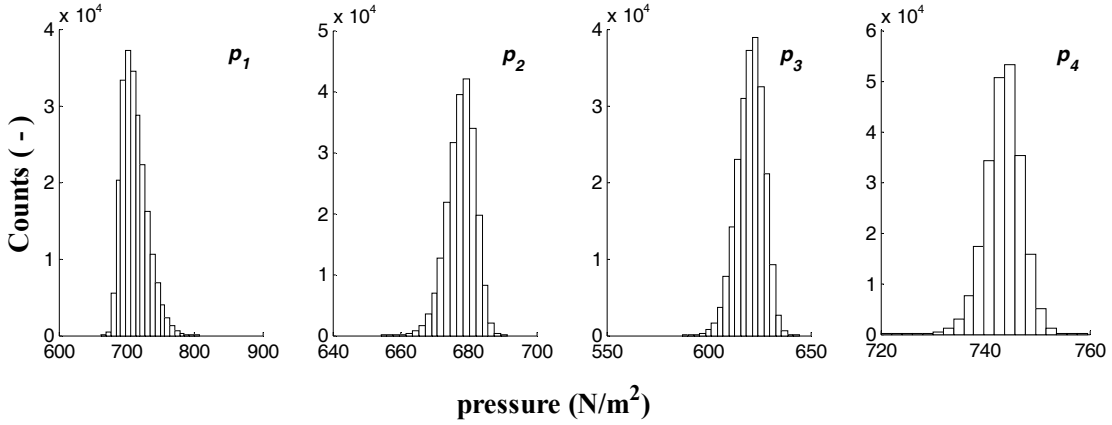

Figure 7. Pressure histograms from run A2; 225,000 data points are represented in each histogram.

The magnitude of the fluctuations in p_2, p_3 and p_4 are very low compared to p_1. Among the former three, p_3 (top) fluctuates widely relative to p_2 (back) and p_4 (bottom) for both the uniform and cylinder wake flows. p'_{rms}, of p_1 was consistently larger than those of p_2, p_3, and p_4 by factors of 4, 3 and 5 respectively for the uniform flow conditions tested. The ratio of root-mean-square (rms) of pressure fluctuations, over the bed shear stress, τ_0, with respect to particle Reynolds number is given in Fig. 8 for the 9 uniform flow conditions (see Table 1). Shear stress values were calculated using ρu_*^2,

where ρ is the density of water. An average value of 3 for p'_{rms}/τ_0 is reported in the literature for rough walls (Smart & Habersack 2007 and Vollmer & Kleinhans 2007 provide reviews on this topic). In our experiments, we obtained values close to 3 only for p_2 and p_4 (back and bottom pressures respectively). For p_1 and p_3 this ratio was near 18 and 7 respectively. p_1 and p_3 therefore are expected to make the major contributions to the fluctuations of pressure forces acting on the grain. The very high values of p'_{rms}/τ_0 for p_1 and p_3 also indicate the inadequacy of the approaches based on shear stress in describing the flow induced pressures and forces acting on fully exposed bed material. Furthermore, they highlight the need to account for the continuous record of the fluctuating pressures in particle movement.

3.2 Cylinder Tests

Data from the cylinder tests revealed that the time average values of the pressures for all cylinder diameters remain the same to that of the undisturbed flow conditions (UC). p'_{rms} values of all four pressures increased in the presence of the cylinders by a factor of 2 for all cylinder diameters tested. Nelson *et al*. (1995) and Sumer *et al*. (2003) reported a significant increase in bedload transport under such conditions where the turbulence intensity near the bed was higher compared to the uniform flow conditions. We will address the role of turbulence intensity on the pressure and force fluctuations later in section 6. An overlooked aspect of the surface pressures acting on the grains in sediment research, the correlations between the individual pressures are presented in the following section.

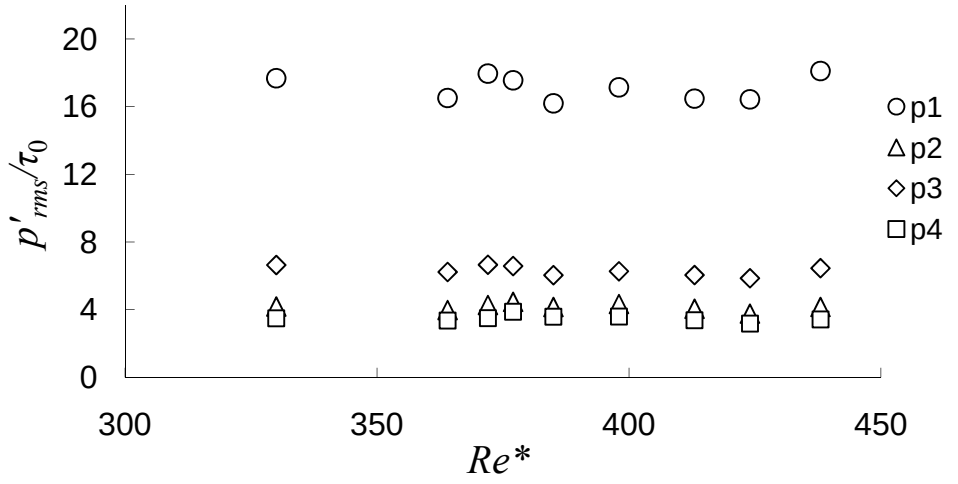

Figure 8. p'_{rms}/τ_0 vs. Re^* plots from uniform flow conditions (A1-A9).

4. Correlations between the Individual Pressures

4.1 Uniform Flow Conditions

Cross correlation functions (CCF) were used to investigate the statistical similarities between two pressure time series as well as to detect the time lag between them. The correlation coefficient at time lag Δt, $R_{ab}(\Delta t)$ between any two variables, a and b is given by:

$$R_{ab}(\Delta t) = \frac{\sum [a(t) - \bar{a}][b(t + \Delta t) - \bar{b}]}{(N-1)\sqrt{\sum [a(t) - \bar{a}]^2}\sqrt{\sum [b(t + \Delta t) - \bar{b}]^2}} \quad (1)$$

where N is the number of pairs of data (a, b). A positive Δt in Eq.1 implies that b values were measured at time Δt later than that of a. Figures 9(*a-f*) show the CCF's between individual pressures as a function of time lag. As the data from runs of uniform flow conditions (A1-A9 and UC) exhibit similar behaviors, we present plots of CCFs between pressures from run A2 only.

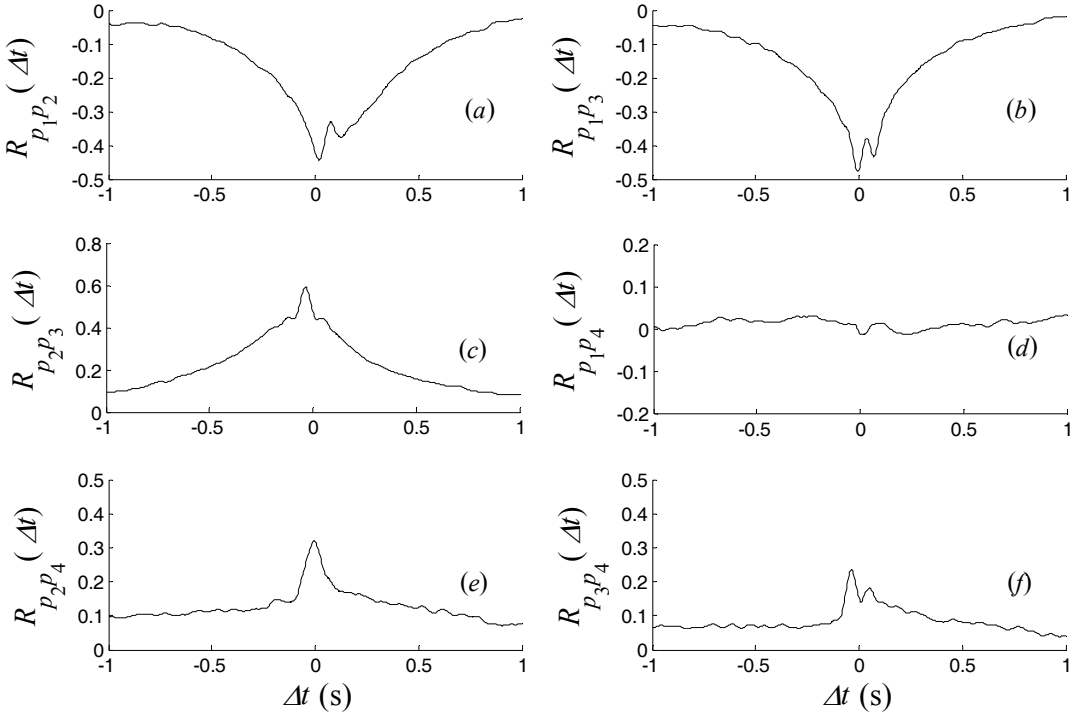

Figure 9. Cross correlation functions between: (*a*) p_1 and p_2, (*b*) p_1 and p_3, (*c*) p_2 and p_3 (*d*) p_1 and p_4 (*e*), p_2 and p_4, and (*f*) p_3 and p_4, all from run A2.

The pressures p_1, p_2 and p_3 are well correlated with each other (Figs. 9(*a*), 9(*b*) and 9(*c*)). In particular, a very significant correlation (~ 0.6) is obtained between the pressures on the top and back of the grain (Fig. 9(*c*)). This suggests that the flow processes causing high pressure fluctuations on top of the particle, via a Bernoulli effect for example, are also responsible for similar pressure fluctuations at the rear of the sphere, at a slightly later instant (negative time lag). Negative correlations shown in Figs. 9(*a*) and 9(*b*) are indicative of cases where an increase in p_1, stagnation pressure, in the front (with increase in velocity fluctuation) is observed, followed by a decrease in the pressures on the top and back of the grain (again at a slightly later time, consistent with the average

convection speed). This phenomenon is captured better in Fig. 10 where a surface plot of the instantaneous p_1, p_2 and p_3 obtained in run A2 is shown. In this plot, the distinct regions of "high p_1 - low p_2 and p_3"and "low p_1 - high p_2 and p_3 are clearly seen at the lower right and upper left corners respectively. Such combinations, when p_1 is high while p_2 and p_3 are low, provide favorable overall instantaneous resultant force for particle dislodgement. It should be noted that the frequency of occurrence of these events is not indicated in this figure.

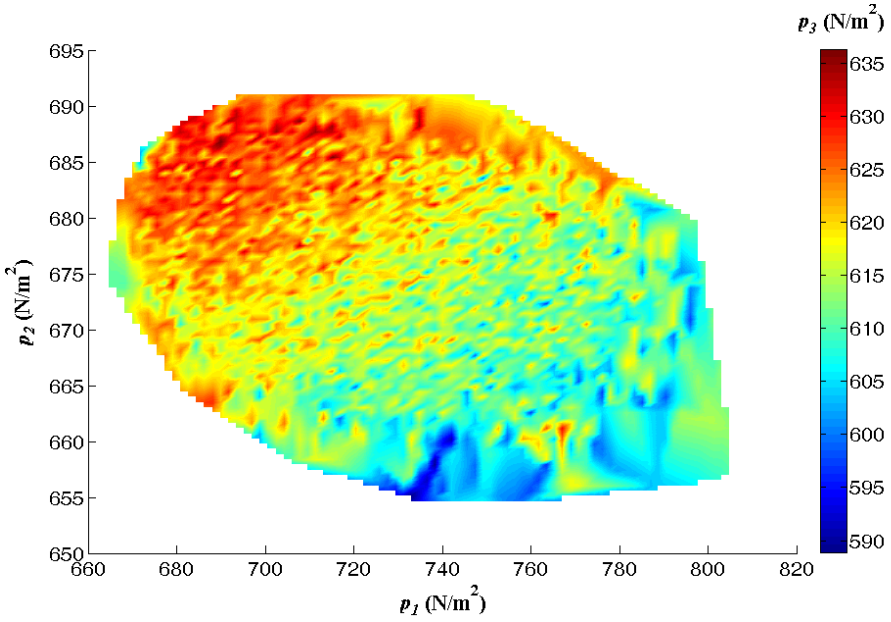

Figure 10. A (3D) surface plot of the instantaneous p_1, p_2 and p_3 from run A2. Color bar represents the magnitude of p_3. 225000x3 data points (p_1, p_2 and p_3) were used to create this plot.

Curiously, Figs. 9(*e*) and 9(*f*) show that p_2 and p_3 which are highly correlated with p_1 are also correlated with p_4, although these correlations are not as strong as those shown in Figs. 9(*a*) and 9(*b*). On the other hand, there is little or no correlation between p_1 and

p_4 (Fig. 9(*d*)). Smart & Habersack (2007) reported comparable findings between the pressures measured on top of a roughness element and within the natural gravel pore directly below. A possible explanation for this phenomenon is that the fluctuations of p_1 are dependent upon the structures of near-bed turbulent flow and the characteristic signature of these flow structures is not maintained in the pore flow underneath the particle where p_4 is measured.

Another observation is that the CCFs involving the pressure behind or on top of the grain exhibit two dominant peaks (i.e. Figs. 9(*a*), 9(*b*) and 9(*f*)). The time lag between the peaks is on the order of 100 ms. Using Taylor's hypothesis, this duration, together with the time average near-bed velocity, gives a length scale about twice the particle diameter. These length and time scales are too small to be linked to the largest eddies in the channel which are several times the flow depth in size in the streamwise direction (Shvidchenko & Pender 2001). The time lag between the peaks is also large to be compared with higher frequency particle-scale or smaller flow structures generated via vortex shedding by the roughness elements upstream of the grain or by the grain itself. The latter view point is in agreement with the findings of Schmeeckle *et al*. (2007). They argued that the particle-scale structures generated by the vortex shedding by the upstream grains or the test grain itself do not influence the instantaneous forces acting on it.

4.2 Cylinder Tests

The double peaks in CCFs of signals from the cylinder wake experiments are not so easily identified because the effect of oscillations in the CCFs (due to vortex shedding from the cylinder) dominates. However, the distance between the oscillating peaks is

clearly indicative of the size of the flow structures. That is, Fig. 11 shows the CCF's between individual pressures as a function of time lag resulting from cylinder tests with D = 33.4 mm. Oscillations shown in Fig. 11 yield a period of about 2/12=0.166 ms (a frequency of nearly 6Hz). Figure 12 shows that the power spectral density, PSD, of p_1 from the same run exhibits a dominant peak at 2 Hz and also another peak near 6Hz. The latter matches the frequency obtained from the cross correlation function while the peak at 2 Hz is consistent with vortex shedding from the cylinder (i.e. Strouhal number = 0.21, St = fD/V, where f is the vortex shedding frequency, 2 Hz, V is the time average flow velocity upstream of the cylinder's centerline, V = 0.31 m/s, measured with the LDV system). The two dominant frequencies are attributed to the variations in the rapidty of the vortex shed from the lower side of the cylinder and that of upper side which results from vortex-boundary layer interactions (Sarkar and Sarkar 2010). The time lag between the peaks which corresponds to 6 Hz frequency shown in Fig. 11 indicates the period of energetic vortical structures downstream of the cylinder and when used together with the time average streamwise velocity, $\bar{u}$, measured near the bed (~0.25 m/s, considered as convection velocity) suggest a length scale of 41 mm which is comparable to the cylinder diameter used in this run.

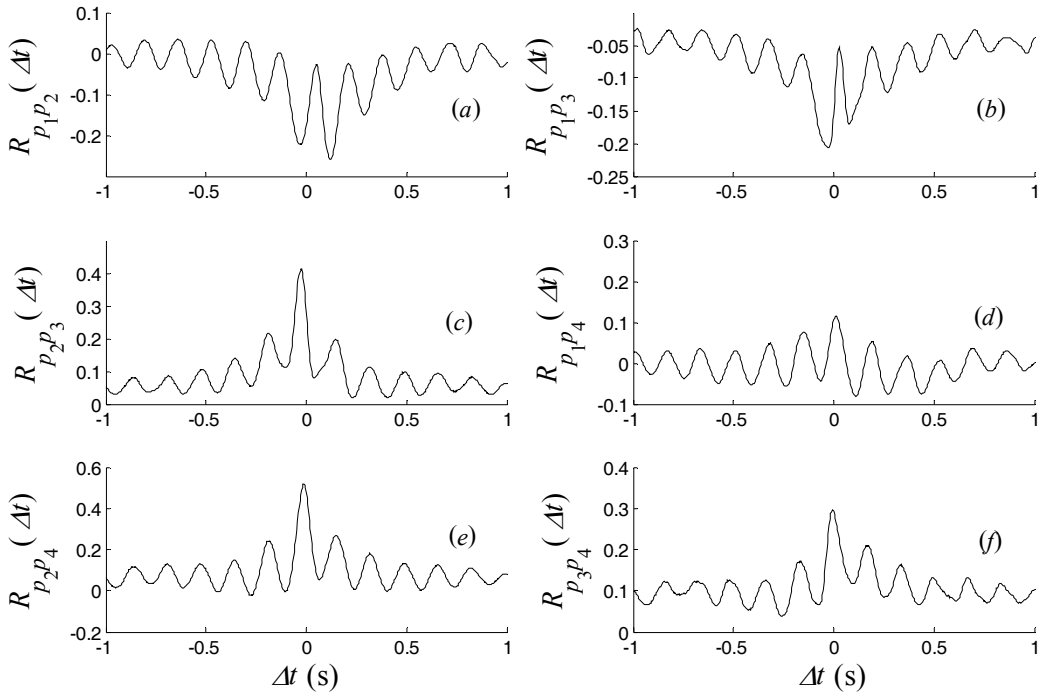

Figure 11. Cross correlation functions between: a) p_1 and p_2, b) p_1 and p_3, c) p_2 and p_3 d) p_1 and p_4 e) p_2 and p_4, f) p_3 and p_4, all from run with the cylinder D = 33.4 mm. The dominant periodic structure corresponds to 6 Hz for this cylinder size.

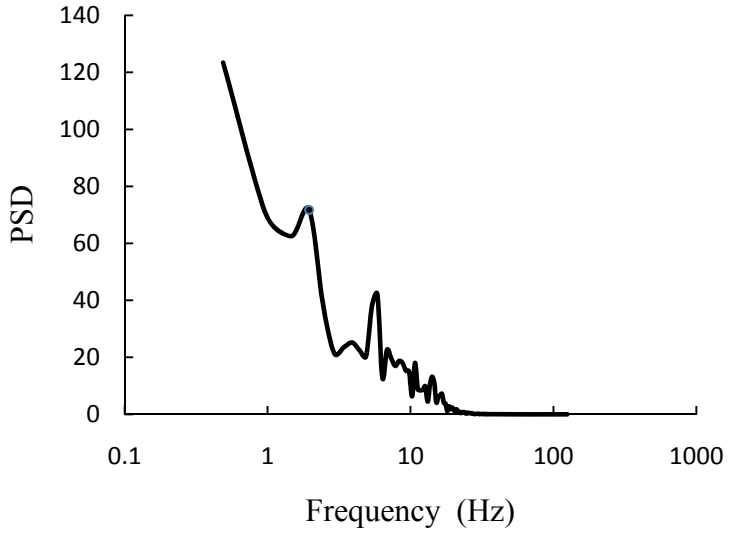

Figure 12. Power spectral density vs frequency of p_1 signal from cylinder tests (D = 33.4 mm).

5. Pressures and Near-bed Flow Velocity

We first illustrate the qualitative relation between the velocity and pressure signals by showing the representative time histories of u, w and the simultaneously measured pressures from run A2 in Fig. 13 and from the cylinder test with D = 33.4 mm in Fig. 14. A strong similarity in the temporal variations between u and p_1 is observed in both Figs. 13 and 14. This is expected as p_1 is located at the stagnation point, and so anticipated to be closely related to u^2. In Fig. 13, a negative correlation is apparent between p_1 (as well as u, as will be shown later) and the other three pressure signals. The time lag associated with this negative correlation is on the order of h/U (~200 ms, estimated from cross-correlation function between u and p_1). This negative correlation is however not evident in the cylinder tests (Fig. 14).

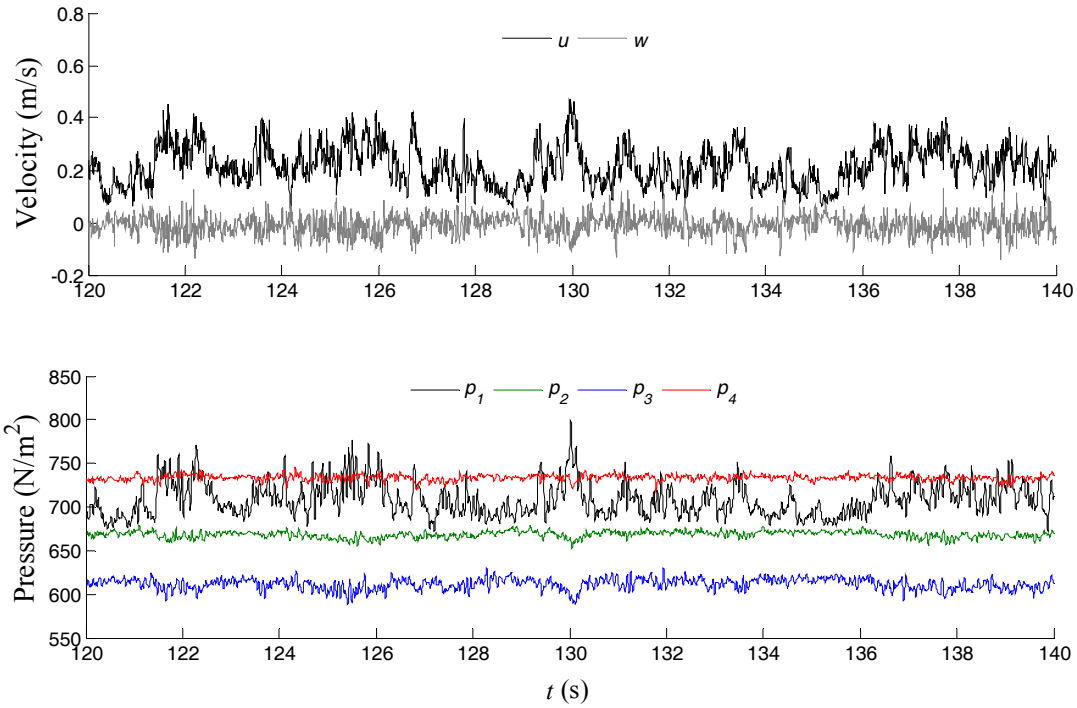

Figure 13. Representative time series of, u, w (top) and simultaneously measured surface pressures (bottom) from run A2.

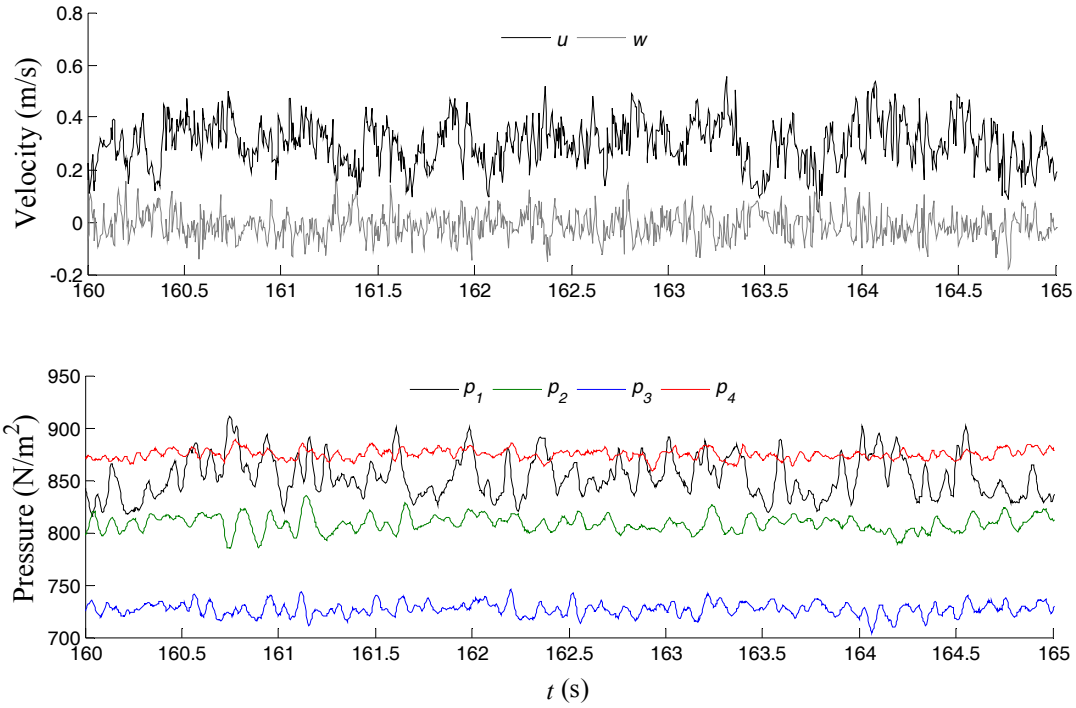

Figure 14. Representative time series of, u, w (top) and simultaneously measured surface pressures (bottom) from a cylinder test (D = 33.4 mm).

5.1 Uniform Flow Conditions

Figure 15 presents the CCFs between u and the pressure signals for uniform flow conditions. The CCFs between w and the pressures for uniform flow conditions are shown in Fig. 16. According to the CCFs with respect to time lags shown in Fig. 15, p_2 and p_3 are inversely correlated with u while, as expected, p_1 has a strong positive correlation with u. This finding is consistent with the negative correlation between p_1 and p_2 as well as p_1 and p_3 presented earlier (Fig. 9).

Figure 16 reveals a strong negative correlation between w and p_1. p_2 is also dependent, albeit weakly compared to p_1, on the vertical velocity (positive correlation).This indicates that, noting the positive correlation between u and p_1, during a

sweep like event ($u' > 0$, $w' < 0$) when w is towards the bed and u is high, p_1 also has high values. This is accompanied with a decrease in p_2. When u is low and w is positive (ejection like event with $u' < 0$, $w' > 0$) there is a decrease in p_1 and an increase in p_2. This observation is in agreement with the findings of Hofland *et al*. (2005) that the fluctuating drag force ($\propto (p_1 - p_2)$, see Fig. 2(*a*)) is also a function of the vertical velocity component. As shown in Fig. 16, p_3 is also correlated with w (positive correlation). This represents a favorable situation for particle dislodgement, during sweep like events for example, which are causing an increase in p_1, and having the opposite effect on p_2 and p_3, the former increasing the drag and latter contributing to upward lift forces acting on the grain. In another possible flow event, where a slow fluid parcel is ejected from the bed, p_1 will have lower values and p_2 and p_3 will increase, altogether having a stabilizing effect on the grain. p_4, on the other hand, was found to be uncorrelated with u and w, in agreement with the findings of Fig. 9(*d*).

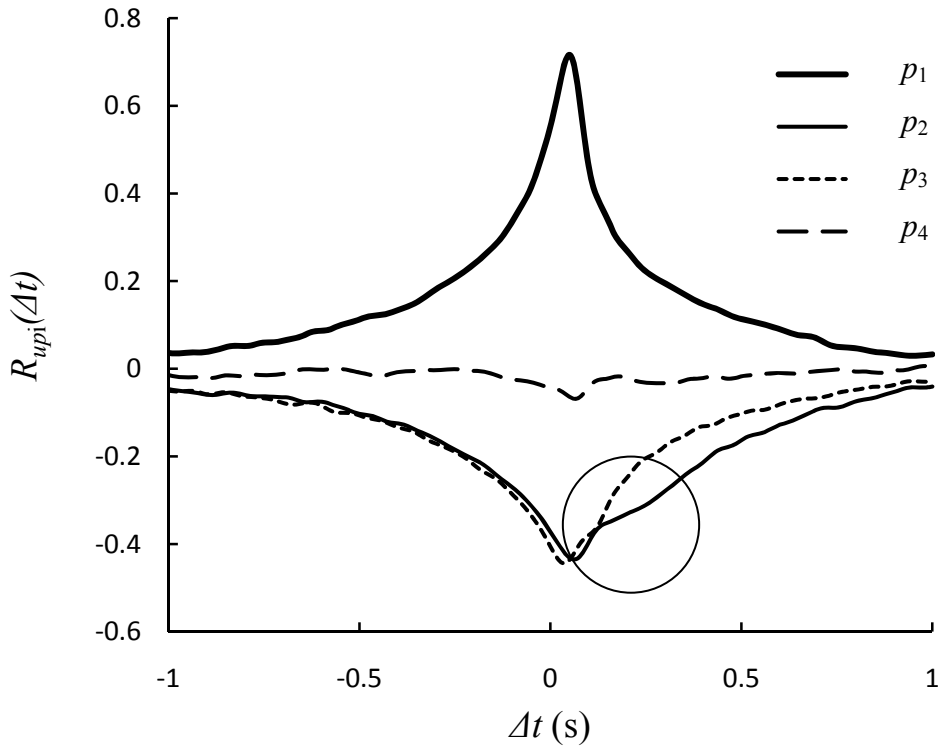

Figure 15. CCFs between u and the pressures from run A2. The circle shows the second peaks in the CCFs.

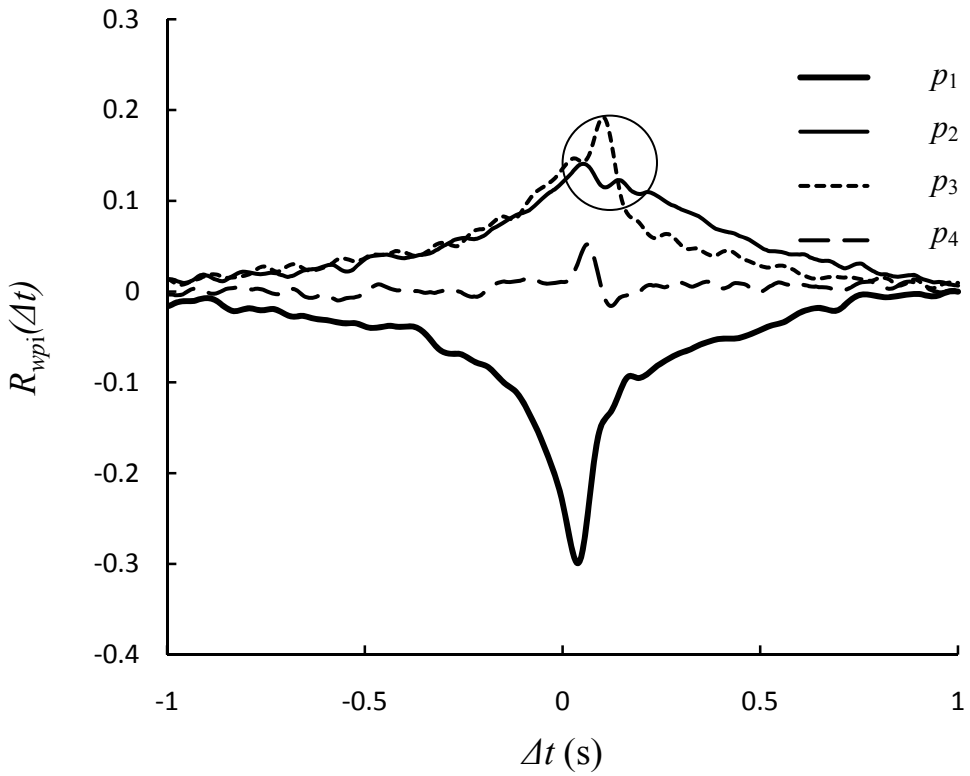

Figure 16. CCFs between *w* and the pressures from run A2. The circle shows the double peaks in CCFs.

The CCFs between the flow velocity and pressures for uniform flow conditions (run A2) given in Figs. 15 and 16 reveal again the double peaks (shown with circles). The second peaks are clearly seen especially in Fig. 16 in the CCFs between "*w* and p_2" and "*w* and p_3".

5.2 Cylinder Tests

The CCFs between the flow velocity and pressures for flow in the wake of a cylinder (D = 33.4 mm) are shown in Figs. 17 and 18 for *u* and *w* respectively. It is seen that p_1 is out of phase with $p_{2\text{-}4}$ by a time lag of 15 ms. p_2 and p_3 appear to be out of phase with each other as well, although it should be noted that these are inferred from the influence of the

same controlled effect, the cylinder wake, on the pressure signals. The phase delay between the pressures and the flow velocity will be elaborated in the next section with emphasis given to the instantaneous positive peaks in p_1 signal.

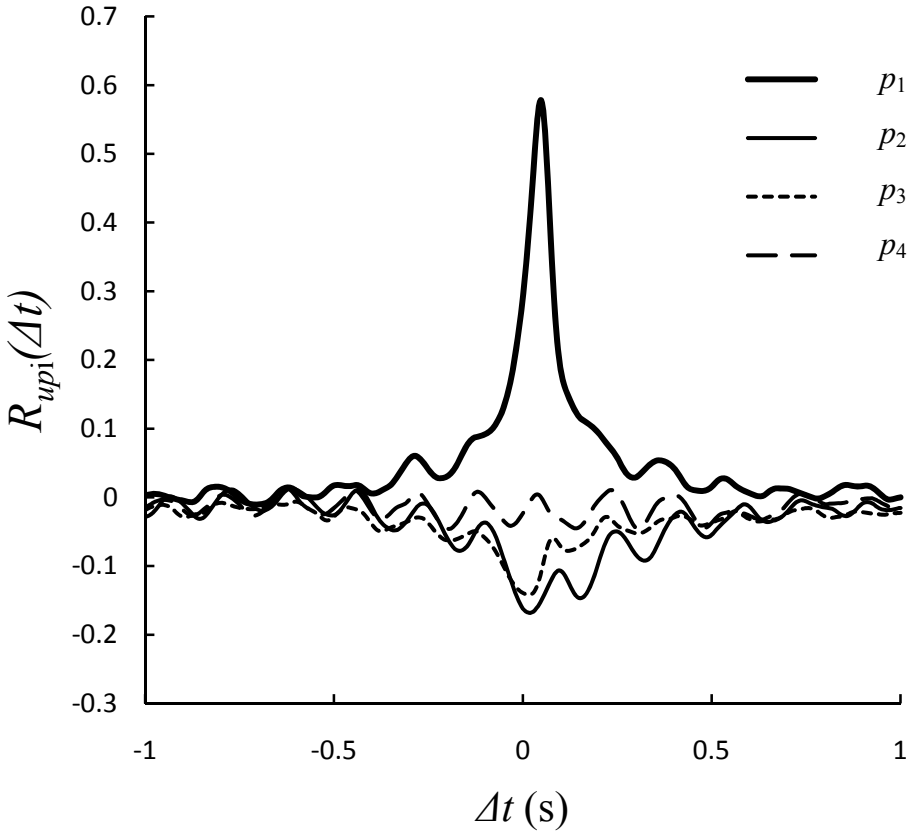

Figure 17. CCFs between u and the pressures from the cylinder test with D = 33.4 mm.

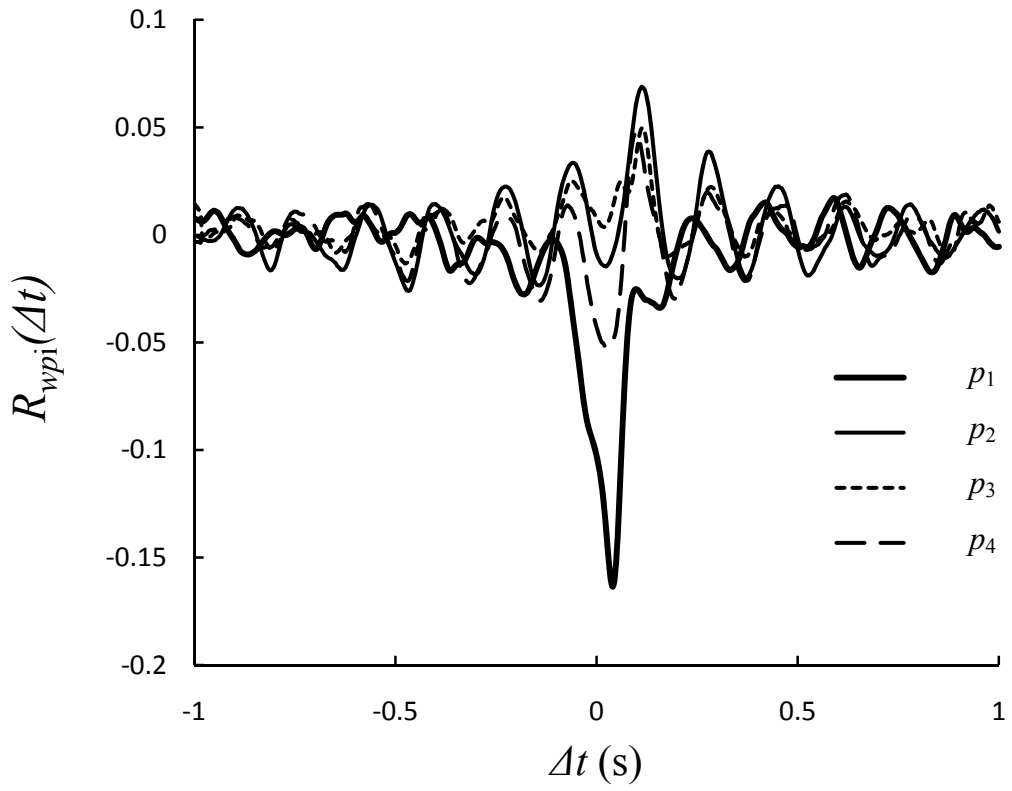

Figure 18. CCFs between w and the pressures from the cylinder test with D = 33.4 mm.

6. Conditionally Sampled Pressure Fluctuations

Conditional sampling of pressure has often been utilized to characterize peak pressure events acting on rough and smooth walls and their relation to the near-bed flow structures (Johansson *et al*. 1987, Laadhari *et al*. 1994; Detert *et al*. 2010*b*). For this purpose, we employed a peak detection method which is based on the p_1 signal. This is justified because the peak events in p_1 are more relevant to particle entrainment for the fully exposed particle configuration studied here (Drake *et al*. 1988, Diplas *et al*. 2008). Local peaks in the pressure signal with positive fluctuations higher than H times the root-mean-square of the pressure fluctuations (i.e. $p' > H.\, p'_{rms}$) were detected, where H is a threshold value. Prior studies concerned with wall pressure fluctuations employed H

values often between 2 and 4 (Laadhari *et al*. 1994). In this study, results for $H = 1$ and 2 will be presented as these values were found to provide a general impression about the magnitude of low frequency peak events while allowing for inclusion of a reasonable portion of the p_1 signal in the analysis. Prior to the analysis, the pressure data was low pass filtered (9th order Butterworth) at 125 Hz (half of the Nyquist frequency) in order to smooth the shape of the peaks and reveal the underlying temporal variations. The magnitude of the positive pressure peaks in the filtered p_1 signal, with $p' > H\,p'_{rms}$, together with their time of occurrence were detected using the Matlab software. Figure 19 illustrates the detected peaks in p_1 using the data from A2. Table 2 summarizes the results from the peak detection analysis.

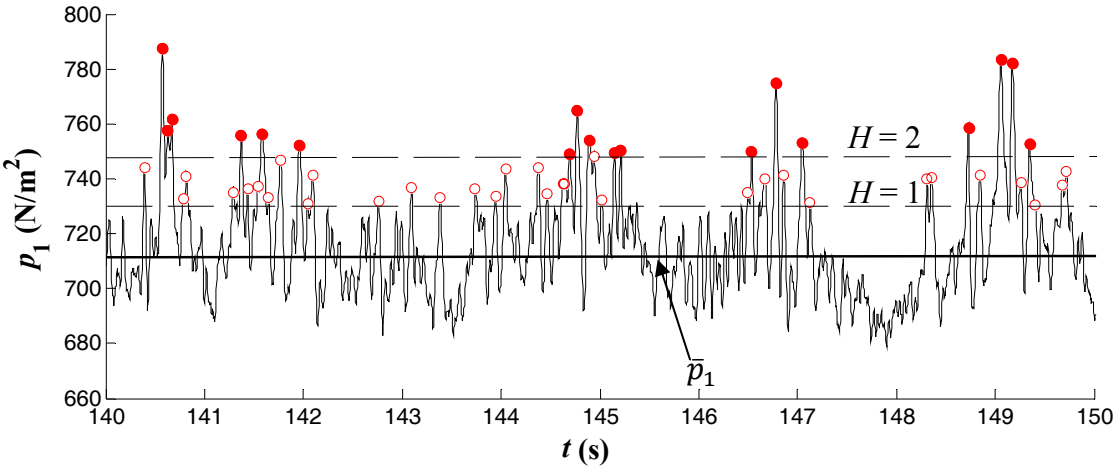

Figure 19. Representative time series of (filtered) p_1 from run A2. The detected local peaks with $p' > p'_{rms}$ and $p' > 2p'_{rms}$ are shown with empty and solid circles respectively. The threshold levels (for $H = 1$ and 2) are shown with horizontal, dashed lines. Time average p_1 is specified with horizontal, solid line.

Table 2. Summary of the results from peak detection analysis (for p_1). Turbulence intensity, TI, for uniform flow experiments was 0.27. The last four rows present the tests with the cylinders.

			$H = 1$		$H = 2$	
		Run	# of peaks per s	Ensemble average peak magnitude (N/m^2)	# of peaks per s	Ensemble average peak magnitude (N/m^2)
		A1	4.0	784.17	1.4	801.14
		A2	4.0	747.29	1.4	759.73
		A3	4.1	830.05	1.4	844.39
		A4	3.8	803.14	1.3	816.60
		A5	3.9	849.82	1.3	862.17
		A6	4.0	874.17	1.3	886.77
		A7	3.8	879.87	1.3	892.05
		A8	3.7	887.50	1.3	898.43
		A9	3.7	827.75	1.3	837.61
TI	D (mm)	UC	4.2	883.61	1.4	891.48
0.37	33.4	D1	4.6	892.24	1.5	909.11
0.41	26.7	D2	3.6	862.79	1.3	879.69
0.43	21.9	D3	4.1	842.66	1.6	854.88
0.31	12.7	D4	4.7	847.28	1.7	858.35

For a given threshold value, the number of detected peaks didn't vary with the change in the flow strength for uniform flow condition cases. However, $H = 1$ consistently resulted in higher number of peak events per min by a factor of 3 compared to $H = 2$, while the same effect increased the ensemble average peak magnitudes by only 2% or less for p_1 signals from all uniform flow conditions. For the cylinder tests, a trend was not apparent between the pipe diameters or the turbulence intensities upstream of the instrumented fixture and the number of the detected peaks (see data in Table 2). The presence of the cylinder induced a slight increase in the average peak magnitudes for $D =$

33.4 mm and a small decrease for the other three pipe diameters. The magnitude of the detected peaks in p_1 signal showed a positively skewed distribution with a heavy tail. The skewness values were between 1.1 and 1.5 for all runs, including the cylinder tests, and for both H values. This is due to the strong dependence of the p_1 on the near-bed velocity squared. The distribution of the peak magnitudes were found to be well characterized by Johnson SB distribution (p-values ranging between 0.4 and 0.9). The probability density function (pdf) of the detected peaks for runs UC and D1 (with H =2) together with their normalized histogram are given in Figs. 20(a) and 20(b).

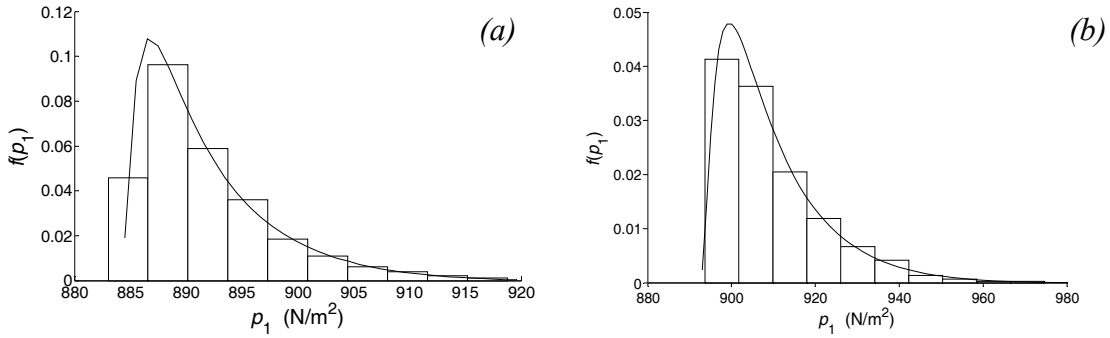

Figure 20. Pdf of the detected peak magnitudes in p_1 (H = 2). (a) data from UC. (b) data from cylinder test with D = 33.4 mm. Both normalized histograms and theoretical pdfs are presented. pdf: Johnson SB distribution, p-value: 0.52 for (a) and 0.65 for (b).

In order to examine the other pressure signals as well as near-bed flow velocity components associated with the peaks in p_1 signal, the following procedure was implemented. 200 ms long pressure ($p_{2\text{-}4}$) and velocity (u and w) waveforms were conditionally sampled by means of centering these 200 ms long windows on the instants of detected peaks in p_1 for each run (e.g. a window covering -100 ms before and 100 ms

after each positive p_1 peak). Subsequently, the ensemble average of these conditionally sampled waveforms was calculated (indicated by a superscript "+", e.g. p^+). The number of peaks per second, presented in Table 2, also represents the number of the conditionally sampled waveforms used here to obtain the ensemble average waveforms.

6.1 Uniform Flow Conditions

The representative patterns for the ensemble average pressures and the flow velocities (from run A2) are shown in Fig. 21. Individual pressure waveforms (corresponding to a single peak in p_1) were observed to be within ±15% of the p_{crit}. Although not shown here, all of the uniform flow data show similar patterns.

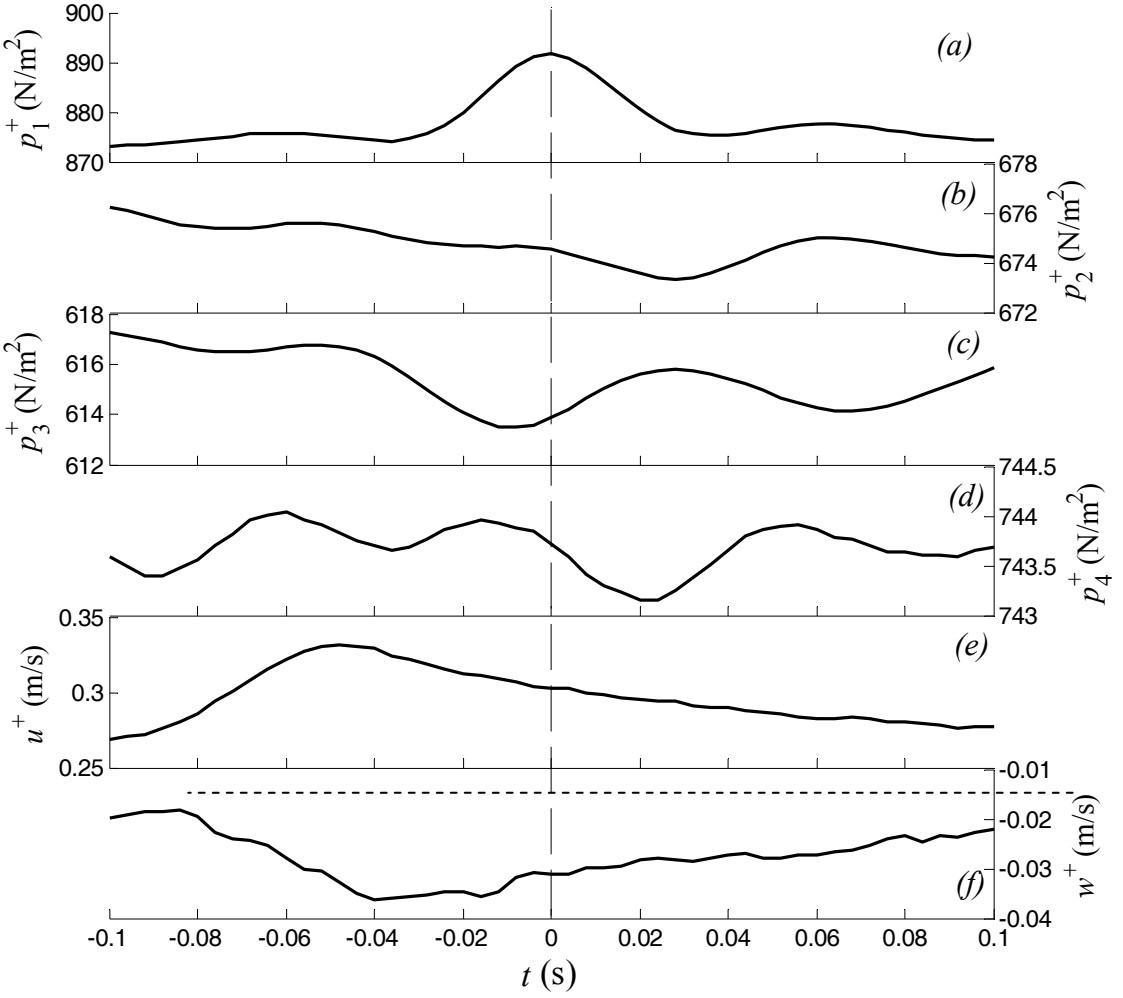

Figure 21. Ensemble averaged waveforms of conditionally sampled pressures ($p_{1\text{-}4}$) and velocities (u and w) from top to bottom (a)-(f), based on the detected positive peaks in p_1 signal. $t = 0$ is the instant when the peaks in p_1 were detected. Data from run UC was used and the ensemble average values are based on the 1296 detected peaks. Time average w is shown with dashed, horizontal line in (f). Threshold level, $H = 2$.

The duration of the pressure peaks in p_1 appears to be roughly 40 ms while the events in the flow velocities exhibit a longer duration, 3 to 4 times the pressure peak durations (Fig. 21(a)). This is in conflict with the quasi-steady theory which is based on

similar behaviors of pressures/forces and velocities at the same frequencies. The duration of peak events in the pressure signals will be discussed in detail in section 8.2.

Considering a 40 ms lifespan for the peak in p_1 (Fig. 21(*a*)) and the frequency of occurrence given in Table 2, the peak events which were detected using $H = 1$ and 2 occurred during approximately 16% and 6% of the total sampling time respectively. The latter is in accord with the estimations of Johansson *et al*. (1987) using an H value of 2.5. Therefore, the following sections will include results from the analysis only with $H = 2$.

The positive peaks of p^+_1 (front) coincide with accelerations in u^+ and decelerations in w^+ (Fig. 21). The ensemble average p^+_3 (top) waveform shows greater variability in its magnitude compared to p^+_2 (back) and p^+_4 (bottom). In addition, multiple positive and negative peaks in $p^+_{2\text{-}4}$ were observed consistently in all uniform flow cases. For instance, a negative peak occurred in p^+_3 before the positive peak in p^+_1 (Fig. 21(*c*)). Then the positive peak in p^+_1 was followed by negative peaks in both p^+_2 and p^+_4, and a positive peak in p^+_3. It was shown earlier in Fig. 9 that p_4 is not correlated with p_1 or flow velocity components. Figure 21 does not suggest a correlation between the waveform of p^+_4 with the other pressures or flow velocity components. Nevertheless these relatively low magnitude peaks in p_4 consistently occur during the peaks in p_1. These distinct features of the patterns shown in Fig. 21 suggest that the coupling of peaks in p_1 with events in other pressure signals is subtle. These patterns could be attributed to (*i*) the streamwise vortices within coherent structures, downstream of the sweep events, creating low pressure zone at their cores near the top of the grain (Jackson 1976, Schmeeckle *et al.* 2007, Smart & Habersack 2007) and interacting with the shear layers near the bed, (*ii*) the effect of vortex shedding from the grain itself (Kalinske 1947,

Hofland *et al*. 2005) and its effect on top, back and bottom of the grain, (*iii*) or the combination of (*i*) and (*ii*).

6.2 Cylinder Tests

The representative patterns for the ensemble average pressures and the flow velocities from cylinder test with D = 33.4 mm are shown in Fig. 22. Similar patterns were observed for the data with different diameter cylinders.

The waveforms of $p^+_{2\text{-}4}$ do not exhibit multiple (and out of phase) peaks over the 200 ms window as were observed in the uniform flow case. This is one of the main differences between the two flow cases. A strong drop in p^+_3 takes place about the same time as the peak in p^+_1 initiates, which is followed by a positive peak in p^+_1 and then in p^+_3. Considering the location of the pressure measurement points, the signature of a certain flow structure is first expected to be observed in p_1 and then in p_3 and finally in p_2. Unlike the uniform flow case, the cylinder test results follow this order as can be seen by the instants of peaks occurring in p^+_1, p^+_2 and p^+_3. This observation suggests that the out of the phase peaks in p^+_3 (Fig. 21) in uniform flow are caused by coherent structures of fully developed turbulent flow. The flow velocity patterns again suggest the connection between high speed fluid motion towards the bed (a sweep like event) and the peak in p^+_1.

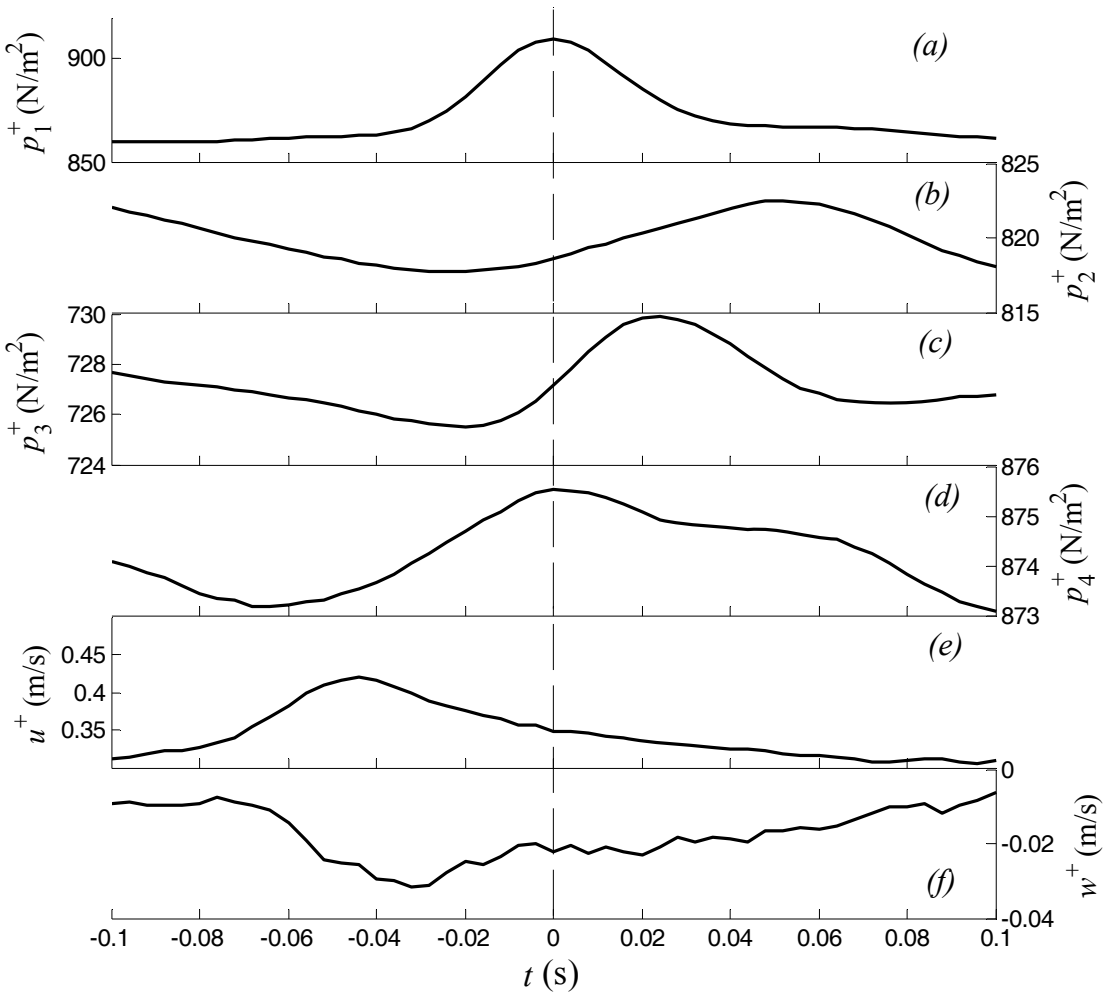

Figure 22. Ensemble average waveforms of conditionally sampled pressures ($p_{1\text{-}4}$) and velocities (u and w) from top to bottom (a)-(f), based on the detected positive peaks in p_1 signal. $t = 0$ is the instant when the peaks in p_1 were detected. Data from cylinder test D1 was used and the ensemble average values are based on detected 923 positive peaks. Threshold level, $H = 2$.

7. Conditionally Sampled Force Fluctuations

7.1 Uniform Flow Conditions

Another difference between the fully developed uniform flow case and the flow in the wake of the cylinder is that, both the horizontal and vertical pressure gradients (conditioned on the local maxima in p_1) acting on the grain appear to be higher in the presence of the cylinder. The horizontal and vertical gradients of the ensemble average of conditionally sampled pressures ($p^+_1 - p^+_2$ and $p^+_4 - p^+_3$), referred to as drag and lift forces from here on (for both conditionally sampled and instantaneous values), are given in Fig. 23 (data from runs UC, A1 and A9). Note that the vertical pressure gradient excludes the hydrostatic pressure difference between the locations of p_4 and p_3 ($\gamma \Delta z$, where γ is the specific weight of water and $\Delta z = d = 12.7$ mm) to eliminate the buoyancy effect. That is, the lift force estimated in this fashion will be compared against the submerged weight of a 12.7 mm, Teflon® grain (e.g. p_{crit}). The waveforms from runs A1 and A9 were also included along with the undisturbed flow condition for the cylinder tests (UC) to represent the upper and lower limits of the pressure gradients respectively for uniform flow conditions.

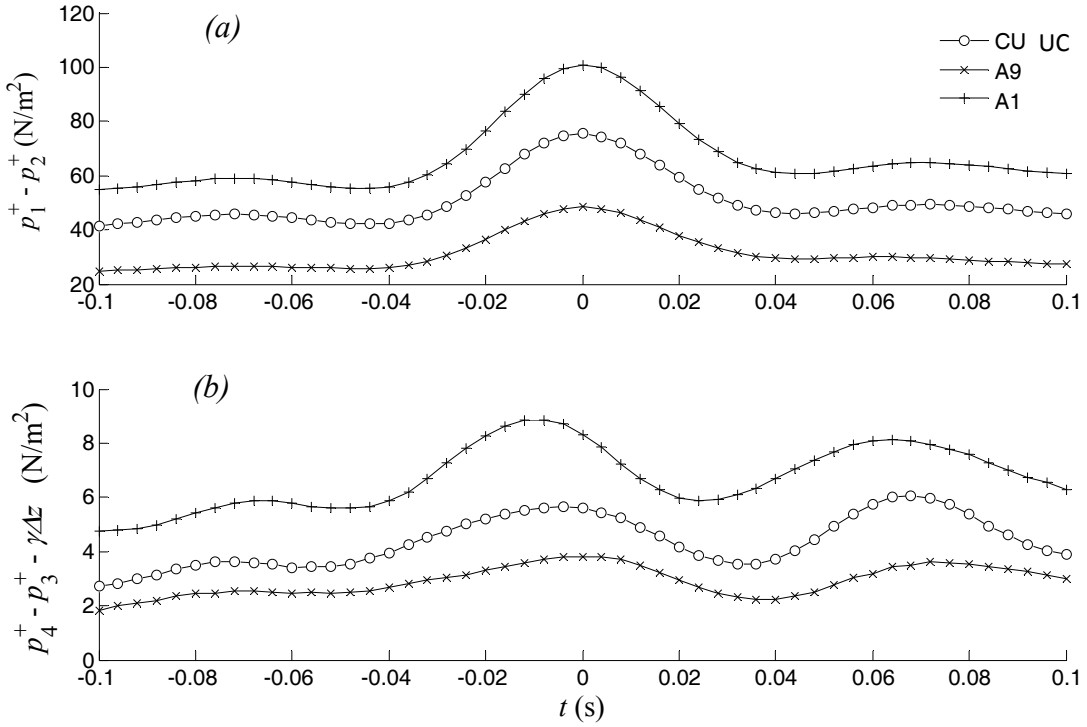

Figure 23. The waveforms for the horizontal and vertical differences of ensemble average of the conditionally sampled pressures (top (*a*) and bottom (*b*) figures respectively). $t = 0$ is the instant when the peaks in p_1 were detected. Data from runs A1, A9 and UC were used. Threshold level, $H = 2$.

The vertical pressure difference in Fig. 23 indicates an average upward lift, about 4% of the critical pressure, p_{crit}, over the 200 ms window centering the peaks in drag force. The contribution of p^+_3 to this average positive vertical pressure difference is 65%. A peak occurs in the vertical pressure difference (~lift force) 5 to 10 ms before the peak in the horizontal pressure difference (~drag force) and is dominated by p^+_3 (out of phase with p^+_1). The second peak in the lift force, again essentially caused by a drop in p^+_3, is observed about 65 ms after the peak in drag and 73 ms after the peak in u^+. The latter

delay indicates a convection velocity of about 10u*, comparable to findings reported in the literature (Laadhari *et al*. 1994). Both of these peaks in p^+_3 (Fig. 23) correspond to about 6% of the $p_{crit,}$ sufficient to momentarily reduce the threshold level for particle entrainment and potentially aid in dislodgement. The valleys in lift force (for example the instants at -0.050ms and +0.030 ms in Fig. 23), by contrast, are caused by drops in p^+_4. It is clear that the peak in drag force, dominated on the average by positive contributions from p^+_1 (118%) accompanied by negative contributions from p^+_2 (-18%), is strongly related to the acceleration in u^+ and deceleration in w^+. The second peak in the lift which occurs after the peak in the drag also (dominated by p_3, see Figs. 15 and 19 for CCFs between p_3 and the flow velocities) is related to the acceleration in u^+ and deceleration in w^+ (this is assuming a constant convection speed, 10u*, and the distance which the flow structure has to travel to have influence at the location of p_3). Nevertheless, it is not reasonable to link the aforementioned first peak in the lift force (Fig. 23(*b*)) to the same effect. Because that peak occurs before the peak in the drag force and about the same time as the peak in u^+. Therefore, the cause for this first peak in the lift force cannot be the acceleration in flow towards the bed. While the measurements in this study do not indicate a definite source for this phenomenon, interactions of vortices with the grain particularly at the interface (shear layer) of low and high speed fluids near the bed might be creating low pressure zones and eventually a strong drop in p^+_3 and an upward lift force. Such vortices were observed by Cameron (2006) and Detert *et al*. (2010*b*) to occur near the bed downstream of sweep events. This interpretation is also consistent with the findings of Hofland (2005*a*), Smart & Habersack (2007) and Schmeeckle *et al*. (2007).

7.2 Cylinder Tests

Figure 24 presents the waveforms of $(p^+_1 - p^+_2)$ and $(p^+_4 - p^+_3 - \gamma\Delta z)$ from the cylinder test with D = 33. 4 mm. Similar to the results from the uniform flow case, peaks in the lift force are observed occurring before and after the peak in the drag. But , unlike the uniform flow case, the first peak in the lift shown in Fig. 24 is a result of a steady drop in the pressure on top of the grain (see Fig. 22), coinciding with a steady increase in the bottom pressure occurring right before the peak in drag force occurs. The same behavior in the lift forces for both uniform and cylinder wake flows caused by slightly different pressure patterns in p_3 and p_4 indicates that this might be a dominant instability inherent to the geometry used here. The presence of the cylinder does not increase the relative magnitude of the peaks in drag and lift forces but causes a significant increase in the average lift $<p^+_4 - p^+_3 - \gamma\Delta z>$ force during the 200 ms window centered on the peaks in drag force. (angle brackets denote averaging over the specified duration and will later be used to indicate averaging over the peak pressure duration, T). It is calculated that the overall lift acting on the grain during the observation window is 27% of the p_{crit} (a nearly 7 fold increase compared to uniform flow conditions) and the peaks in the lift can reach up to 32% of the p_{crit}. The shift in the average lift force during peaks in drag is most likely associated with increased flow velocities (due to the presence of the cylinder) generating a permanent low pressure zone over the uppermost layer of the bed via a Bernoulli effect as suggested by Brayshaw et al. (1983). Such relatively small changes in the effective weight of the particle have been shown to be responsible for significant changes in the particle entrainment frequency by Celik *et al*. (2010). The reason for the significant increase in the bedload activity with minute increase in the turbulence level as

Nelson *et al*. (1995) and Sumer *et al*. (2003) observed can also be attributed to the modification of the average lift force during extreme drag forces by the flow structures in the cylinder wake which makes the particles effectively lighter.

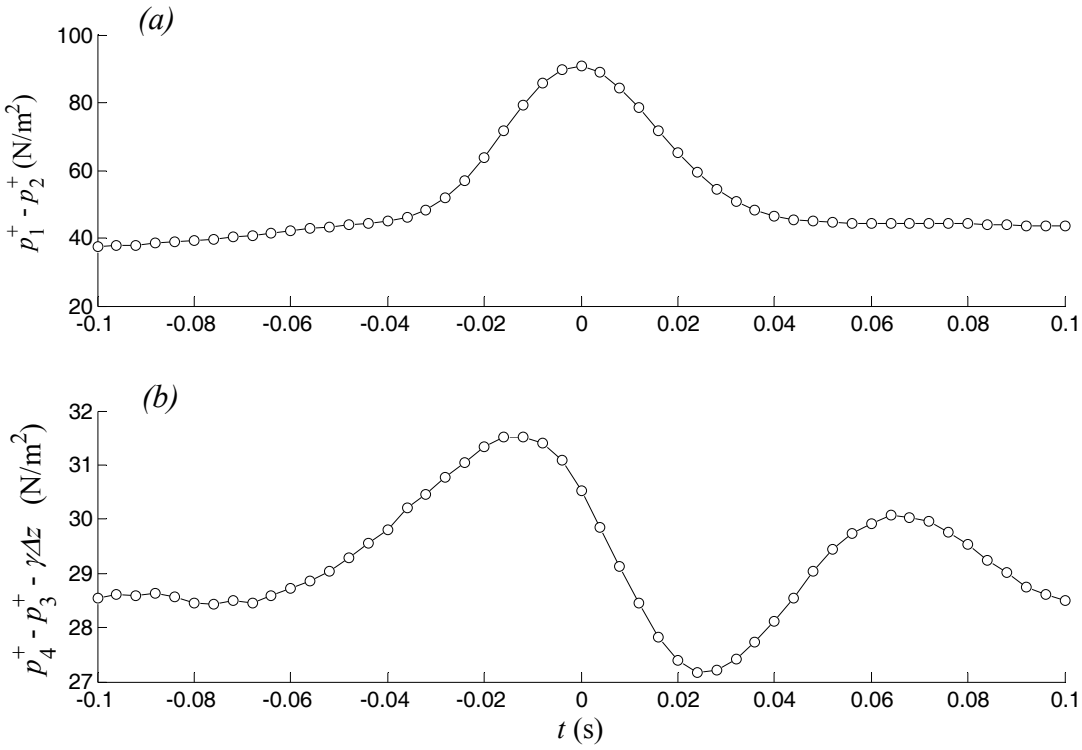

Figure 24. The waveforms ensemble average of the conditionally sampled horizontal and vertical pressure gradients (top (*a*) and bottom (*b*) figures respectively). $t = 0$ is the instant when the peaks in p_1 were detected. Data from cylinder tests with $D = 33.4$ mm were used. Threshold level, $H = 2$.

About 30% of the detected peaks in drag force coincided with lift events which were below the ensemble average lift for both uniform flow and cylinder tests. The peak detection method (with $H = 2$) was applied to the instantaneous lift force ($p_4 - p_3 - \gamma\Delta z$) to

detect the patterns of flow velocities and drag forces associated with extreme positive lift events.

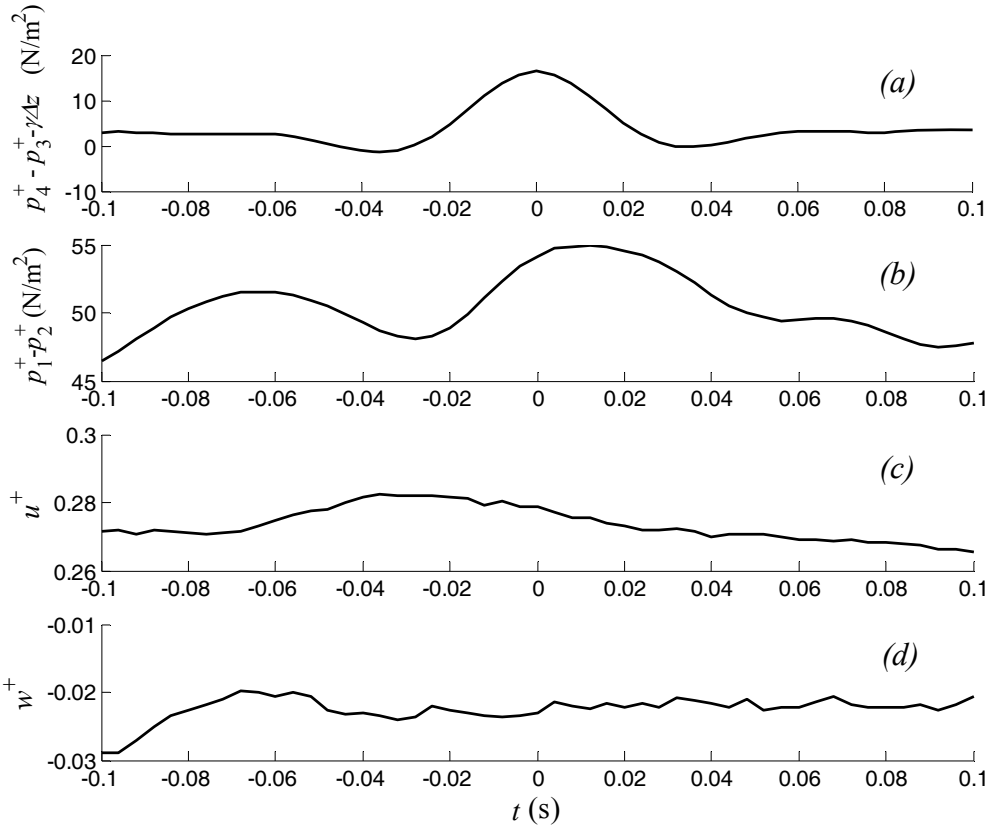

Figure 25. Ensemble average waveforms of conditionally sampled lift force and velocities (u and w) from top to bottom, based on the detected positive peaks in p_1 signal. $t = 0$ is the instant when the peaks in p_1 were detected. Data from cylinder test D1 was used and the ensemble average values are based on the 923 detected positive peaks. Threshold level, $H = 2$.

In Fig. 25, the ensemble average lift force, $(p_4 - p_3 - \gamma\Delta z)^+$, is given together with accompanying (ensemble average) conditionally sampled drag force, $(p_1 - p_2)^+$, u^+ and w^+ for run UC. The figure shows that the relative peak in the lift force, about 10% of the

p_{crit} (Fig. 25(*a*)) coincides with sweep like events, but the acceleration in u^+ and deceleration in w^+ are not as strong as they were in Figs. 21(*e*) and 21(*f*). There are very small variations (~10 N/m^2) in the drag force about 65 ms before and 15 ms after the extreme lift event.

8. Instantaneous Forces

8.1 Force Magnitudes

The instantaneous drag force was observed to be momentarily reaching up to 6 times the mean value and it was very rarely observed to be negative (see Fig. 7). Though curious, this phenomenon is not without a precedent as it was also observed in the measurement of forces acting on a spherical particle near a rough wall by Schmeeckle *et al*. (2007), although upstream drag was not commented upon by the authors themselves.

CCFs between instantaneous drag and lift forces are given in Fig. 26. The flow patterns detected for the conditionally averaged waveforms (based on the peaks in p_1) also appear to be present during the entire signal duration judging by the double peaks in the CCF. That is, the effect creating the peak lift force just before the peak in the drag is a consistent near-bed phenomenon. The highest peak is observed at Δt = -0.012 s with a correlation coefficient of 0.45, indicating a modest relation between drag and lift. This prominent feature is accompanied by a secondary peak at Δt = +0.060 s, $R(\Delta t)$ = 0.42 in the cross correlation function in Fig. 26.

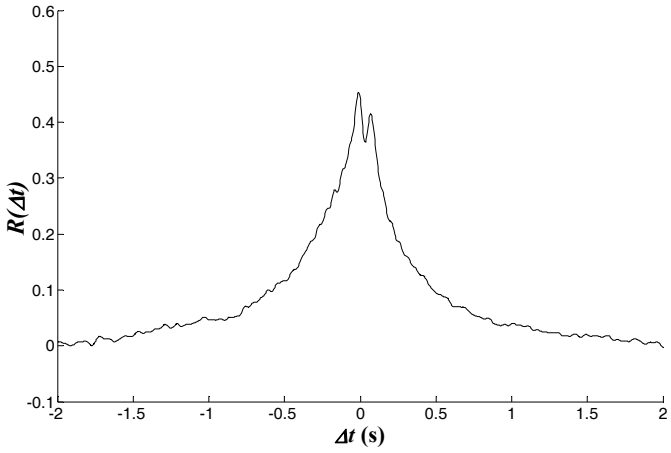

Figure 26. CCF between drag and lift forces from run A2.

Figure 27 shows the plots of CFFs between the flow velocity component and the drag force. The plots of CFFs between the flow velocity component and the lift force are given in Fig. 28. Similar patterns were observed in all uniform flow and cylinder test data therefore the statements below apply to all. Besides the expected patterns in the flow velocities and the lift force corresponding to the peaks in the drag force shown earlier, dependency of the instantaneous drag force on w is apparent. This is consistent with the findings of Hofland *et al*. (2005). The instantaneous lift force is correlated with u to some degree (R = 0.37, Fig. 28) contradicting the findings of Schmeeckle *et al*. 2007. Interestingly, the lift force shows a very weak correlation with w. This finding does not support the models occasionally employed for incipient motion criterion, where the instantaneous lift is associated with the instantaneous vertical velocity squared.

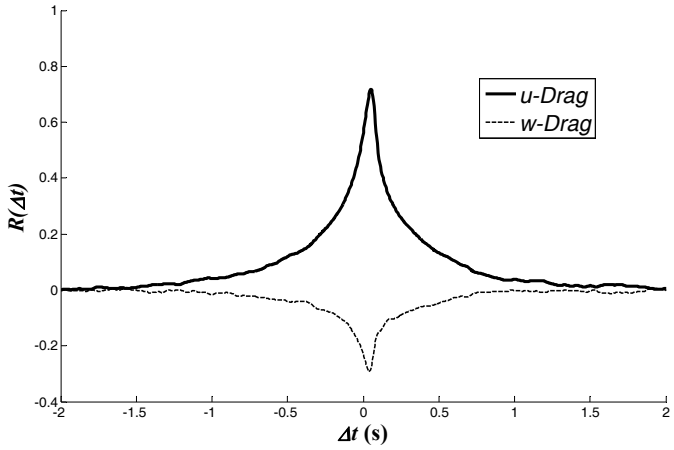

Figure 27. CCFs between *u* and drag force (bold line and) *w* and drag force (dashed line) from run A2.

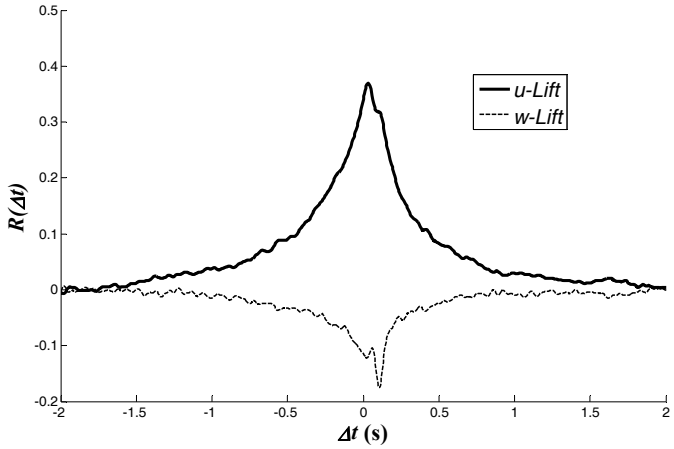

Figure 28. CCFs between *u* and lift force (bold line and) *w* and lift force (dashed line) from run A2.

It is interesting to note that the time average value of the vertical pressure difference ($\overline{p_4 - p_3 - \gamma \Delta z}$) over the entire duration of a run for uniform flow conditions varied between +0.5% and -1.5 % of the p_{crit} (Series A1 – A9, UC) with a very weak inverse relation to *Re**. The instantaneous values of ($p_4 - p_3 - \gamma \Delta z$) (lift), however, were

observed to occasionally reach up to nearly 50% of the p_{crit} in magnitude in both upward and downward directions. The histograms of the ($p_4 - p_3 - \gamma\Delta z$), normalized with p_{crit} using data from UC and D1 are given in Fig. 29 to demonstrate the variability in the instantaneous lift force. It is shown that the lift force can instantaneously reach up to 80% of the p_{crit} in the wake of the cylinder for D=33.4 mm. As the cylinder diameter decreases, the histogram is shifted slightly to the left. It is clear that the lift force alone is not capable of dislodging the fully exposed grain from its pocket (analysis considered a 12.7 mm diameter Teflon® grain) but it can momentarily achieve very high values, high enough to generate favorable conditions for grain entrainment, particularly in the wake of a cylinder. In addition, the increase in the mean lift force in the wake of the cylinder enhances the sediment transport by decreasing the effective particle weight.

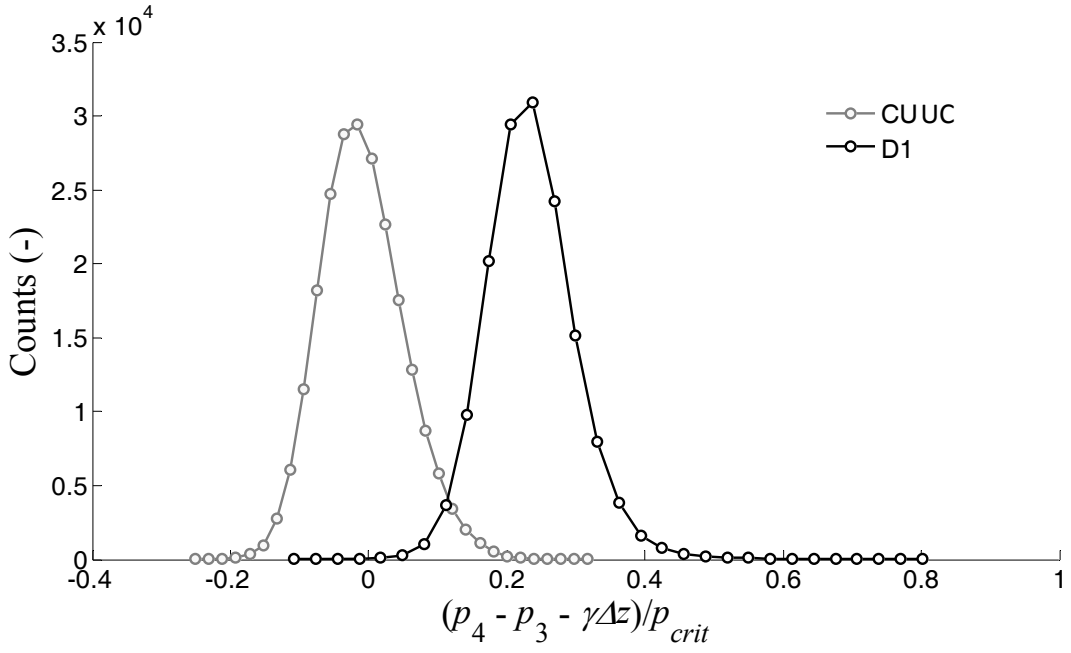

Figure 29. The histograms of the instantaneous lift force normalized with the critical pressure from runs UC and D1.

8.2. Force Event Durations

The magnitude of instantaneous pressure and force peaks has been advocated to be the relevant parameter for particle entrainment (see for example Hofland *et al*. 2005 and Schmeeckle *et al*. 2007). Yet, Diplas *et al*. (2008) and Celik *et al*. (2010) provided evidence that not every peak in the forces, even when exceeding the threshold value, results in particle entrainment. They demonstrated that the duration, T, of peak events is as important as the peak magnitude.

The impulse detection method used here identified the time of occurrence and duration of events during which the magnitude of the positive pressure fluctuation (in the low pass filtered) p_1 is higher than 2 times the p'_{1rms} ($H = 2$). In addition, time-averaged p_1 values, $\langle p_1 \rangle$, over the peak duration, T, were computed for each such event with $p' > 2p'_{rms}$ (angle brackets denote averaging over peak duration). Note that this method differs from the peak detection algorithm in that multiple consecutive peak events which are regarded as individual peaks (and data points) in the latter are detected as one peak in the duration analysis as long as they are all above the threshold level. This difference is depicted in Fig. 33. A peak event on the left, well above the threshold level (detected earlier as in Fig. 19), also qualifies as an event here with finite duration. The two local peaks on the right however form together one peak event with a relatively longer duration.

Implementing this procedure results in series of random peak pressure events, associated $\langle p_1 \rangle$, and durations, T, for each run (Fig. 30). The association of the identified peaks with the other pressures and flow velocity components was obtained through the time of occurrence of the peaks in p_1. In order to account for the phase delay between the

flow velocity and pressure signals due to the distance between the pressure measurement points and the location of the LDV measurement volume, the flow velocity records were shifted forward by the lag time obtained at the rise point in the cross correlation function between u and p_1 (Fig. 15). In this way, the near-bed flow events and the pressures they generate on the particle were matched in time before the event duration analysis was performed. More explicitly, all pressure signals were synchronized with u-w pairs by using a single time delay that was obtained between u and p_1, which is the strongest and the most relevant relation for the bed configuration studied here. Subsequently, each peak in p_1 was associated with an event averaged p_2, p_3, p_4, u and w over the peak duration (denoted by angle brackets).

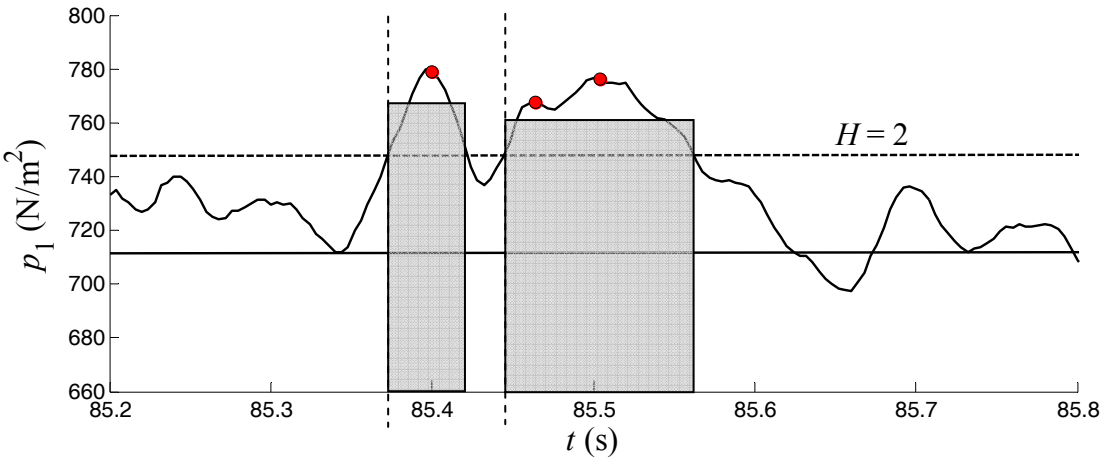

Figure 30. Representative time series of (filtered) p_1 from run A2. The detected local peaks with $p' > 2p'_{rms}$ are shown with solid circles. Time average p_1 is specified with horizontal, solid line. The widths of the shaded rectangular areas indicate the detected event durations, T, while the heights indicate the average p_1 over duration T ($<p_1>$). The vertical dashed lines show the time of occurrence of events for the duration analysis.

The distribution of peak durations in p_1 are heavily and positively skewed (Fig. 31) and is described well by the extreme value distributions: Wakeby (p-value = 0.99), General extreme value (p-value = 0.86), and 3 parameter log-normal (p-value = 0.67). The extreme durations in uniform flow cases (based on $H = 2$) were exceeding 500 ms.

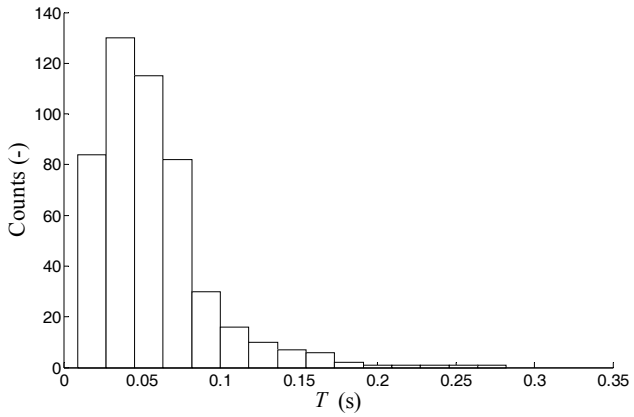

Figure 31. Histogram of the 478 events peak durations detected in p_1 ($H = 2$). Data from UC was used.

The relation between the duration and magnitude of peak pressures, as well as with the flow velocity components are given in Figs. 32(*a*) and 32(*b*). The surface plots indicate that events lasting longer than 100 ms and magnitudes well over the threshold level occur predominately in the high u and negative w region implying association with sweep like events. Such events also occur occasionally in the region of outward interactions ($u' < 0$ and $w' > 0$). A precise relation between the magnitude and duration in peak p_1 events is not apparent, although events with extremely high durations were generally not associated with the highest event magnitudes. This can be seen by matching the high values of duration and magnitude on the identical $\langle u \rangle$ -$\langle w \rangle$ plane in Figs. 32(*a*) and 32(*b*). Note that all of the event magnitudes seen in these figures are above the

threshold value of p_1. The magnitude of the local average p_2 and p_3 signals concurrent with the peak events in p_1 are given in Figs. 32(*c*) and 32(*d*) respectively, again on the <*u*> -<*w*> plane.

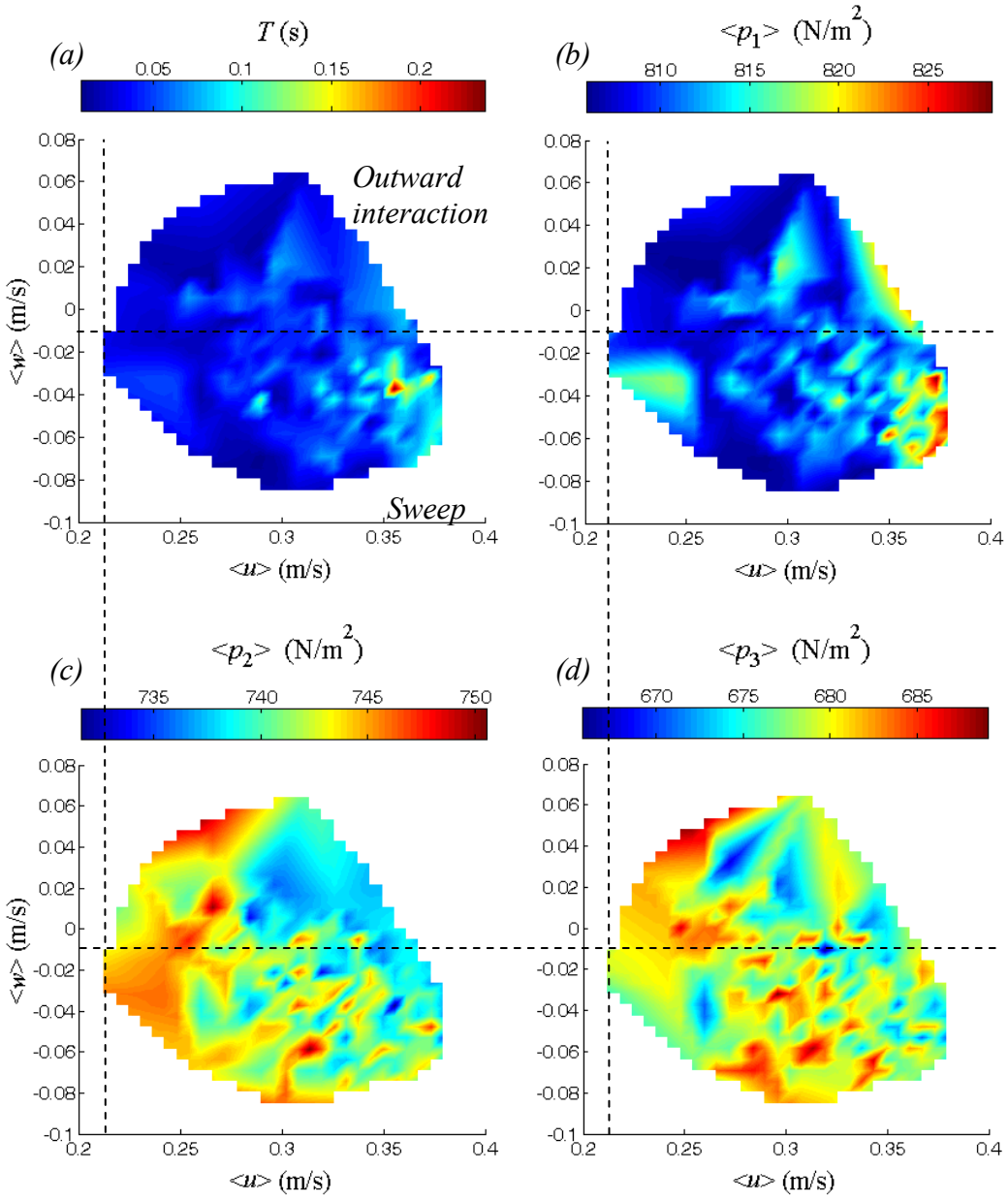

Figure 32. The surface plots of the peak event durations (*a*), magnitudes of p_1 signal (*b*), magnitudes of p_2 signal (*c*), magnitudes of p_3 signal (*d*) on <*u*>-<*w*> plane. Data from

run UC was used and 478 events with finite durations are represented. Color bars represent the duration (*a*) and magnitude (*b*), (*c*), (*d*) of pressure peaks. Note that the same colormap was used for different scales in the subplots. Horizontal and vertical dashed lines indicate the time average *u* and *w* values over the entire test duration respectively. Data from run UC.

One consistent behavior common to these two pressures is the lower values corresponding to high duration regions in p_1. This confirms the findings from the CCFs between the pressures presented earlier (Fig. 9). The time delays between individual pressures in the event duration analysis here intentionally haven't been taken into account in order to picture the concurrent pressures at a given instant (or peak duration) as felt by the grain. The magnitude of p_4 doesn't show any particular correlation to peak magnitudes nor to duration in p_1, while having high magnitudes during sweep like events where the event durations were higher (Fig. 33(*a*)). A joint histogram of the $\langle u \rangle$ and $\langle w \rangle$ pairs is presented in Fig. 33(*b*) to provide information about the frequency of occurrence of events shown in Figs. 33(*a*) and 32(*a*-*d*).

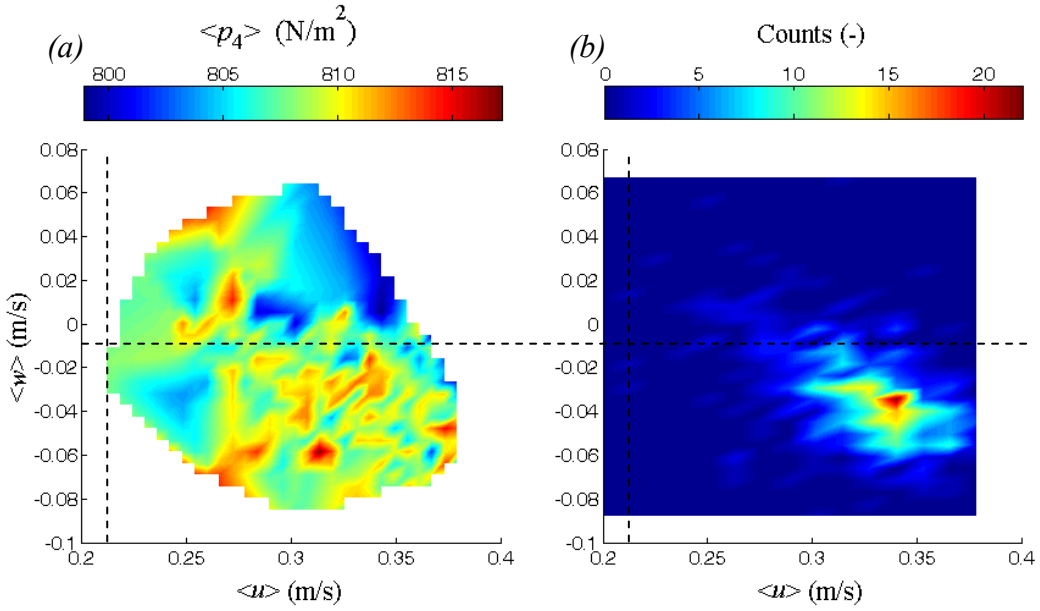

Figure 33. The surface plots of the magnitudes of p_4 signal on <*u*>-<*w*> plane (*a*), two dimensional histogram of the <*u*> and <*w*> (*b*). The color bar in (*b*) represents the number of counts for the 2D histogram. Horizontal and vertical dashed lines indicate the time average *u* and *w* values over the entire test duration respectively. Data from run UC.

A feature observed for all of the uniform flow conditions was that the high duration region in the sweep events yield angle of attacks (inclination angle of the velocity fluctuations from the horizontal plane) between 7° and 19° (obtained using the data of Fig. 33(*b*)). Keshavarzi & Gheisi (2006) reported high sediment activity occurring with angle of attacks near the upper limit reported here. The peak events did not occur during ejection ($u' < 0$ and $w' > 0$) and inward interaction like events ($u' < 0$ and $w' < 0$). The distribution of pressure magnitudes and duration (based on p_1) on the <*u*>-<*w*> plane, in relation to the impulse based incipient motion model, implies that the sweep and outward interaction like events near the bed are effective in particle dislodgement which has also been reported earlier by Nelson *et al*. (1995) and more recently by Cameron

(2006). The dominance of these two near-bed events in particle removal has often been attributed to the frequent high streamwise velocities and resulting high forces. However, the occurrence of high event durations along with high magnitudes (for p_1), i.e. high impulse magnitudes, during the sweep and outward interaction type events is more descriptive of the actual physical processes leading to higher sediment movement rates.

Characterization of drag events with both high duration and magnitude and the concurrent associated lift forces is essential for developing better incipient motion models. In order to explore the coupling between the peak drag force magnitudes and durations with the lift forces occurring during these peak events, the duration detection method was applied to p_1-p_2 with $H = 2$. The duration of events based on drag force magnitude and their frequency of occurrence are given in Figs. 34(*a*) and 34(*b*) respectively on the drag-lift plane for the uniform flow condition test, UC. Note that these force and duration patterns are for a fully exposed grain and our assessments pertain to rolling motion of this particle. Extreme events with relatively high durations (e.g. >100 ms), and high drag and lift forces were observed, although very rarely (Fig. 34(*b*)). In addition, there were events occurring more frequently than the extreme events, with durations between 50 ms and 100 ms, and positive lift and high drag force magnitudes. The most frequent events however were characterized by shorter durations (50 ms or below). These events also imparted lift forces near zero and relatively low drag force on the particle compared to the extreme event durations.

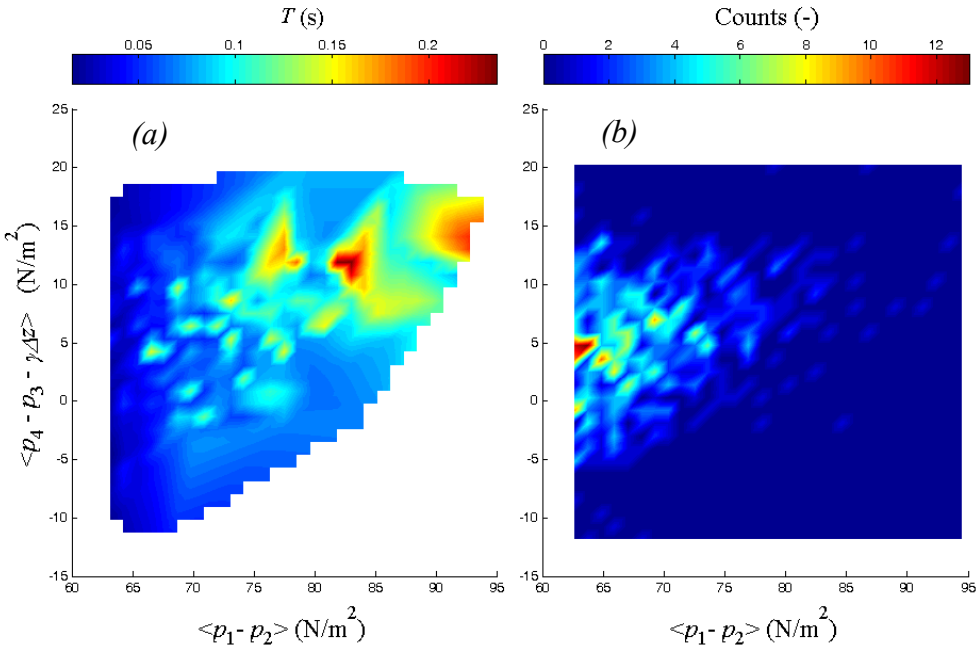

Figure 34. The surface plots of the durations of drag force signal on drag-lift plane (*a*), two dimensional histogram of the drag and lift (*b*). The color bars in (*a*) shows the event durations and in (*b*) represents the number of counts for the 2D histogram. Data from run UC.

Plots similar to that of Fig. 34 for the cylinder test data are given in Figs. 35 (*a*) and (*b*). The same arguments for the uniform flow case are also valid here only this time the average lift force is positive with significantly high magnitudes.

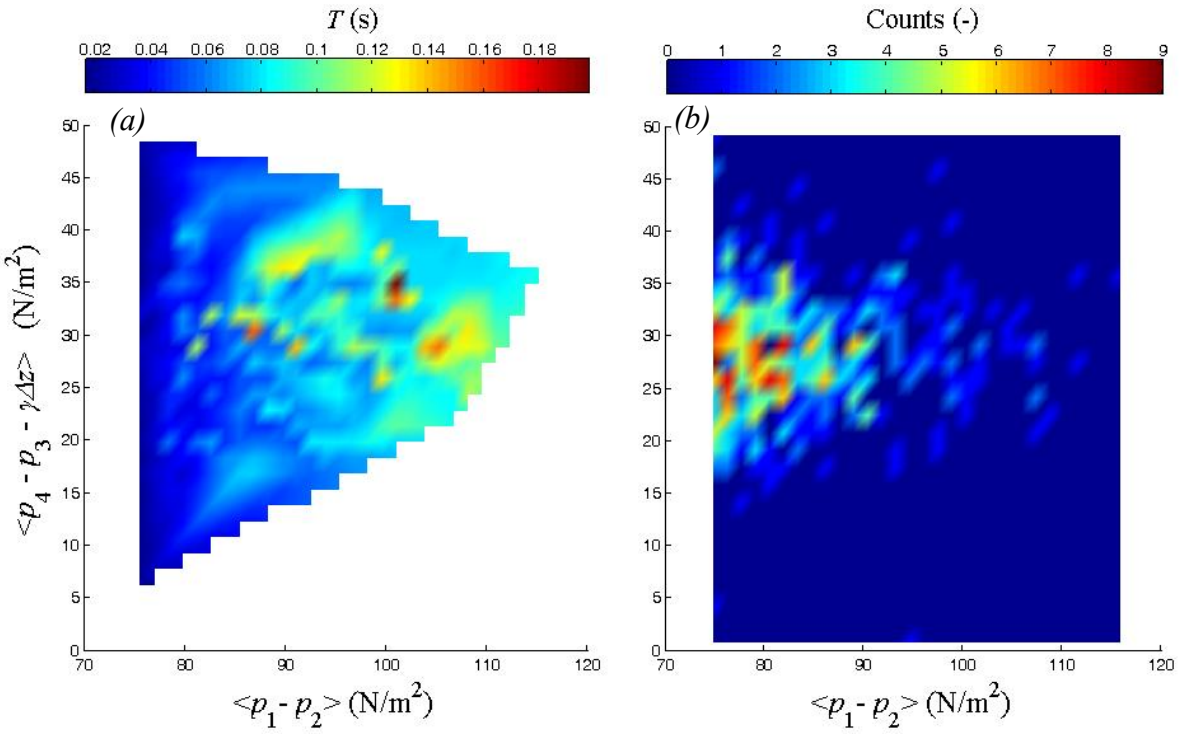

Figure 35. The surface plots of the durations of drag force signal on drag-lift plane (*a*), two dimensional histogram of the drag and lift (*b*). The color bars in (*a*) shows the event durations and in (*b*) represents the number of counts for the 2D histogram. Data from run D1.

9. Discussion on the Time Delay between Flow Velocity and Pressures

As mentioned earlier, there is a time delay between the flow velocities measured one diameter upstream of the instrumented grain and the pressure acting on it due to the distance between the LDV measurement volume and the pressure measurement location (Fig. 6). As the pressure is conveyed very rapidly throughout the flow field, the time delay we consider here is associated with the measured velocity and when that parcel of fluid actually contacts the instrumented grain. This time delay is best judged by utilizing the correlation between p_1 and u (Fig. 15, i.e. the time delay corresponding to the

maximum of their cross correlation function) as the strongest correlation appears between these two signals. Representative time series of synchronized u and p_1 using the appropriate time delay from run A2 are shown in Figs. 36(a) and 36(b) respectively. The p_2 signal synchronized with u using the same time delay is given in Fig. 36(c).

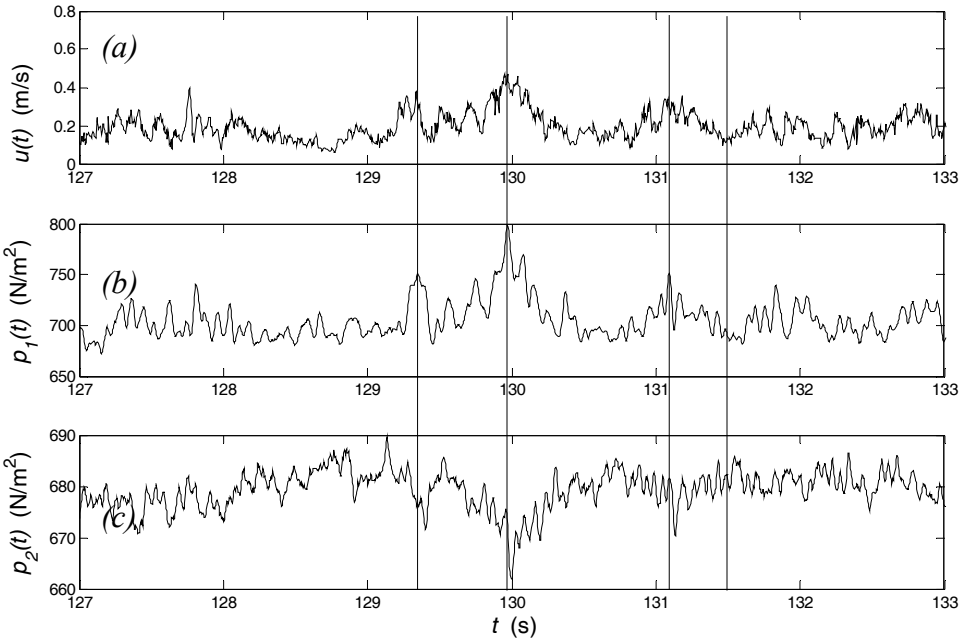

Figure 36. Time traces of the synchronized streamwise flow velocity, u (a) the pressures acting on the front the particle, p_1 (b) and the pressures acting on the back of the particle, p_2 (c). Data from run A2 is presented. Vertical lines show flow structures which have reverse effects on p_1 and p_2.

Results presented earlier in this study indicate that the pressures in the front and back of the grain are negatively correlated (Fig. 9(a)). Figure 36 clearly illustrates examples of such flow events (shown with vertical lines). Based on these findings, one should expect that, when u increases, p_1 should also increase and p_2 decrease at the same

time leading to a relatively higher drag force. The opposite can also be said for decreasing u. Such conditions are not anticipated to generate relatively lower drag forces for high u and higher drag forces for low u values. As a result, the variability in the instantaneous drag coefficient, C_D, , is not expected to be very large. However Schmeeckle *et al*. (2007) reported that the instantaneous drag coefficient is well below the average drag coefficient for high u values compared to the time average drag coefficient. Therefore, instantaneous drag force is overestimated if a constant drag coefficient is used. It is clear that our findings of the previous section contradict Schmeeckle *et al*.'s (2007). The origin of this apparent inconsistency lies in the fact that, as our measurements demonstrate, there is a phase delay between the surface pressures at the front and rear of the grain, i.e between p_1 and p_2. Figures 15 and 17 show that the flow structures detected at one diameter upstream of the grain (via $u(t)$) first reach the upstream face of the grain (at the time $t+\Delta t_1$, where Δt_1 is the phase delay between u and p_1) and influence the pressure in the front ($p_1(t+\Delta t_1) \propto u(t)$) and then after an added convection time $\Delta t_1 - \Delta t_2$ (where Δt_2 is phase delay between u and p_2) influence the pressure at the back of the grain ($p_2(t+\Delta t_2) \propto u(t)$). Figure 38 shows that $\Delta t_1 < \Delta t_2$ as it takes a longer time for a flow structure to affect the back of the grain compared to the front. That said, and assuming that the viscous drag acting on the grain is negligible (Wang 1999) and that the instantaneous horizontal pressure difference represents the form drag (Hofland *et al*. 2005, Vollmer & Kleinhans 2007, Detert *et al*. 2010(*a*)), these results imply that the conventional quasi-steady drag equation, coupling the instantaneous near-bed velocity in a turbulent channel flow to the drag force is inappropriate, even as a

surrogate for the phenomena. That is, the quasi-steady drag expression implies that $u^2(t)$ is proportional to drag force at time $(t+\Delta t_1)$. This is not the case because the phenomena (in the present work for fully rough turbulent channel flow) involve two phase delays instead of one. This effect is likely to be most pronounced for sediment grain-turbulent flow interactions where the flow structures are comparable in size to the grain. This observation helps to explain the inadequacies of incipient motion models that employ the standard drag equation to estimate the instantaneous drag forces.

10. Summary and Discussions

Experimental results from a range of uniform flow conditions and flow in the wake of various size cylinders mounted spanwise above the bed in otherwise fully developed flow, all representing near threshold conditions, are presented to document the characteristics of the instantaneous surface pressures and forces acting on a spherical grain and their relation to the near-bed flow velocity. Implications about mechanisms for particle dislodgement are discussed as well.

The pressure fluctuations on the front and top of the spherical grain were observed to be the major contributors to the instantaneous forces acting on the grain. p'_{rms}/τ_0 ratios for the front and top measurement locations were near 18 and 7 respectively. These ratios increased by a factor of two in the presence of the cylinders while the mean pressure values did not change considerably. The force obtained from horizontal pressure difference was found to be as high as 6 times its mean value. These findings demonstrate the inadequacies of incipient motion models that employ time-space average flow parameters. For instance, the p'_{rms}/τ_0 ratios reported here indicate that the

Shields curve which has been the most widely used criterion for determining incipient motion is in fact a further educated guess, rather than an accurate measure of the phenomenon.

Two distinct phase delays between the instantaneous pressures on the front and top of the particle were determined. These phase delays were shown to be in agreement with the occurrence of the peaks in pressure patterns obtained by the conditional sampling method based on the peaks in the pressures acting in the front of the particle. Force patterns based on the peaks in the horizontal pressure gradient were also obtained. These patterns, in which a strong upward lift was observed before and after a peak event in drag force occurred consistently as a result of strong unsteady drops in the pressure on the top of the grain for uniform flow conditions. The drop in the pressure on the top of the grain was observed to be steady. Regardless of the flow cases tested here, the resulting strong upward lift forces generated favorable conditions for particle entrainment. The first peak in the lift force observed in the conditionally averaged patterns is most likely associated with the localized hairpin vortices with low pressure cores traveling downstream of sweep type of events. Recent findings in the literature support this description. Cameron (2006) reported strong accelerations in streamwise velocity following hairpin vortices near the bed just before the initiation of particle movement. Detert *et al*. (2010*b*) detected hairpin vortex packages 2-4*d* long in the streamwise direction near the rough bed which generated low pressure zones on the uppermost layer of the bed. The second peak we observed in the lift force patterns was shown to be strongly related to the passage of sweep type events under uniform flow conditions. The lift force was positive, upward during the peak drag events for both the

uniform channel flow and cylinder wake flows. This effect was augmented in the presence of the cylinder. Specifically, the conditionally sampled force waveforms showed that the ensemble average lift force increased significantly (nearly 7 fold) in the wake of a cylinder, compared to the uniform flow conditions. This phenomenon was also observed in the time average lift forces, reducing the effective particle weight permanently in the presence of the cylinder which leads to significantly higher particle entrainment rates. It was also observed that the instantaneous peaks in the lift force occasionally reached magnitudes nearly 80% of the submerged weight of the particle in the wake of a cylinder. The results from conditional sampling method based on extreme lift events showed no strong relation between the peak lift events and the drag force or near-bed flow velocity components. Nevertheless, for the fully exposed grain configuration considered here, the lift force was shown to be of importance for particle entrainment and therefore shouldn't be neglected.

The duration of the pressure peaks and also the peaks in the pressure gradients were also investigated. The results showed that long duration (100 ms or longer) events in the frontal pressure were associated with sweep like events in the flow with relatively high frequency. Such high stagnation pressure episodes also occurred during outward interactions, but rarely. The long duration, high magnitude drag forces accompanied by high lift forces were infrequent.

Finally these measurements revealed that the instantaneous coupling between the streamwise flow velocity and the drag force involves more than one phase delay considering the contributions of the pressures on the front and back to the drag force.

Therefore we propose that the standard drag formula should be used cautiously for instantaneous drag force estimations.

Our results using the instantaneously measured surface pressures acting on a fully exposed spherical grain under various flow conditions, despite the simplified bed geometry employed revealed the important characteristics of certain flow and forcing events with a potential to dislodge the grain. The duration and magnitude characteristics of the force events as well as their association with the near-bed flow are believed to be significant in describing the actual processes responsible for particle entrainment and the inadequacies of existing incipient motion models.

Acknowledgements

The support of the National Science Foundation (EAR-0439663, EAR-0738759 and CBET-1033196) and Army Research Office is gratefully acknowledged. The writers also thank Mr. Colin Steward for his contribution in the flume vibration tests.

References

Ancey, C., Bohm T., Jodeau M. & FREY P. 2006 Statistical description of sediment transport experiments. *Phys. Rev. E* 74(1), 011302.

Balakrishnan, M. 1997 The role of turbulence on the entrainment of a single sphere and the effects of roughness on fluid-solid interaction. PhD thesis, Virginia Polytechnic Institute and State University.

Brayshaw, A. C., Frostick, L. E. & Reid, I. 1983 The hydrodynamics of particle clusters and sediment entrapment in coarse alluvial channels. *Sedimentology* 30(1), 137–143

Bushnell, D. M. & McGinley, C. B. 1989 Turbulence control in wall flows. *Annu. Rev. Fluid Mech.* 21, 1–20.

Cameron, S. M. 2006 Near-boundary flow structure and particle entrainment. PhD thesis, University of Auckland.

Celik, A. O., Diplas, P., Dancey, C. L. & Valyrakis, M. 2010 Impulse and particle dislodgement under turbulent flow conditions. *Phys. Fluids* 22, 1–13.

Cheng, N. S., Law, A. W. K. & Lim, S. Y. 2003 Probability distribution of bed particle instability. *Adv. Water Resour.* 26(4), 427–433.

Derksen, J. J. & Larsen, R. A. 2011 Drag and lift forces on random assemblies of wall-attached spheres in low-Reynolds number shear flow *J. Fluid Mech.* DOI: 10.1017/S0022112010006403

Detert, M., Weitbrecht, V. & Jirka, G. H. 2010*a* Laboratory measurements on turbulent pressure fluctuations in and above gravel beds. *J. Hydraul. Engng* 136(10), 779–789.

Detert, M., Nikora, V. & Jirka, G. H. 2010*b* Synoptic velocity and pressure fields at the water-sediment interface of streambeds. *J. Fluid Mech.* 660, 55–86.

Diplas, P., Dancey, C. L., Celik, A. O., Valyrakis, M., Greer, K. & Akar, T. 2008 The role of impulse on the initiation of particle movement under turbulent flow conditions. *Science* 322,717–720.

Dwivedi, A., Melville, B. & Shamseldin, A. Y. 2010*a* Hydrodynamic forces generated on a spherical sediment particle during entrainment. *J. Hydraul. Engng* 136 (10), 756–769.

Dwivedi, A., Melville, B., Shamseldin, A. Y. & Guha, T. K. 2010*b* Drag force on a sediment particle from point velocity measurements: A spectral approach. *Water Resour. Res.* 46, W10529.

Einstein, H. A. & El-Samni, E. A. 1949 Hydrodynamic forces on a rough wall. *Rev. Mod. Phys.* 21(3), 520–524.

Gimenez-Curto, L. A. & Corniero, M. A. 2009 Entrainment threshold of cohesionless sediment grains under steady flow of air and water. *Sedimentology* 56(2), 493–509.

Heathershaw A. D. & Thorne P. D. 1985 Sea-bed noises reveal role of turbulent bursting phenomenon in sediment transport by tidal currents. *Nature* 316, 339–342.

Hofland, B. 2005 Rock & roll Turbulence-induced damage to granular bed protections. PhD thesis, TU Delft, available at: www.library.tudelft.nl

Hofland, B., Booij, R. & Battjes, J. 2005 Measurement of fluctuating pressures on coarse bed material. *J. Hydr. Engrg* 131(9), 770–781.

Hofland, B. & Battjes, J. 2006 Probability density function of instantaneous drag forces and shear stresses on a bed. *J. Hydr. Engrg* 132(11), 1169–1175.

Jackson, R. G. 1976 Sedimentological and fluid-dynamic implications of the turbulent bursting phenomenon in geophysical flows. *J. Fluid Mech.* 77, 531–560

Johansson, A. V., Her, J. Y. & Haritonidis, J. H. 1987 On the generation of high-amplitude wall-pressure peaks in turbulent boundary layers and spots. *J. Fluid Mech.*175, 119–142.

Kalinske, A.A. 1947 Movement of sediment as bed load in rivers. *Trans. Am. Geophys. Union* 28(4), 615–620.

Keshavarzi, A. R. & Gheisi, A. R. 2006 Stochastic nature of three dimensional bursting events and sediment entrainment in vortex chamber. *Stoch. Env. Res. Risk A.* 21(1), 75–87.

Kirchner, J. W., Dietrich, W. E., Iseya, F. & Ikeda, H. 1990 The variability of critical shear stress, friction angle, and grain protrusion in water-worked sediments. *Sedimentology* 37, 647–672.

Laadhari, F., Morel, R. & Alcaraz, E. 1994 Combined visualisation and measurements in transitional boundary layers. *Eur. J. Mech., B-Fluids* 13(4), 473–489.

Ling, C.H. 1995 Criteria for incipient motion of spherical sediment particles. *J. Hydr. Engrg* 121(6), 472–478.

Nelson, J. M., Shreve, R. L., MacLean, S. R. & Drake, T. G. 1995 Role of near-bed turbulence structure in bed load transport and bed form mechanics. *Water Resour. Res.* 31(8), 2071–2086.

Nezu, I. & Nakagawa, H. 1993*Turbulence in open channel flows*. IAHR Monograph, Balkema, Rotterdam

Paintal, A. S. 1971 Concept of critical shear stress in loose boundary open channels. *J. Hydr. Eng. Div.* ASCE 9, 91–114.

Papanicolaou, A. N., Diplas, P., Evaggelopoulos, N. & Fotopoulos, S. 2002 Stochastic incipient motion criterion for spheres under various bed packing conditions. *J. Hydr. Engrg* 128(4), 369–380.

Paiement-Paradis, G., Marquis, G. & Roy, A. 2010 Effects of turbulence on the transport of individual particles as bedload in a gravel-bed river. *Earth Surf. Proc. Land.* 36, 107–116.

van Radecke, H. & Schulz-DuBois, E. O. 1988 Linear response of fluctuating forces to turbulent velocity components. In *Proceedings of the Fourth International Symposium on Applications of Laser-Doppler Anemometry to Fluid Mechanics* (ed. R. J. Adrian), pp. 23–44. Lisbon, Portugal, Springer.

Radspinner, R., Diplas, P., Lightbody, A., & Sotiropoulos, F. 2010. River Training and Ecological Enhancement Using In-Stream Structures. *J. Hydraul. Eng.* 136(12), 967–980.

Robinson, S. K. 1991 Coherent motions in the turbulent boundary layer. *Annu. Rev. Fluid Mech.* 22, 631–639.

Sarkar, S. & Sarkar, S. 2010 Vortex dynamics of a cylinder wake in proximity to a wall. *J. Fluid Struct.* 26(1), 19–40.

Schmeeckle, M. W. & Nelson, J. M. 2003 Direct numerical simulation of bedload transport using a local dynamic boundary condition. *Sedimentology* 50, 279–301.

Schmeeckle, M. W., Nelson, J. M. & Shreve, R. L. 2007 Forces on stationary particles in near-bed turbulent flows. *J. Geophys. Res.* 112, F02003.

Shvidchenko, A. B. & Pender, G. 2001 Macroturbulent structure of open-channel flow over gravel beds. *Water Resour. Res.* 37 (3), 709–719.

Smart G. M. & Habersack H. M. 2007 Pressure fluctuations and gravel entrainment in rivers. *J. Hydraul. Res.* 45(5), 661–673.

Song, T., Graf, W.H. & Lemmin, U. 1994 Uniform flow in open channels with movable gravel bed. *J. Hydraul. Res.* 32(6), 861–876.

Stoesser, T., Fröhlich, J. & Rodi W. 2007 Turbulent open-channel flow over a permeable bed" in *Proceedings of 32nd IAHR Congress*, Venice, Itoaly.

Sumer, B.M., Chua, L.H.C., Cheng, N.S. & Fredsoe, J. 2003 Influence of turbulence on bed load sediment transport. *J. Hydr. Engrg.* 129(8), 585–596.

Sumer B. M. & Fredsoe E. J. 2006 *Hydrodynamics Around Cylindrical Structures.* World Scientific, Singapore.

Sutherland, A. J. 1967 Proposed mechanism for sediment entrainment by turbulent flows. *J. Geophys. Res.* 72 (24), 6183–6194.

Valyrakis, M, Diplas, P., Dancey, C. L., Greer, K. & Celik, A.O. 2010 The role of instantaneous force magnitude and duration on particle entrainment. *J. Geophys. Res.* 115, 1–18.

Vollmer, S. & Kleinhans, M. G. 2007 Predicting incipient motion, including the effect of turbulent pressure fluctuations in the bed. *Water Resour. Res.* 43, W05410

Wang, J. 1999 Hydrodynamic lift and drag fluctuations of a sphere. PhD thesis, The Pennsylvania State University.

Williamson, C. H. K. 1996 Vortex dynamics in the cylinder wake. *Annu. Rev. Fluid Mech.* 28, 477–539.

Yoshida, A., Tamura Y. & Kurita, T. 2001 Effects of bends in a tubing system for pressure measurement. *J. Wind Eng. Ind. Aerodyn.* 89 (20), 1701–1716.

Zeng, L., Balachandar, S., Fischer, P. & Najjar, F. 2008 Interactions of a stationary finite-sized particle with wall turbulence. *J. Fluid Mech.* 594, 271–305,

Chapter 5. Instantaneous Turbulent Forces and Impulse on a Rough Bed: Implications for Initiation of Bed Material Movement

Abstract

The aim of this study is to investigate the features of impulsive flow events and their potential to dislodge bed material under uniform and cylinder wake flows. This was pursued by analyzing the surface pressures and entrainment of a spherical grain, as well as the near bed flow velocity under various flow conditions. A simplified bed geometry consisting of spherical particles was used in the flume experiments to reduce the complexities associated with the variations in the bed and flow details in an effort to identify the underlying dominant physical mechanism. The hydrodynamic forces approximated directly from the measured pressures acting on the test grain and indirectly from the near bed velocity were used to detect the impulse events and explore their statistical distribution. The connection between the near bed bursting phenomenon and the impulse events was discussed. The influence of lift force during impulsive events and the turbulence intensity on the particle entrainment was examined.

1. Introduction

The common perception in sediment research concerning sediment transport, especially near threshold conditions, is that the fluctuating drag and lift forces acting on individual grains due to turbulent flow are responsible for particle entrainment. Force or moment balances have been utilized using the magnitude of fluctuating forces to establish the condition for threshold of movement in deterministic and probabilistic models (Papanicolaou et al., 2002; Wu and Chou, 2003; Smart and Habersack, 2007 among

others). According to these force-magnitude based approaches, extreme flow events near the bed exerting high forces (above a critical value) on individual grains will always cause particle entrainment. However, as shown by Balakrishnan (1997) and recently by Diplas et al. 2008, high-magnitude turbulent flow events occurring immediately upstream of a grain are typically very short-lived, which cause them to be ineffective for completely dislodging the grain from its initial position, even when they are well above a given critical value. On the contrary, turbulent events of not as high magnitude (still above a critical minimum value) but lasting longer were observed to be able to fully dislodge the grain from its pocket. These findings, which were obtained from direct observations of threshold of movement of a test grain, together with synchronously measured near bed flow velocity, suggest that the magnitude of fluctuating forces acting on individual grains, even its extreme values, is insufficient for predicting the initiation of movement and therefore characterizing threshold conditions. In addition to the force magnitude, what also needs to be considered is the duration over which the force acts. Thus, impulse, which accounts for both the magnitude and duration of force application (impulse duration, T), was proposed and validated under well controlled laboratory conditions to be the parameter suitable for determining the threshold of particle movement (Diplas et al. 2008).

Celik et al. (2010) showed that the bed particle entrainment rate at low mobility conditions is extremely sensitive to the minute changes in flow parameters, such as the bed shear stress for the bed of spherical particles under uniform flow conditions. A considerable change in sediment movement rate was observed not only as a result of such modifications of uniform flow conditions but for unsteady flow conditions as well.

Nelson et al. (1995) and Sumer et al. (2003) reported such results, where the turbulence intensity, TI, of the flow field was increased using various methods.

Although recent findings illuminate the mechanism of particle entrainment due to turbulent flow processes, they are based on observations of particle movements and indirect estimates of instantaneous forces based on near bed velocity measurements. Accurate data on forces/pressures acting on rough walls with synchronous near bed flow velocity data is still lacking, with the exception of recent noteworthy efforts from Hofland et al. (2005), Schmeeckle et al. (2007), Detert et al. (2010), and Dwivedi et al. (2010). These recent force/pressure measurements highlight the significance of sweep type of events near the bed on high drag forces accompanied by upward lift force. On the other hand, incipient motion models using the impulse concept requires better understanding of the uncertainties in estimating instantaneous drag forces (i.e. the variation in the instantaneous drag coefficient values, Schmeeckle et al., 2007), the role of lift force, and the turbulence intensity on particle dislodgement. One obvious need is to measure the forces, the near bed flow velocity and the particle entrainment rate under identical bed and flow conditions.

The aim of this study is to investigate the force magnitudes, force durations and impulse magnitudes of the peak events obtained from direct measurements of pressures acting on a spherical particle. Entrainment rate of a mobile test grain was also measured under identical flow conditions. Experimental results are discussed in the context of incipient motion.

The experimental methods are described in the following section. The detection of impulses is explained in Sec. 3. In the results section (Secs.4.1 and 4.2) we present the

features of impulse and its relations to forces and flow velocity. Implications of our findings to sediment movement under both uniform and unsteady wake flow conditions are also discussed in Sec.4.3. Conclusions are given in Sec. 5.

2. Experiments

In this study we used the simultaneously measured near bed flow velocity - surface pressure data of Celik et al. (in preparation) and the simultaneously measured near bed velocity - particle entrainment data from mobile grain experiments of Celik et al. (2010) to examine the particle entrainment mechanism. The configuration of flume test section used in both experiments were identical and consisted of a 12.7 mm diameter, d, spherical grain resting on two layers of well packed identical spheres as shown in Fig. 1. This simplified bed geometry was preferred to reduce the complexities associated with the variations in the bed and flow details in an effort to identify the underlying dominant physical mechanism. The majority of the flume tests were performed in fully developed uniform open channel flow at near threshold conditions for a range of particle Reynolds numbers ($Re^* = u^* d/\nu$, where u^* is the friction velocity and ν is the kinematic viscosity). In addition, similar pressure and particle entrainment experiments were performed in the wake of a cylinder (see Fig. 2*b* for cylinder wake test configuration).

In the mobile particle experiments, entrainment of a mobile, Teflon® grain was recorded utilizing a separate laser-based system that detects its displacement (Diplas et al. 2010). A spherical particle, identical in size to the mobile grain, was instrumented with low-range pressure transducers and it was securely attached to the flume bed, to measure

the instantaneous surface pressures simultaneously at its front (p_1), back (p_2), top (p_3) and bottom (p_4) as shown in Fig. 1*a*.

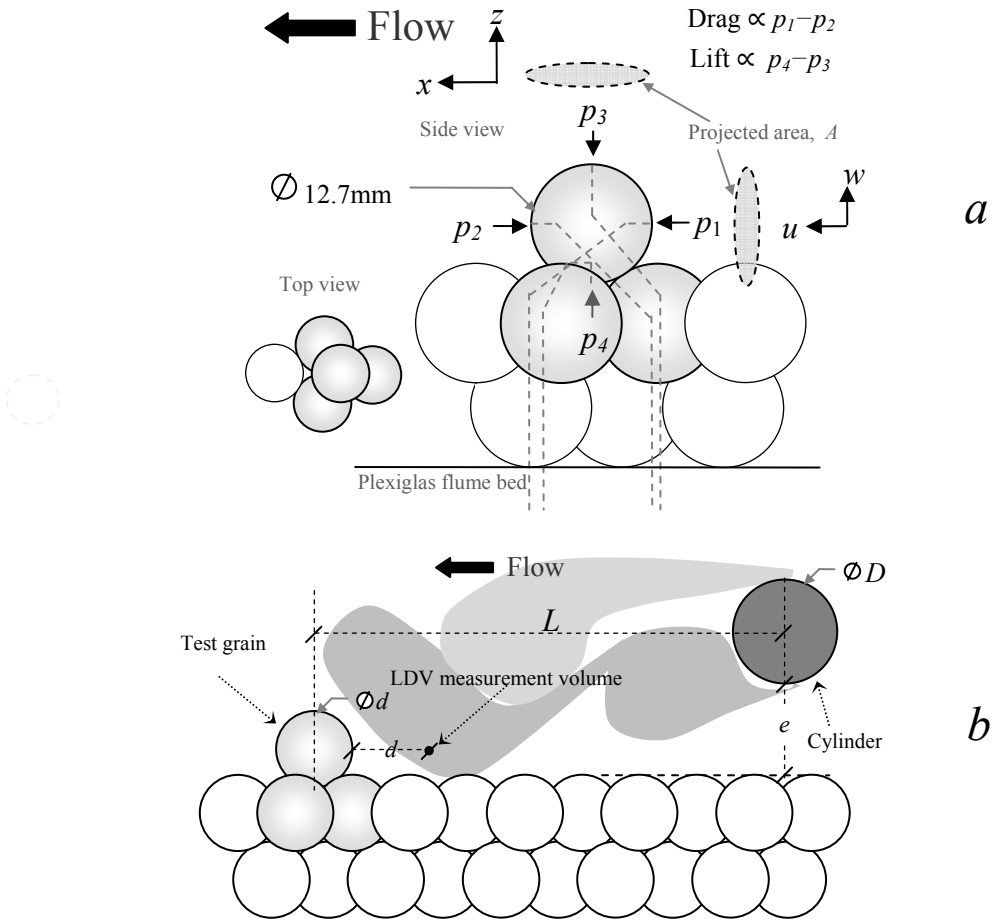

Figure 1. Bed configuration of mobile and instrumented particle experiments. a) Definition sketch for the pressure measurement points and bed geometry. b) Side view of the test section with the test particle in the wake of a cylinder.

In the pressure and particle entrainment experiments, mobile and instrumented grains were placed on the centerline of the flume bed. The instantaneous near bed velocity components, *u* and *w*, in the streamwise and vertical directions respectively,

were measured one particle diameter upstream of the mobile/instrumented grain along its centerline via the use of a 2D laser Doppler velocimeter (LDV- for more details, see Celik et al. 2010). Sampling duration for each flow condition in all experiments was 15 minutes. A Cartesian coordinate system (x, y, z) where x is streamwise along the flume axis, y is spanwise across the flume, and z is perpendicular to the flume bottom was adopted in this study.

The wake flow downstream of a bluff body is characterized by higher turbulence intensities and larger pressure fluctuations acting on the wall. In many practical river engineering applications, flow is altered due to presence of bedforms and hydraulic structures. These conditions lead to a significant increase in sediment movement and result in scour near these hydraulic structures in rivers and waterways (Sumer et al. 2003, Radspinner et al. 2010). Celik et al. (in preparation) showed that the mean lift forces acting on the spherical grain were higher in magnitude and acting upward. The purpose of the tests considered here was to examine the way in which the presence of a cylinder and accompanied high upward lift force might influence the entrainment rate of a mobile grain in such unsteady wake flows.

Four different size PVC pipes with diameters (D) of 3.34, 2.67, 2.19 and 1.27 cm, placed horizontally and extending across the flume width upstream of the test section were used. Figure 1*b* illustrates the bed conditions with the cylinder. L and e in Fig.1*b* are the distance between the center of the instrumented test grain and centerline of the cylinder in streamwise direction, and the distance between the bed (top of the spheres in the uppermost layer) and the bottom of the cylinder respectively. L was chosen to be $2.5D + 1.5d$, as this location was where the highest turbulence intensity (obtained from

near bed velocity measurements) was observed in preliminary flume tests. e was set equal to D, so that $e/D = 1$ to avoid suppression of the vortex shedding due to rough bed proximity (Sumer and Fredsøe, 2006).

A summary of the flow conditions for the flume tests is given in Table 1. A total of ten uniform flow conditions were tested. The uniform flow experiment designated UC was used with the 4 different diameter cylinders. The pressure and entrainment experiments were performed for U2-U8, UC and CD1-CD4.

Table 1. Summary of the flow conditions.

Run	**Depth average velocity, U (cm/s)**	**Flow depth, h (cm)**	***Re****	**Pressure measurements**	**TI**	**Particle Entrainment experiments**	**Particle Entrainment Frequency, n_e** (Ent./min)
U1	47	8.1	438	Yes	0.28	No	-
U2	45	7.5	424	Yes	0.27	Yes	6.93
U3	43	8.2	413	Yes	0.27	Yes	5.73
U4	41	7.9	398	Yes	0.27	Yes	2.06
U5	42	8.3	385	Yes	0.27	Yes	1.33
U6	40	8.6	377	Yes	0.26	Yes	0.52
U7	41	9.1	372	Yes	0.26	Yes	0.24
U8	39	8.7	364	Yes	0.27	Yes	0.14
U9	35	8.9	330	Yes	0.26	No	-
UC	43	9.0	399	Yes	0.27	Yes	4.2
	Cylinder diameter (cm)						
CD1	3.34			Yes	0.36	Yes	19.8
CD2	2.67			Yes	0.41	Yes	22
CD3	2.19			Yes	0.43	Yes	25.4
CD4	1.27			Yes	0.31	Yes	6.6

3. Impulse Detection

The magnitudes of the instantaneous forces were estimated from the measured instantaneous pressures by $F_D = A(p_1 - p_2)$ and $F_L = A(p_4 - p_3)$, where F_D is the drag force, F_L is the lift force and A is the projected area of the spherical test grain in both horizontal

and vertical planes (Einstein and El Samni, 1949; Hofland et al., 2005; see the definition sketch and the insets in Fig. 1*a*). For the analysis here after, we consider F_L as the effective lift force which excludes the buoyancy force acting on the submerged 12.7 mm diameter grain.The procedure to detect the impulse events is explained below.

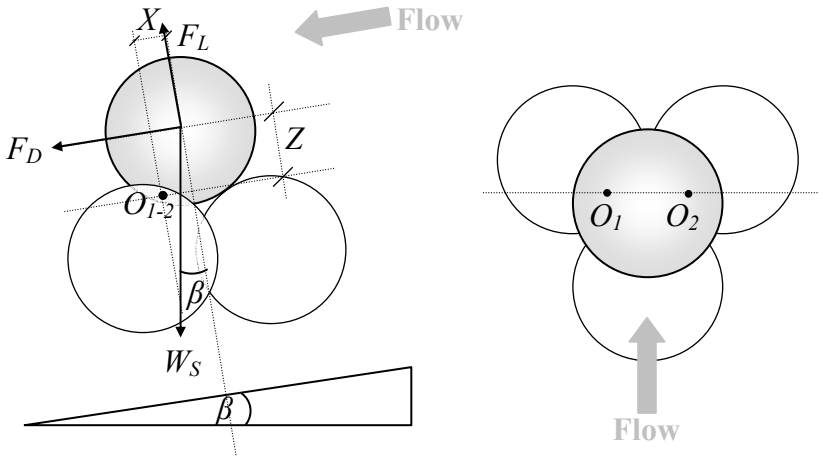

Figure 2. Definition sketch of the forces acting on a spherical particle resting on identical size densely packed spheres, side view (left) and top view (right) of the bed geometry. This is the arrangement that was used for both the pressure and the particle entrainment measurements.

The forces acting on the mobile particle for the given grain configuration (Fig.2) are submerged particle weight, W_S, F_D and F_L, all assumed to act through the center of gravity of the sphere (White, 1940; Gessler, 1971). The test grain is highly exposed to the flow and the drag force, F_D, is the prevailing hydrodynamic force component and the preferred mode of particle entrainment is rolling for these conditions (Sutherland, 1967; Fenton and Abbot, 1977; Diplas *et al*. 2008). Turbulence fluctuations in the F_D time

series which are above the minimum drag force necessary for particle movement, F_{Dcr} are treated as impulses. F_{Dcr} can be obtained from:

$$F_{Dcr} = \frac{X}{Z}(f_v W_s \cos(\beta) - F_{L\text{mean}}) - f_v W_s \sin(\beta) \quad (1)$$

where f_V is the hydrodynamic mass coefficient (Papanicolaou et al., 2002), $f_V = (1+0.5(\rho/\rho_S - \rho))$, ρ_S is the density of the Teflon particle, ρ is the density of water, X and Z are the lever arms obtained from the bed geometry, aligned with the bed and normal to the bed respectively, and β is the angle between the channel bed and the horizontal plane. Though it is generally assumed that the drag dominates grain dislodgement for highly exposed particles, the time-averaged lift force over the entire sampling duration, $F_{L\text{mean}}$, is also considered in Eq. 1 in the framework of effective particle weight, as previously proposed by Zanke (2003).

From the time history of drag force acting upon a particle $F_D(t)$, the impulse, I, can be calculated as follows:

$$I = \int_{t_1}^{t_2} F_D(t)dt = < F_D > T \text{ with } F_D(t) \geq F_{Dcr} \text{ between } t_1 \text{ and } t_2 \quad (2)$$

where, $T = t_2 - t_1$ is the duration of the applied force, $<F_D>$ is the time-average drag force over duration T (angle brackets denote time averaging over T). The duration over which $F_D \geq F_{D\,\text{cr}}$ during the i^{th} event, T_i, is shown in Fig 3 (top plot). The time-average F_D value, $<F_D>_i$, representative of the average drag force of the i^{th} event with $F_D \geq F_{D\,\text{cr}}$ and impulse magnitude, $I_i = <F_D>_i T_i$, can be determined from the data series in post-processing. In addition, time-average F_L value, $<F_L>_i$, representative of the average lift force acting on the grain for the period of T_i of the i^{th} event can be computed for all events (Fig.3, second from top). Simultaneously measured near bed flow velocity components u and w are also shown in Fig. 3. In order to account for the phase delay between the flow

velocity and force signals due to the distance between the grain and the location of the LDV measurement volume, the flow velocity records were shifted forward by the lag time obtained at the rise point in the cross correlation function between u and p_1 (Celik et al. in preparation).

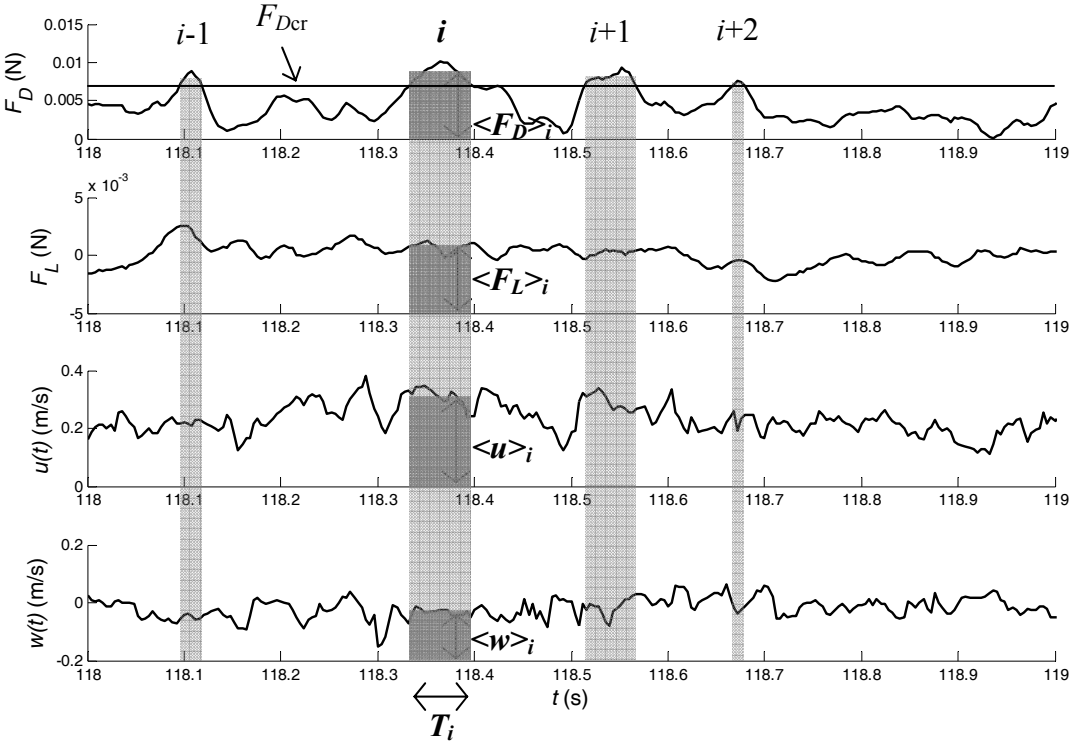

Figure 3. Synchronized plot of measured forces acting on the test grain and flow velocities measured one diameter upstream of the grain. From top to bottom: Representative time series of F_D, F_L, u, and w from run U3. Shaded vertical regions indicate events within F_D, F_L, u, and w time series during which $F_D \geq F_{D\,\mathrm{cr}}$. The i^{th} event was selected to show the magnitude of $< F_D >_i$, $< F_L >_i$, $<u>_i$, and $<w>_i$.

In this way, the near bed flow events and the forces they generate on the particle were matched in time before the impulse analysis was performed. The procedure described

here was implemented and the series of random impulse events (and associated I, T, $\langle F_D \rangle$, $\langle F_L \rangle$, $\langle u \rangle$, and $\langle w \rangle$) for each run were detected. The following section elaborates on the properties of the directly detected impulses and their relation to the flow parameters.

4. Results

4.1 Distribution of Directly Detected Impulse

The histograms of duration and impulse obtained from the measured pressures acting on the test grain are both positively skewed with a long tail (Figs. 4a-b respectively). These histograms are representative of all uniform flow test cases.

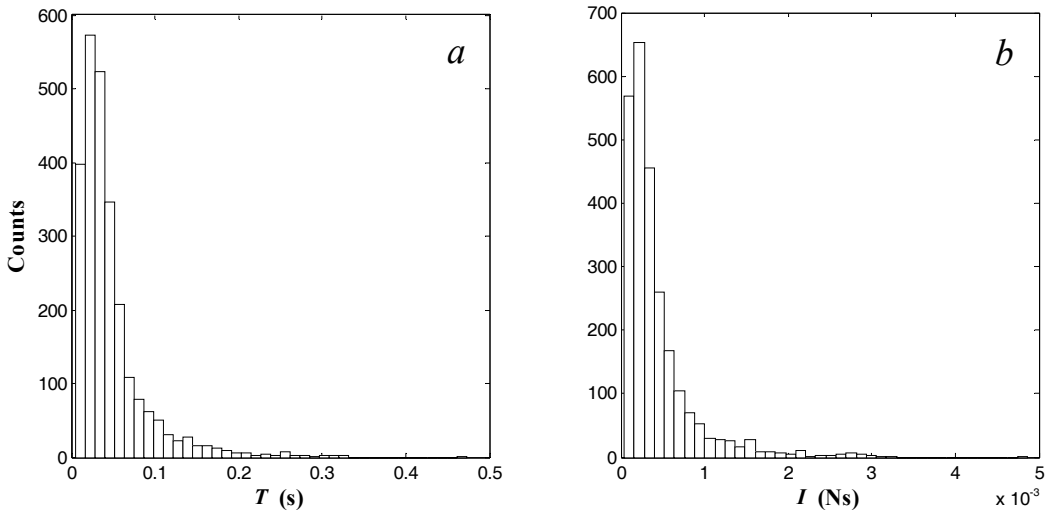

Figure 4. Histograms of the event duration (*a*) and impulse (*b*). Data from Run U2 presented.

Impulse obtained indirectly from $u^2(t)$ ($\sim F_D(t)$) time series was described by a log-normal distribution by Celik et al. (2010). If the impulse, I, is non-dimensionalized with its ensemble average value, $\hat{I} = I / I_{mean}$, then the log-normal probability density function for the dimensionless impulse, $\hat{I}$ as a function of the impulse intensity (coefficient of variation of impulse), $\delta = I_{std} / I_{mean}$ is given by

$$f(\hat{I}) = \frac{1}{\sqrt{2\pi \ln(1+\delta^2)}\hat{I}} \exp\left[-\frac{\left(\ln \hat{I} + \ln\sqrt{1+\delta^2}\right)^2}{2\ln(1+\delta^2)} \right] \tag{3}$$

Here the probability density function (pdf) of directly measured impulses from F_D time series are compared with Eq. 3 in Figs. 5, 6 and 7 for the runs U2, U3 and CD1 respectively. δ values in Eq. 3 were determined from the data for each particular run. In Fig. 5, the pdf of impulse magnitudes determined from approximated drag force time history ($\sim u^2$) is also included with $C_D = 0.9$ and the effect of time-averaged lift force taken in to account. It can be seen that the pdf given by Eq. 3 describes the directly detected impulse data well. However, whether the impulse values are detected directly from the measured drag force or indirectly from the flow velocity makes a difference in the number of data points near the rising leg of the pdf. Impulse events in the rising legs of the pdfs consist of combinations of very short T and very high F_D values, or vice versa. Not all of these events were identified in the instantaneous drag force time history approximated from the near bed velocity. Therefore, this region was not characterized well with Eq.3 (Fig. 5). It is however clear that there are very low amplitude impulse events captured in the actual force time series. Nevertheless, given the agreement between Eq. 3 and the normalized histograms from the measurements, we validate the probability density function of dimensionless impulse in both steady (Figs. 5-6) and

unsteady flow conditions (Fig. 7) using impulses detected from direct pressure measurements.

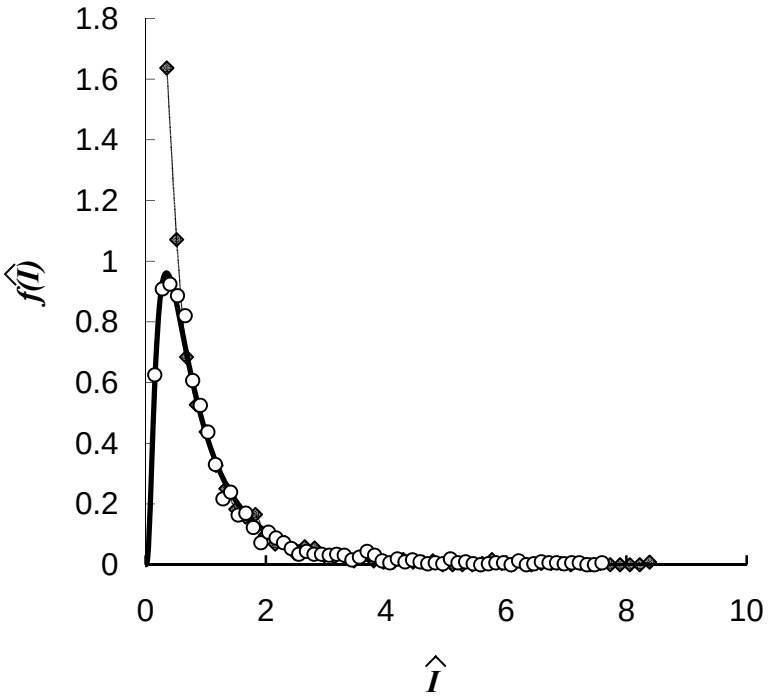

Figure 5. Comparison of Eq. 3 with measured pdfs for run U2. Solid lines are used to show pdfs obtained from Eq. 3 and circles from data. δ = 1.01 from the direct measurements (open circles) and δ = 0.96 from force estimations using C_D=0.9 in Eq. 3 with the effect of time-averaged lift included in Eq. 1 (solid diamonds). p-value = 0.53.

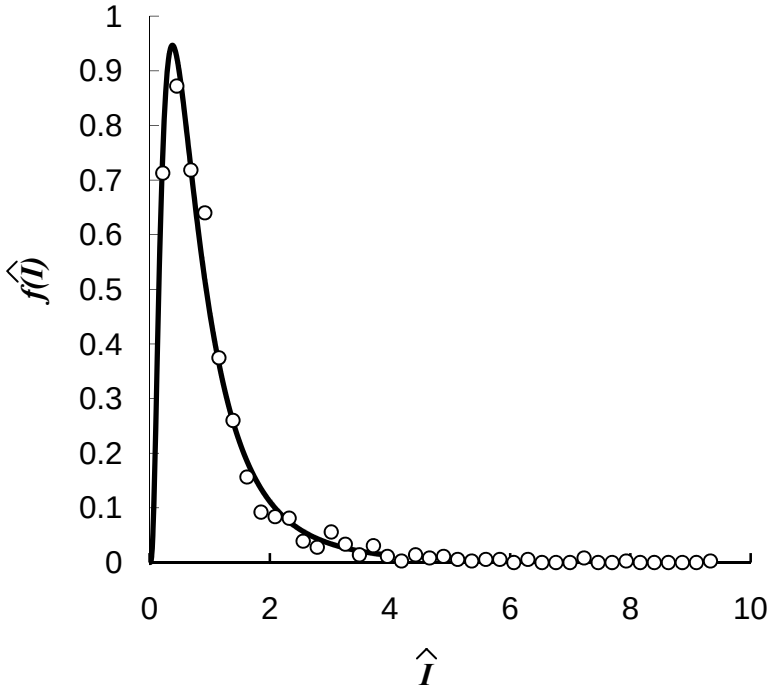

Figure 6. Comparison of Eq. 3 with measured pdfs for run U3. Solid line is used to show pdf obtained from Eq. 3and open circles from data. $\delta = 0.95$. p-value = 0.65.

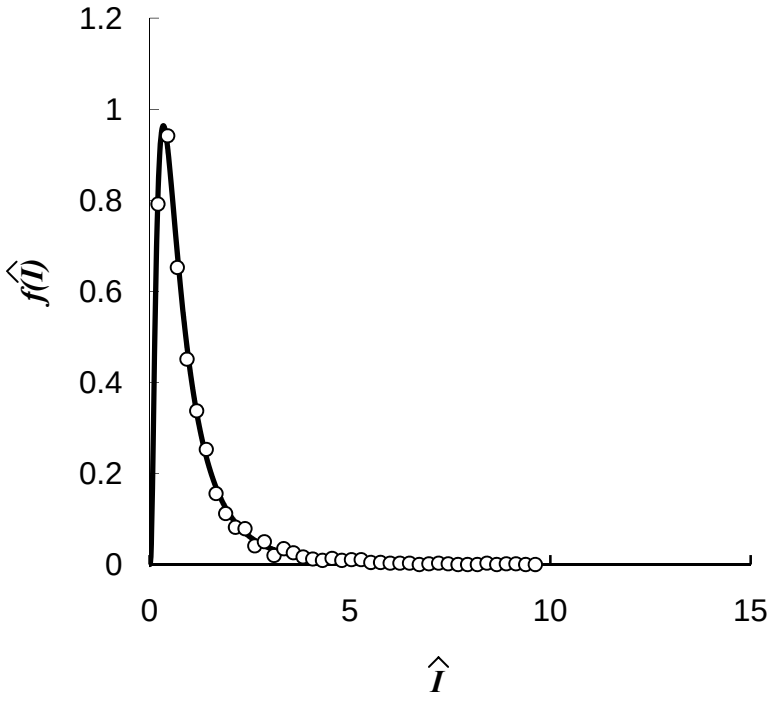

Figure 7. Comparison of Eq. 3 with measured pdfs for run CD1 (cylinder). Solid line is used to show pdf obtained from Eq. 3 and open circles from data. $\delta = 1.02$. p-value = 0.56.

4.2 Forces during Impulse Events

Even though impulse rather than force magnitude is the germane parameter for particle dislodgement, here we investigate the relation between force magnitudes and the near bed flow velocities occurring for the periods of impulse events.

Ensemble Average of the Forces of Impulse Events

The variations in the ensemble average (indicated also by the subscript "mean") of $<F_D>$ and $<F_L>$ with Re^* are shown in Fig. 8. $<F_D>_{\text{mean}}$ was non-dimensionalized by $F_{D\text{cr}}$ (Eq.

1) and $<F_L>_{mean}$ by the submerged weight, W_s, of the Teflon® ball. As the flow strength increases within the given Re^* range, there is a drop in the $< F_L >_{mean}$ from roughly 5% of the W_s to 1% which is also accompanied by a 7.5% increase in $<F_D>_{mean}$. The former is expected to have a stabilizing effect as the effective particle weight increases by nearly 4% within the given Re^* range. On the other hand, it is well known that minute adjustments in flow or local bed conditions result in considerable changes in the particle entrainment rates especially near threshold flow conditions. Celik et al. (2010) showed for instance, within the same Re^* range as studied in this work, that a 14% increase in Re^* is accompanied by a nearly 50-fold increase in the entrainment rate of a Teflon ball. Variations in the ensemble average forces (associated with impulse events) are also not indicative of such considerable changes in the particle entrainment rates. Therefore methods employing time (or ensemble) average forces are not adequate to describe the particle entrainment due to turbulent flow processes accurately.

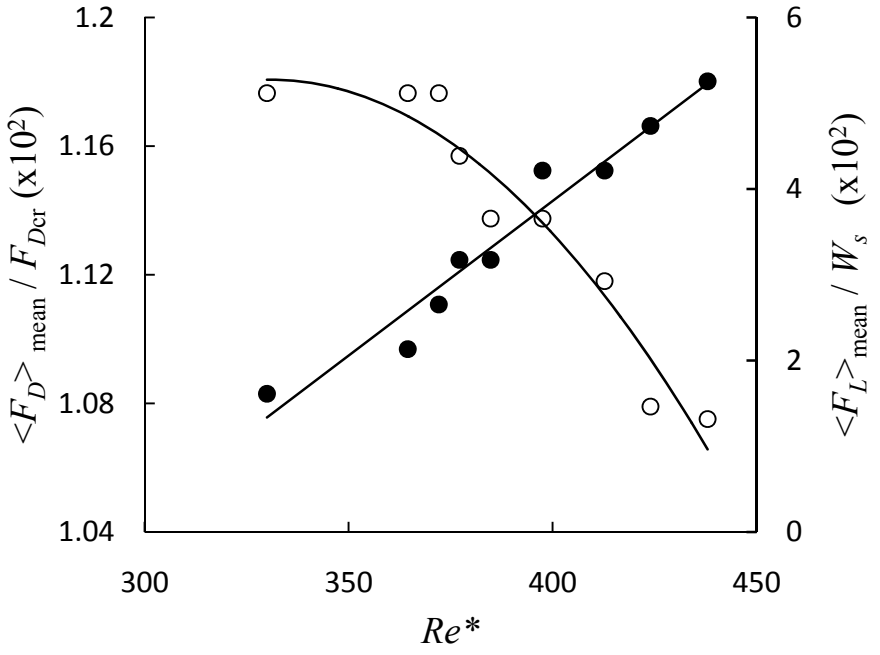

Figure 8. Variations in the non-dimensionalized $<F_D>_{mean}$ and $<F_L>_{mean}$ (right axis) with Re^*. Linear and polynomial curves were included for visual guidance only.

Drag Coefficients of Impulse Events

Schmeeckle et al. (2007) showed that the instantaneous drag coefficient values (denoted by C_D from here on) vary considerably. In chapter 4, it was argued that the instantaneous u^2 is correlated with the pressures in the front and back of the particle at different time lags, which might be causing this variation. On the other hand, the average C_D values we obtained are consistent with those reported by Schmeeckle et al. (2007) (See Fig. 9 for the C_{Dmean} vs Re^*). The instantaneous drag coefficient values averaged over a turbulent event, $< C_D >_i$, are relevant for the impulse framework. The drag coefficient of an (i^{th}) impulse event is given by:

$$< C_D >_i = \frac{2<F_D>_i}{\rho A <u>^2_i} \quad (4)$$

Here, $\langle u \rangle_i$ was determined in a similar fashion as $\langle F_L \rangle$ as shown in Fig.3 (third figure from top), representing the u averaged over the impulse duration T_i. Figure 9 shows the variation in the ensemble average $\langle C_D \rangle$, $\langle C_D \rangle_{\text{mean}}$ with Re^*. Although there is a very strong linear relationship between the $\langle C_D \rangle_{\text{mean}}$ and Re^*, individual $\langle C_D \rangle_i$ values vary more than an order of magnitude within each run. The histogram of $\langle C_D \rangle$ from run U2 plotted in Fig. 10 shows this variability. The relationship between the $\langle u \rangle_{\text{i}}$ and $\langle C_D \rangle_{\text{i}}$ values is shown in Fig. 11 where the $\langle u \rangle_{\text{i}}$ values are non-dimensionalized with the ensemble average $\langle u \rangle$, $\langle u \rangle_{\text{mean}}$. Data points (from four different runs) scatter around a hyperbola, the equation of which is given as an inset in Fig. 11. The $\langle C_D \rangle_{\text{i}}$ varies in a nonlinear fashion and is inversely related to $\langle u \rangle_{\text{i}}$. This behavior is consistent with that presented by Schmeeckle et al. (2007). The range of $\langle C_D \rangle_{\text{i}}$ values for a given $\langle u \rangle_{\text{i}}$ gets smaller for flows of lower strength. The equation of the best fit curve in Fig. 11 is $\langle C_D \rangle_{\text{i}} \langle u \rangle^2_i = 1.5 \langle u \rangle^2_{mean}$ indicating a near constant drag force for impulsive events. The vertical error bars shown with the gray shaded region around the hyperbola help quantify the scatter around this constant value. In the view of that, $\langle F_D \rangle_{\text{i}}$ reaches values as high as 50% of the mean drag force of impulsive events, particularly at high $\langle u \rangle_{\text{i}}$ values of higher flow strengths. There are flow events with low near bed velocities resulting in high magnitude forces imparted on the grain ($\langle u \rangle_i / \langle u \rangle_{\text{mean}} < 0.75$). If only the near bed velocity is used together with a constant C_D value to predict the drag force (and resulting particle movement), then these low velocity events will not be considered as events with potential to dislodge the grain because their force magnitudes will be significantly underestimated. In addition, for events with high velocities ($\langle u \rangle_i / \langle u \rangle_{\text{mean}} >$

1.25), $<C_D>_i$ values are typically below the average C_D. Therefore a constant drag coefficient will cause overestimation of the force magnitude for high flow velocities.

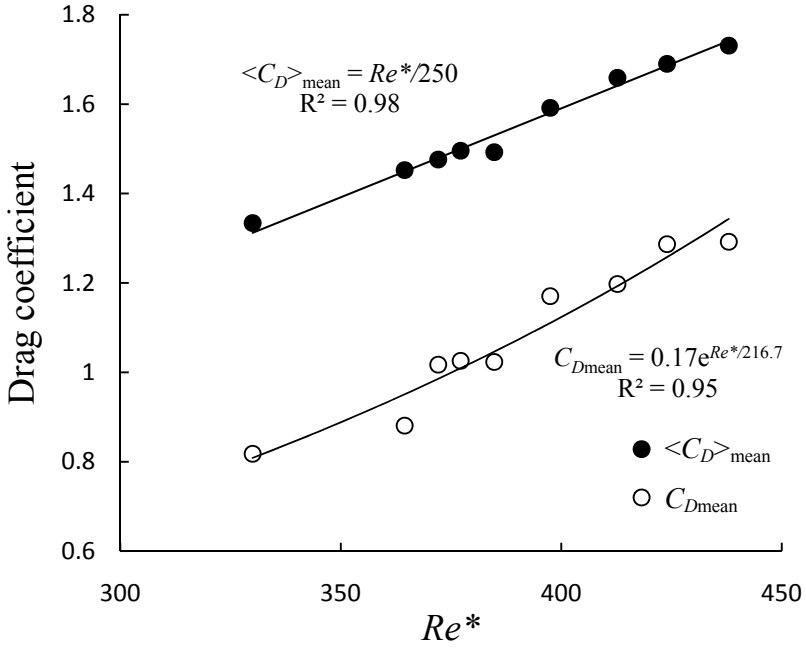

Figure 9. Plot of the average drag coefficients vs. Re^*.

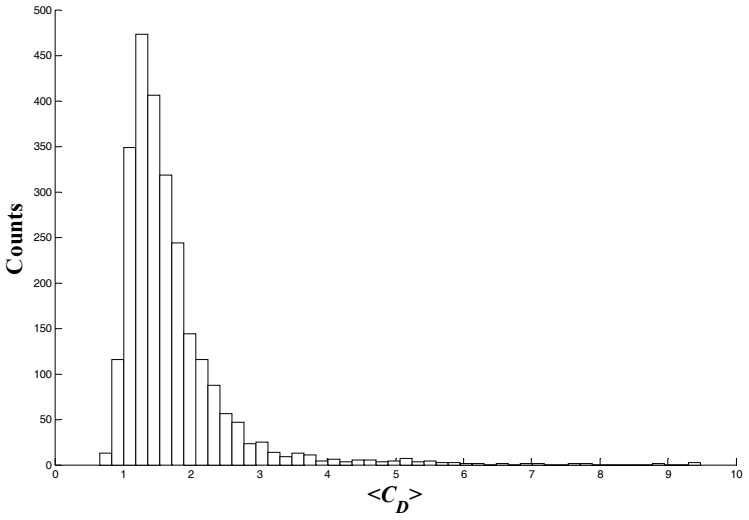

Figure 10. Histogram of the $<C_D>$, 2522 data points from Run U2 were used.

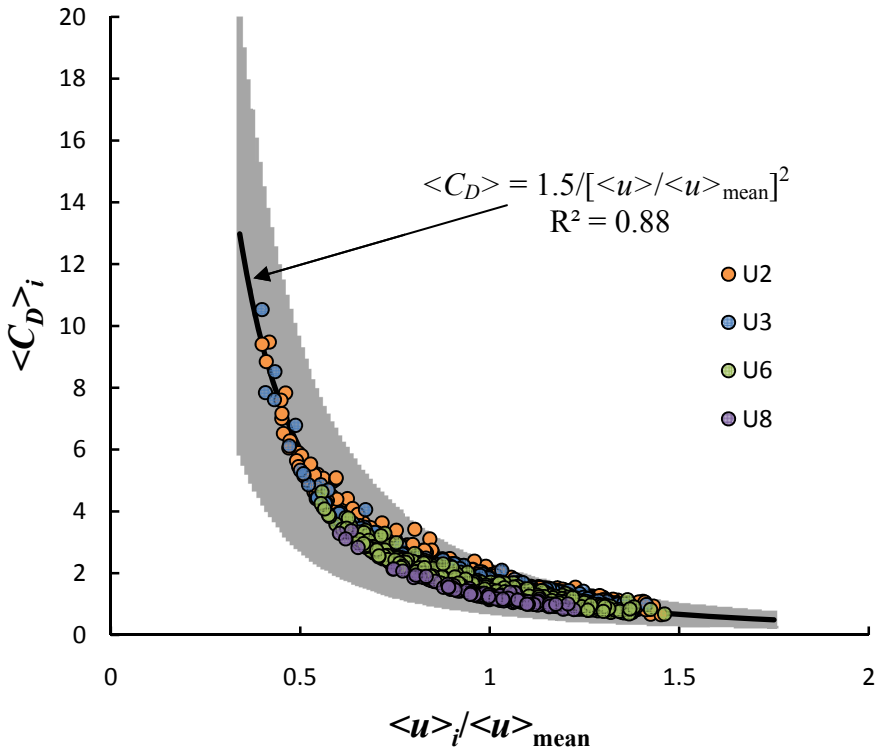

Figure 11. Scatted plot of $<C_D>_i$. vs non-dimensionalized $<u>_i$. Shaded gray region represents ±50 error around the best fit curve.

These observations are in overall agreement with the findings of Schmeeckle et al. (2007). However, the strength of the extreme flow events near the bed, considering their strong correlation with particle movement is better characterized by their impulse magnitude, I_i. Therefore it is important to see the coupling of $<u>_i$ - $<C_D>_i$ pairs with the I_i values. This is shown in Fig. 12 with a 3D surface plot of $<u>_i$, $<C_D>_i$ and I_i (data: run U3). The extreme impulse events are generally observed in the high flow velocity region ($<u>_i$ above $<u>_{mean}$) where the variability in C_D values is small. It implies that the very high $<C_D>_i$ values (>3) observed near the rising leg of the hyperbola in Fig.12 are not associated with impulse events which have potential to dislodge a grain from its pocket. The lift forces of impulse events are not correlated well with the $<C_D>_i$ values as shown

in Fig. 13 though the extreme lift force magnitudes occur at the region of lower $<C_D>_i$ values.

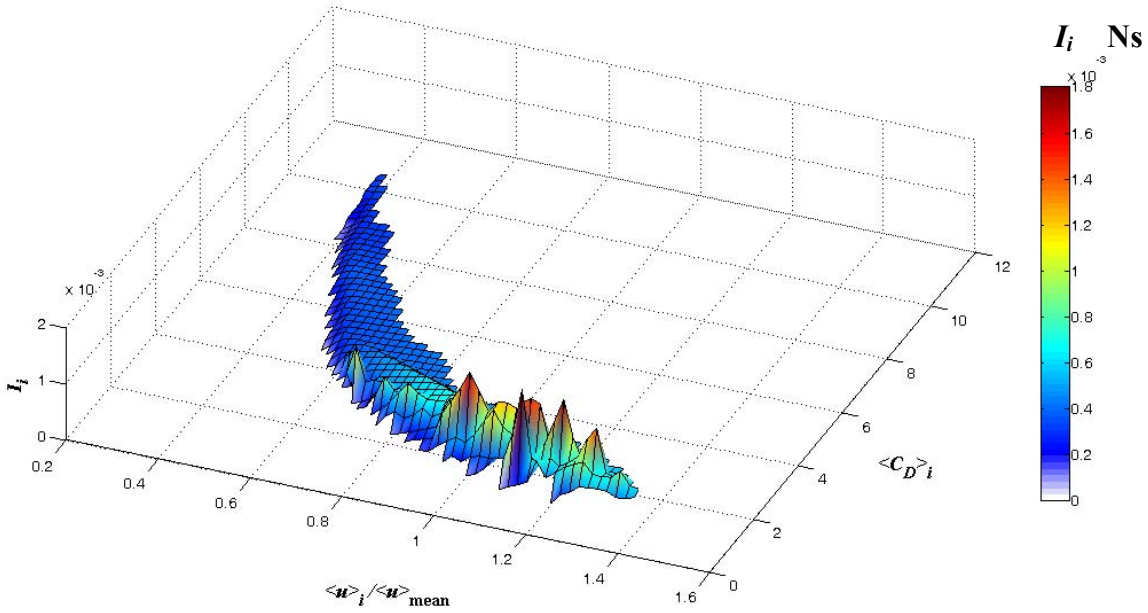

Figure 12. 3D surface plot of $<u>_i$, $<C_D>_i$ and I_i (data: run U3). Color bar indicates the impulse magnitude.

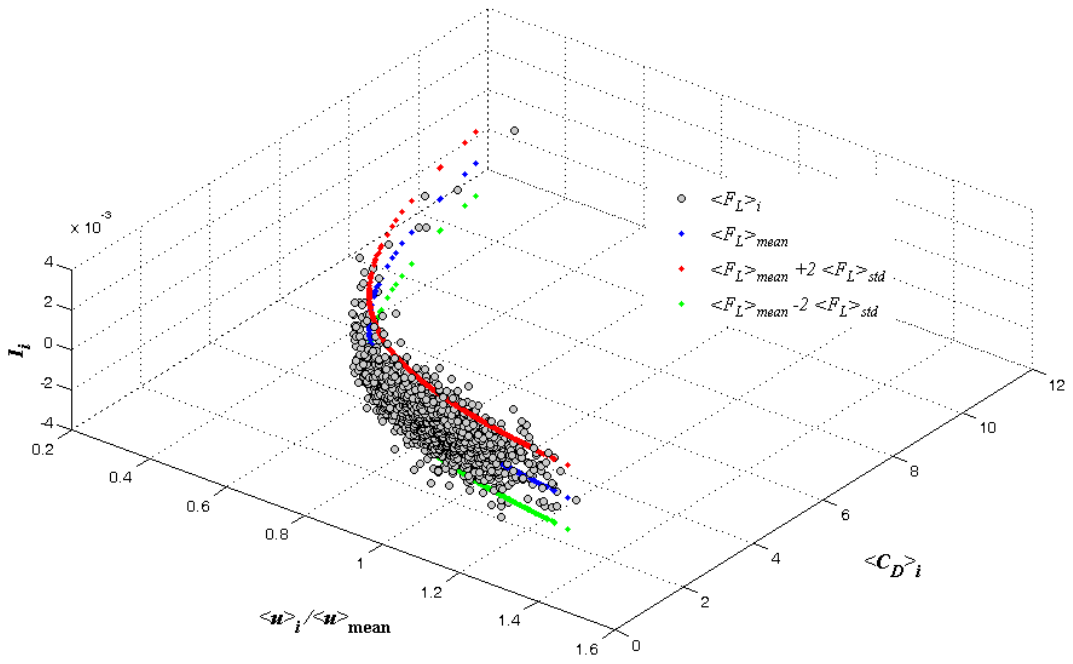

Figure 13. 3D scatter plot of $\langle u \rangle_i$, $\langle C_D \rangle_i$ and $\langle F_L \rangle_i$ (data: run U3). Blue ($\langle F_L \rangle_{\text{mean}}$) red and green lines ($\langle F_L \rangle_{\text{mean}} \pm 2\langle F_L \rangle_{\text{std}}$) are obtained using the equation given in Fig.11 inset.

1D and 2D Histograms of the Forces of Impulse Events

The histograms of the event based force magnitudes are presented in Fig. 14 (Data: Run U2). The histogram of $\langle F_D \rangle$ (non-dimensionalized by $F_{D\text{cr}}$) bears resemblance to a triangular (beta) distribution as shown in Fig. 14*a*. The distribution of $\langle F_L \rangle$ (non-dimensionalized by W_s) is near Gaussian (Fig. 14*b*). The same general distribution characteristics are observed for all runs from uniform flow conditions. As shown in Fig. 14b, $\langle F_L \rangle$ can have values up to ±20% of W_S for this flow condition and values up to ±30% of W_S in other runs. Such extreme lift forces acting upward will contribute to the particle dislodgement while if acting downward, will have a stabilizing effect. It is

evident that the lift force (concurrent with impulse events) can, however rarely, be consequential for particle stability even for a fully exposed particle configuration.

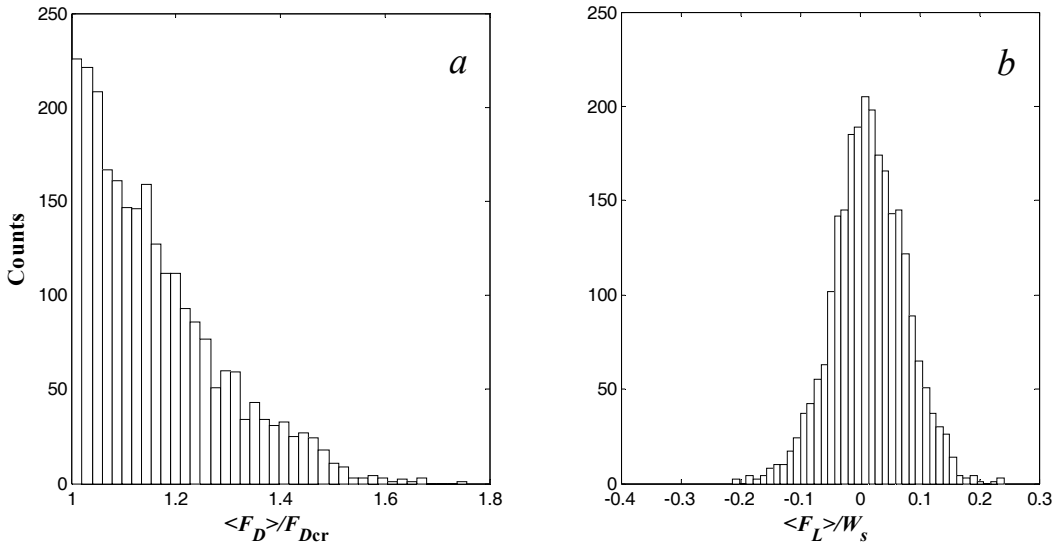

Figure 14. Histograms of the event average drag force (a) and lift force (b). Data from Run U2 presented.

The joint (2D) histograms of $<F_D>$ with $<F_L>$ and I with $<F_L>$ are shown in Figs. 15*a* and 15*b* respectively. A certain tendency of the direction and magnitude of the lift force is not apparent in Fig. 15*a*. The same can be said for the lift force and impulse. Lift force acts both upwards and downwards during the extreme events with high $<F_D>$ as well as high impulse values. However, the lift forces of highest magnitude (for instance those shown by a circle in Fig. 15*b*) do not occur during extreme impulse events.

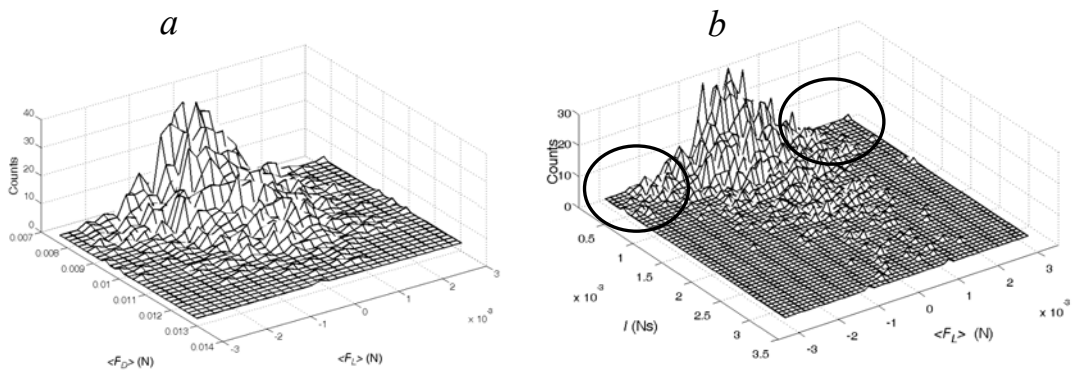

Figure 15. 3D mesh plot of the joint histogram of (a) drag force versus lift force and (b) impulse versus lift force (data from run U2-2522 data points were used, number of bins: 30x30 on $<D>$ -$<L>$ plane and 50x50 on I - $<L>$ plane).

Influence of Near-bed Bursting Phenomenon on the Forces of Impulse Events

Coherent structures in open-channel flow over rough beds have been studied extensively in sediment transport research. Recently, experimental studies of Hofland et al. (2005), and Dwivedi et al. (2010) using the quadrant analysis estimated the contributions from the four quadrants to the pressures acting on bed material and pointed out the importance of flow events in the fourth quadrant to particle entrainment when the force magnitudes are concerned. However, the influence of bursting phenomenon on impulse magnitude has never been investigated in sediment research before. Here we first consider the distribution of impulse magnitude on $<u>'$- $<w>'$plane, where the Reynolds decomposition is used for the velocity of impulse events, $<u>_i' = <u>_i - u_{mean}$ and $<w>_i' = <w>_i - w_{mean}$ (see Fig.3 for the description of $<w>_i$ magnitude). Accordingly, the boundaries of the quadrants can be given as:

$<u>_i' > 0$ and $<w>_i' > 0$ (I)

$<u>_i' < 0$ and $<w>_i' > 0$ (II)

$<u>_i' < 0$ and $<w>_i' < 0$ (III)

$<u>_i' > 0$ and $<w>_i' < 0$ (IV)

These events characterize the four types of near bed flow events, durations of which are equal to the matching impulse event durations (on the order of fractions of a second). The $<u>_i'$- $<w>_i'$ pairs and corresponding I_i values were identified. An interpolated contour plot of the impulse magnitude on $<u>'$- $<w>'$ plane was then created and is shown in Fig. 16*a* for run U3.

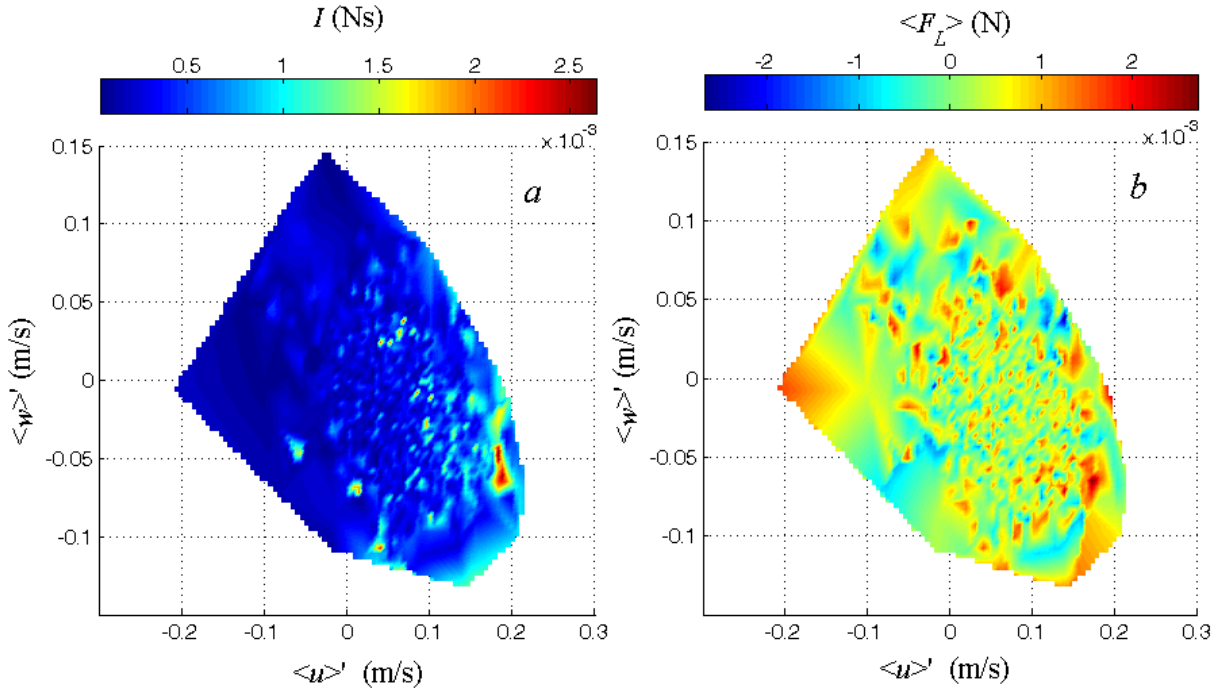

Figure 16. 3D surface plots of (*a*) impulse on $<u>'$ - $<w>'$ plane. Color bar on top indicates the impulse magnitude. (*b*) lift force associated with impulse events on $<u>'$ - $<w>'$ plane. Color bar indicates the lift force magnitude/direction. Run U3.

The extreme impulse events take place in the second and fourth quadrants the latter being more common. Lift force yet again does not show sensitivity to the type of quadrants and

is randomly distributed on <*u*>′- <*w*>′ plane as shown in Fig. 16*b*. The influence of lift force on particle dislodgement will be discussed in detail in the next section.

The fractions of the number of impulse events observed in each quadrant are given in Fig. 17 for all nine uniform flow conditions. The majority of the impulsive events take place in the fourth and the first quadrants in all runs. As the flow strength decreases, the number of events occurring in the first quadrant increases. For the given *Re** range, this increase is from 67% to %80 and is compensated by drops in the number of impulse events in both second and third quadrants from 10% to 0 and from 8% to 0 respectively. The number of impulse events observed in the first quadrant remains nearly constant around 21% of the total number of impulse events for all runs.

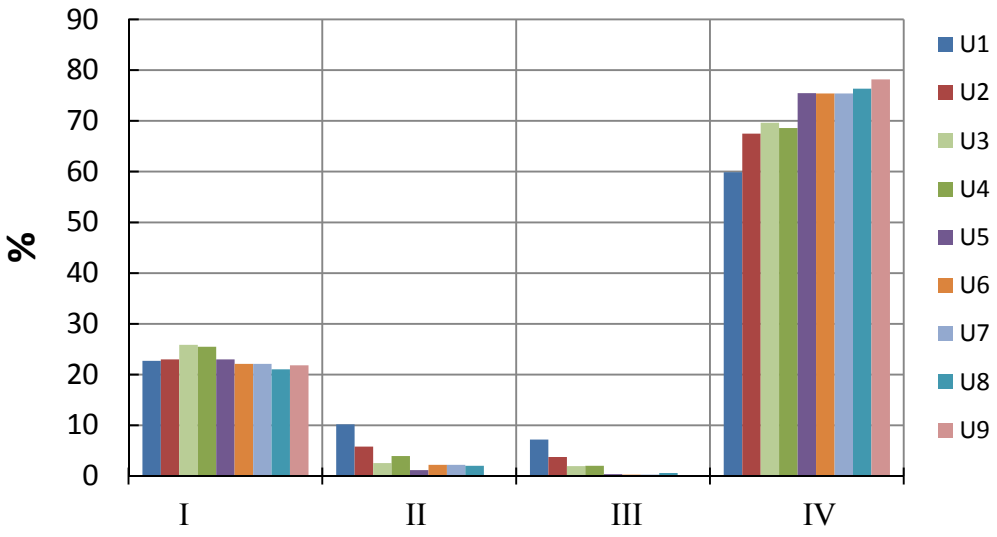

Figure 17. Bar plots of % total number of impulse events for each quadrant for all nine runs.

4.3 Implications for Particle Entrainment

The number of Detected Impulse Events

The total number of flow induced impulse events per unit time (with $F_D \geq F_{Dcr}$), n, as far as the sediment movement is concerned, is an essential flow parameter. n obtained directly from the measured F_D time series using Eqs. 1 and 2 for each run are given in Fig. 18 as a function of Re^*. For comparison, Fig. 18 also includes n values obtained from the drag force time series approximated using the near bed flow velocity:

$$F_D(t) = \frac{1}{2} C_D \rho A [u(t)]^2 \quad (5)$$

where:

i) the actual time average C_D value for each run shown in Fig. 9 was obtained from pressure experiment results and the effect of time-averaged lift force in Eq.1 was included,

ii) a constant C_D value of 0.9 (Schmeeckle et al. 2007) for all the runs was used and the effect of time-averaged lift force in Eq.1 was included,

iii) a constant C_D of 0.9 for all the runs was used, neglecting the effect of time-averaged lift force in Eq.1.

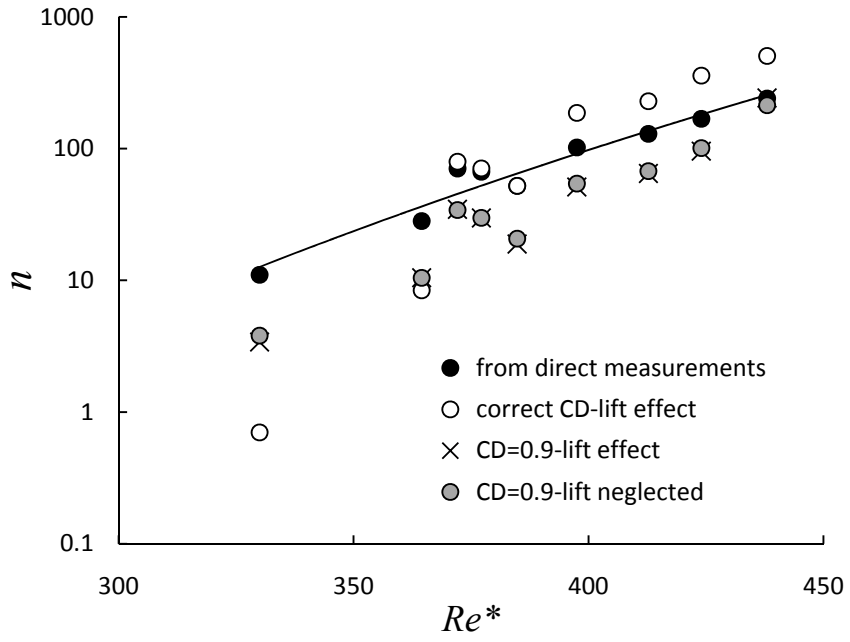

Figure 18. Plot of the total number of impulse events per min obtained using different methods, vs. Re^*. Linear line describes the overall variation of n calculated from directly measured F_D data with Re^* ($R^2 = 0.94$).

This comparison shows that the time-average lift force has minimal or no effect on n values. Overall, the variability in the n values shown in Fig.18 appears to originate from using a constant (whether the actual C_D or not) drag coefficient in Eq. 5 for estimating the drag force. The influence of using a constant C_D value of 0.9 results in a more than an order of magnitude difference in the calculated and true n values especially at low Re^*. At high Re^* range tested here, the n values are overestimated by up to a factor of two with even the use of the actual average C_D value, while they are underestimated if a C_D value of 0.9 is used.

The Effect of Lift Force during Impulse Events on the Critical Impulse

The rare impulse events (above a critical value), described by relatively long durations and a range of $<F_D>$ are expected to dislodge the grain from its pocket when they exceed a critical impulse level, I_{cr}. When the influence of lift force is negligible, then there is a constant critical impulse value in the streamwise direction for a given bed configuration (Diplas et al., 2008). Consider a detectible level of displacement of a spherical particle (Δx, Δz in the streamwise and vertical directions respectively) due to rolling. The change in the linear momentum of the particle in the streamwise direction when it is elevated by an amount of Δz can be used to approximate the critical impulse, which is required to cause this movement. That is:

$$I_{cr} = mV_{init} \tag{6}$$

where, m is the mass of the grain (back calculated from the submerged, effective weight), V_{init} is the theoretical initial velocity of the particle in the streamwise direction, which is estimated from the potential energy that the particle gains when it is elevated by an amount of Δz normal to the flow direction due to an impulse event (i.e. $V_{init} = \sqrt{2g\Delta z}$). For simplicity the energy losses due to friction are ignored here. Following such an approach, a constant I_{cr} value based on the W_s and Δz can be obtained.

As shown in chapter 4, lift force fluctuations are not always negligible and the instantaneous coupling of impulse and the magnitude and the direction of $<F_L>$ needs to be understood in order to substantiate the effect of lift force on the particle mobility. It is possible to incorporate $<F_L>_i$ values in the calculations to obtain an effective particle weight and consequently, a varying critical impulse value, I_{cri} which is a function of W_s, Δz, and $<F_L>_i$ for each impulse event.

In order to demonstrate the coupling of impulse events and the lift force as well as the influence of lift on the critical impulse values, a 2D (joint) histogram of impulse vs. lift force was created and is given in Fig. 19 (Data from run U2). As shown in the figure, lift force doesn't show a pattern and momentarily acts downward or upward within a range of magnitudes of ±21% of W_s. In addition to the joint histogram, Fig. 19 also shows the critical impulse values on I - $\langle F_L \rangle$ plane, necessary to cause initial particle movement calculated with both neglecting and taking into consideration the $\langle F_L \rangle_i$ values. Events above the critical impulse level (those to the right of the critical impulse lines shown in Fig. 19) are the events that can move a mobile Teflon particle.

Data from run U2 shows that the number of events above the actual (varying) critical impulse is 259. However, if a constant critical impulse is used then the number of events above this constant critical level is found to be 280. 12% of the events above the constant critical impulse are in fact below the actual critical impulse therefore not strong enough to dislodge the Teflon grain from its pocket (false positives). False negatives, which are below the constant critical impulse value but still above the actual (varying) critical impulse and capable of dislodging the grains, are nearly 2%. Taking into consideration the false positives and false negatives, neglecting the influence of lift force causes a 10% overestimation in the number of events that are in fact capable of causing particle entrainment. This fraction of total number of events representing the ambiguity in other runs can reach up to 15%. Therefore it is concluded that the fluctuations in lift force even for a fully exposed particle configuration can play a considerable role in particle dislodgement.

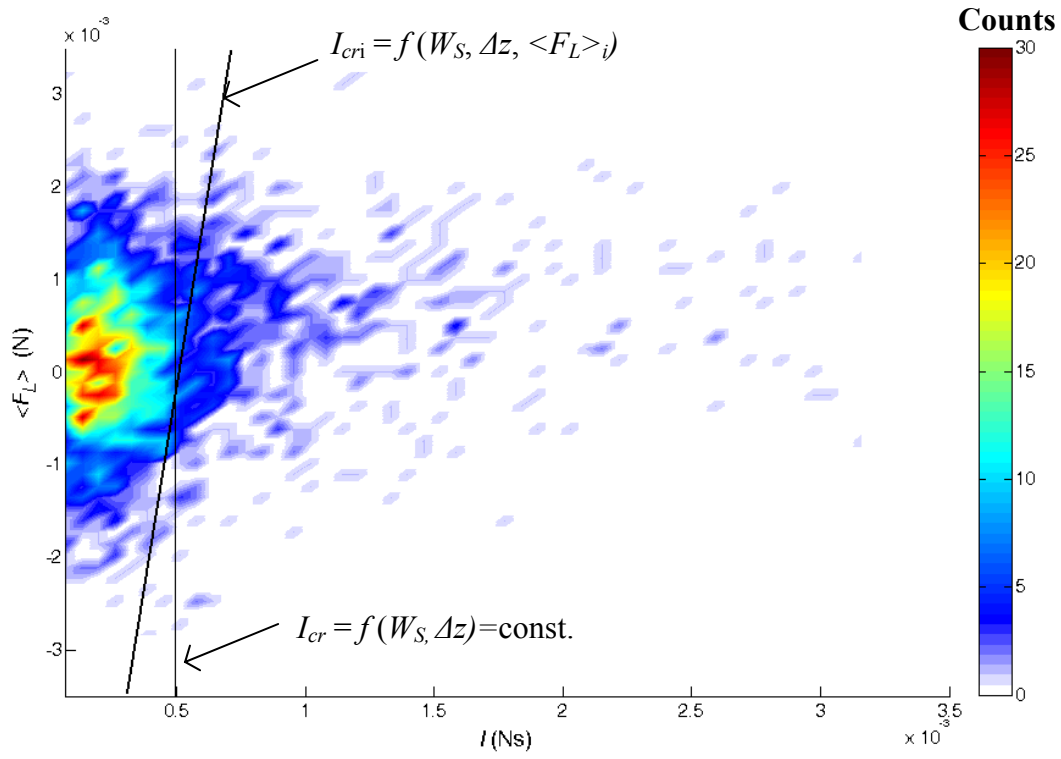

Figure 19. Surface plot of the 2D histogram of impulse versus lift force (from run U2-2522 impulse events were used, number of bins: 50x50 on I-<F_L> plane). Color bar indicates the counts. This figure is the same as Fig 15b.

The effect of Turbulence Intensity on the Number of Impulse Events and Particle Entrainment

Sumer et al. (2003) conducted flume experiments with a sand bed in the wake of a cylinder and concluded that the sediment transport increased appreciably with increasing turbulence intensity. Nelson et al. (1995) made similar observations in the wake of a backward facing step. Celik et al. (2010) showed a significant increase in both number of impulse events and the number of events above a given critical impulse value with minute changes in either flow parameters or grain density under uniform flow conditions

and concluded that this was not a coincidence but a phenomenon inherent to turbulent flow-particle interactions. The impulse concept was used to explain these interactions.

As shown in Table 1, a 50% increase in the turbulence intensity near the grain due to the cylinder resulted in a six-fold increase in the particle entrainment frequency. Overall, the available data from the present cylinder tests show that the particle entrainment frequency, n_e increases with about 4th power of the turbulence intensity (Fig. 20). The average lift force increases in cylinder wake flow, and reduces effective particle weight by up to 30% of the submerged weight (see chapter 4). It was shown in chapter 3 that an artificial decrease in the particle density by 25% causes nearly an order of magnitude increase in the number of impulse events capable of entraining the particle. Despite the variability in flow and bed material parameters this behavior shows strong qualitative similarities with the findings of Sumer et al. (2003) as shown in Fig. 21. Here, the bed load, q, and the particle entrainment frequency are compared, in which both parameters are non-dimensionalized by their counterparts from undisturbed flow conditions. Note that, Sumer et al. (2003) kept the bed shear stress constant while generating external turbulence by use of a cylinder to isolate the effect of turbulence level in their flume tests. In our experiments, the flow was not adjusted in the cylinder wake tests in order to keep the bed shear stress same as in the undisturbed flow experiments. The observed similarity here in the trends (see the exponents shown in the inset of Fig. 20) nevertheless helps explain the well known, yet poorly understood, phenomenon observed by Sumer et al (2003).

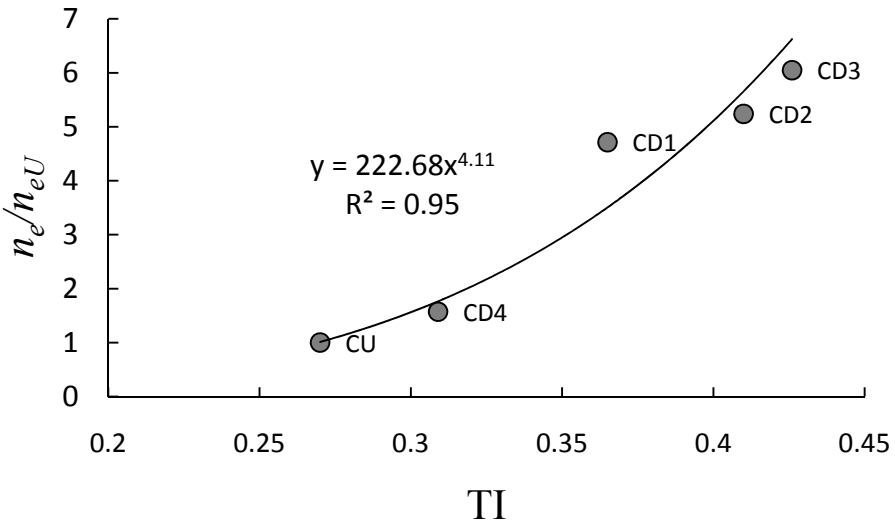

Figure 20. Ratios of particle entrainment frequency data obtained in cylinder tests to that of undisturbed flow conditions vs. turbulence intensity. Marker labels indicate the runs.

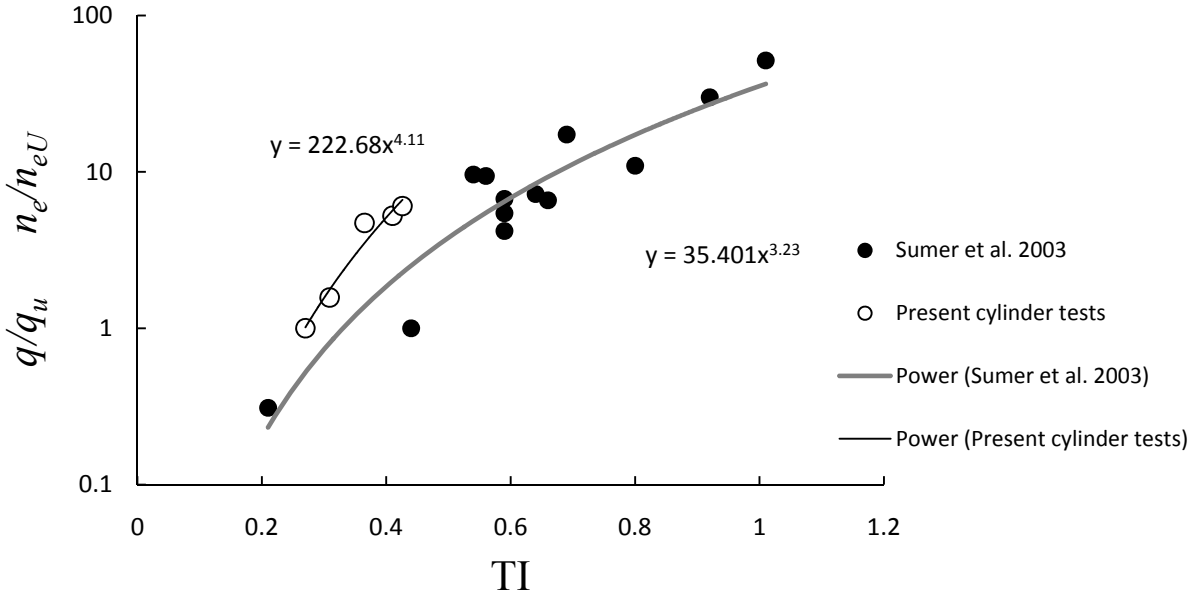

Figure 21. Ratios of bed material movement (bed load, *q,* data from Sumer et al. 2003, particle entrainment frequency, n_e, data from present tests, also shown in Fig. 20) obtained in cylinder test to that of undisturbed flow conditions vs. turbulence intensity.

5. Conclusions

We investigated the previously proposed impulse concept using directly measured surface pressures acting on a spherical grain. Lognormal distribution was validated to be the suitable pdf for impulse under both uniform and unsteady cylinder wake flows. Near bed flow velocity components and forces during impulse events were identified. For the given Re^* range it was shown that the impulse based ensemble average drag coefficient was higher than conventionally accepted drag coefficients for spherical particles. Drag coefficients obtained for impulse events varied substantially and inversely for given impulse based streamwise velocities. Lift force of impulse events was found to be not correlated with drag force or impulse. Extreme lift force magnitudes were observed to occur when low $<C_D>$ values were observed but not during extreme impulse events. Overall, without an obvious trend, lift forces of impulse events were found to be, though rarely, consequential for particle entrainment for the given bed configuration. It was then shown that the majority of the high magnitude impulse events were observed in the fourth quadrant. A comparison was used to present the effect of force approximations on the particle movement analysis and it was found that using a constant drag coefficient influenced the detection of impulse events significantly. Lift force of the impulse events was shown to change the critical impulse level required to dislodge the grain instantaneously. Finally, the influence of turbulence intensity on the particle movement was investigated and found to be significant due to increased average lift force under such conditions (chapter 4), in agreement with well known observations of others available in the literature.

Acknowledgements

The support of the National Science Foundation (EAR-0439663 and EAR-0738759) and Army Research Office for this study is gratefully acknowledged.

References

Balakrishnan, M. (1997). “The role of turbulence on the entrainment of a single sphere and the effects of roughness on fluid-solid interaction” PhD dissertation, Virginia Polytechnic Institute and State University, Blacksburg, VA.

Celik, A. O., Diplas, P., Dancey, C.L., Valyrakis, M. (2010) "Impulse and particle dislodgement under turbulent flow conditions" Physics of Fluids, DOI:10.1063/1.3385433, 22, 046601:1-13

Celik, A. O., Diplas, P., Dancey, C.L., (Instantaneous pressure measurements on a spherical grain under threshold flow conditions- manuscript in preparation)

Cheng, N. S., Law, A. W. K., and Lim, S. Y. (2003). “Probability distribution of bed particle instability.” Advances in Water Resources. 26(4), 427-433.

Detert, M. Weitbrecht, V. and Jirka, G.H.,(2010). “Laboratory Measurements on Turbulent Pressure Fluctuations in and above Gravel Beds” J. Hydr. Engrg.,ASCE, 136(10), 779–789

Diplas P., Dancey C.L., Celik A.O., Valyrakis M., Greer K., and Akar T. (2008). “The role of impulse on the initiation of particle movement under turbulent flow conditions” Science, 322, 717-720

Diplas, P., Celik, A. O., Dancey, C.L. and M. Valyrakis. (2010). ”Non-intrusive method for detecting particle movement characteristics near threshold flow conditions” Journal of Irrigation and Drainage Engineering, ASCE, Volume 136, Issue 11, pp. 774-780

Dwivedi, A., Melville, B., and Shamseldin, A. Y., (2010). “ Hydrodynamic Forces Generated on a Spherical Sediment Particle during Entrainment” J. Hydr. Engrg.,ASCE, 136(10), 756–769

Einstein, H.A., and El-Samni, E.A. (1949). “Hydrodynamic forces on a rough wall” Rev. Mod.
Phys., 21(3), 520-524.

Fenton, J.D., and Abbot, J.E. (1977) “Initial movement of grains on a stream bed : The effect of relative protrusion” Royal Society (London) Proceedings, v. 352A, p. 523-537.

Gessler, J. (1971). “Beginning and ceasing of sediment motion” in River Mechanics, Shen, H.W., Ed., Water Resources Publications, Forth Collins, CO, Chap.7

Hofland, B., Booij, R., Battjes, J. (2005). “Measurement of fluctuating pressures on coarse bed material.” J. Hydr. Engrg.,ASCE, 131(9), 770–781

Nelson, J. M., Shreve, R. L., MacLean, S. R. and Drake, T. G. (1995). "Role of near-bed turbulence structure in bed load transport and bed form mechanics" Water Resour. Res. 31(8), 2071–2086.

Nezu, I., Nakagawa, H. (1993) "Turbulence in open channel flows." IAHR Monograph, Balkema, Rotterdam

Mouri, H., Hori, A. and Takaoka, M. (2009)."Large-scale lognormal fluctuations in turbulence velocity fields" Physics of Fluids, 21, 065107

Papanicolaou, A.N., Diplas, P., Evaggelopoulos, and N., Fotopoulos, S. (2002). "Stochastic incipient motion criterion for spheres under various bed packing conditions" J. Hydr. Engrg., 128(4), 369-380

Schmeeckle, M.W., Nelson, J. M., and Shreve, R. L. (2007). "Forces on stationary particles in near-bed turbulent flows" J. Geophys. Res., 112, F02003

Smart G. M., and Habersack H. M. 2007. Pressure Fluctuations and Gravel Entrainment in Rivers, Journal of Hydraulic Research, IAHR, Vol.45, No.5, 661-673

Sumer, B.M., Chua, L.H.C., Cheng, N.S., and Fredsoe, J. (2003). "Influence of turbulence on bed load sediment transport" J. Hydr. Engrg., 129(8), 585-596

Sumer B. M., Fredsoe E J., (2006). "Hydrodynamics Around Cylindrical Structures", World Scientific, Singapore.

Sutherland, A. J. (1967). "Proposed mechanism for sediment entrainment by turbulent flows" J. Geophys. Res., 72(24), 6183-6194.

White, C. R. (1940). "The equilibrium of grains on the bed of a stream." Proc. R. Soc. London, Ser. A, 174, 322-338.

Wu, F.C., and Chou, Y.J. (2003). "Rolling and lifting probabilities for sediment entrainment" J. Hydr. Engrg., 129(2), 110-119

Zanke U. C. E. (2003). "On the influence of turbulence on the initiation of sediment motion." Int. J. Sed. Res.,18(1), 17-31

Chapter 6. Conclusions

This work showed, for a range of flow conditions and particle entrainment rates, that the impulse is a better suited parameter for describing the role of turbulence fluctuations on the particle movement for the given bed configuration under incipient conditions.

The non-intrusive particle tracking method used here proved to be reliable in detecting even the slightest movements of a test grain. Using the data obtained with this system, a connection was found between the particle entrainment probability and the probability of occurrence of impulse events above critical level. The observed sensitivity of particle entrainment rate to minute changes in the flow parameters was explained with the associated significant increase in the frequency of impulses capable of dislodging the grain.

Peak force and corresponding flow patterns important for the particle entrainment were obtained from the conditional sampling of the pressure data. Force patterns showed consistent positive lift force peaks occurring before and after the peak events in the drag force. These patterns were generally occurring during sweep type near bed flow events and providing favorable conditions for particle entrainment. The mechanism responsible for these force patterns was discussed.

It was shown that the dominance of sweep events in particle dislodgement can be due to the frequent occurrence of high magnitude impulse events during sweeps. Impulse measured directly or obtained indirectly was well characterized by the proposed log-normal distribution.

A direct connection between the lift forces and flow structures yet was not evident but lift forces occurring during impulse events were shown to change the critical impulse

level required to dislodge the grain instantaneously. In cylinder wake flows, the turbulence intensity was higher compared to the undisturbed flow condition but the average lift force increased as well, reducing the effective weight of the particle considerably. Such effects were shown to be enhancing the particle mobility significantly in this study and by other researchers in sediment transport field. Instantaneous lift force was also shown to be reaching very high levels that can be consequential to particle mobility even though it was alone not capable of dislodging the mobile grain.

In this work, the flow structures associated with impulses or individual pressure peaks were not precisely identified from the single point velocity measurements. The impulse concept can be expanded by using state of the art measurement techniques, such as particle image velocimetry, together with synchronized pressure or force measurements. Such measurements might particularly shed light on the actual flow structures that are responsible for certain local force and velocity patterns.

On the other hand, it appears that the applicability of the impulse concept might be limited to the low shear stress conditions. That is, there must be a limiting flow strength above which, the high force magnitudes lasting over longer periods of time rather than impulse with finite durations can still describe the particle mobility. This critical level that distinguishes the impulse and force magnitude dominated regimes of particle movement has to be determined and parameterized. Another important parameter that involved in the impulse analysis in this work is the critical impulse. This was a single, well defined value in the present work due to the spherical particle configuration used. However the critical impulse is probabilistic due to the random nature of the orientation of particles on a natural bed. It is therefore anticipated that the implementation

of the impulse framework for more complex bed configurations will need characterization of the variation in critical impulse levels on a given bed surface.

Recently developed discrete particle models can incorporate impulse concept with such enhanced understanding of the influence of flow structures, limits of applicability and an understanding of the variations in the critical impulse level, for more accurate bed material movement simulations. Models with better predictive abilities might have direct influence on practical applications.